MODELING WAVE-CURRENT INTERACTION
IN THE VICINITY OF
HUMBOLDT BAY, CALIFORNIA

by

Nathan J. Claasen

A Thesis

Presented to
The Faculty of Humboldt State University

In Partial Fufillment

of the Requirements for the Degree

Master of Science

In Environmental Systems: Mathematical Modeling

December, 2003

Report Documentation Page	*Form Approved* *OMB No. 0704-0188*

1. REPORT DATE **DEC 2003**	2. REPORT TYPE **N/A**	3. DATES COVERED **-**

4. TITLE AND SUBTITLE **Modeling Wave-Current Interaction in the Vicinity of Humboldt Bay, California**	5a. CONTRACT NUMBER 5b. GRANT NUMBER 5c. PROGRAM ELEMENT NUMBER
6. AUTHOR(S) **Claasen, Nathan J.**	5d. PROJECT NUMBER 5e. TASK NUMBER 5f. WORK UNIT NUMBER
7. PERFORMING ORGANIZATION NAME(S) AND ADDRESS(ES) **Humboldt State University, Humboldt, CA**	8. PERFORMING ORGANIZATION REPORT NUMBER
9. SPONSORING/MONITORING AGENCY NAME(S) AND ADDRESS(ES)	10. SPONSOR/MONITOR'S ACRONYM(S) 11. SPONSOR/MONITOR'S REPORT NUMBER(S)

12. DISTRIBUTION/AVAILABILITY STATEMENT
Approved for public release, distribution unlimited

13. SUPPLEMENTARY NOTES

14. ABSTRACT

The interactions between waves and currents can be complex, primarily because of the nonlinear relationships between the two. Nevertheless, in computational models it is often desirable to simplify, or even ignore, the coupling between waves and currents because of the computational expense. In order to assess the errors associated with different forms of wave-current coupling in a realistic coastal inlet environment, the STWAVE wave model and ADCIRC current model been applied to Humboldt Bay, California, the only deep-draft harbor in a 400-mile stretch along the Pacific coast of the continental United States. These models will also ultimately be used to help understand the details of sediment transport and the implications of alternative dredging schemes at Humboldt Bay. The models are initially validated and then examined under a variety of climatological wave and tidal forcing conditions using uncoupled, one-way coupled, and two-way coupled forms of the wave and current models. Current fields, radiation stress, wave height, wave period, and wave turning are compared in the coupled and uncoupled applications to determine the importance of modeling wave-current interaction accurately at Humboldt Bay. A general set of guidelines for coupled model application are presented based on the results from this study.

15. SUBJECT TERMS

16. SECURITY CLASSIFICATION OF:			17. LIMITATION OF ABSTRACT	18. NUMBER OF PAGES	19a. NAME OF RESPONSIBLE PERSON
a. REPORT	b. ABSTRACT	c. THIS PAGE	**UU**	**192**	
unclassified	**unclassified**	**unclassified**			

Standard Form 298 (Rev. 8-98)
Prescribed by ANSI Std Z39-18

MODELING WAVE-CURRENT INTERACTION IN THE VICINITY OF HUMBOLDT BAY, CALIFORNIA

by

Nathan J. Claasen

Approved by the Master's Thesis Committee:

Dr. Greg Crawford, Major Professor Date

Dr. Adele Militello, Committee Member Date

Dr. Ken Owens, Committee Member Date

Dr. Rollie Lamberson, Graduate Coordinator Date

Dr. Donna E. Schafer, Dean for Research and Graduate Studies Date

ABSTRACT

MODELING WAVE-CURRENT INTERACTION IN THE VICINITY OF HUMBOLDT BAY, CALIFORNIA

By

Nathan J. Claasen

Master of Science In Environmental Systems: Mathematical Modeling

Humboldt Bay, California is the only deep draft harbor in a 400 mile stretch along the Pacific coast of the continental United States. Large, high energy waves and a sizeable tidal prism characterize the local marine environment. The navigational channels and entrance region of the bay are dredged once or twice a year, at significant cost.

The interactions between waves and currents can be complex, primarily because of the nonlinear relationships between the two. Nevertheless, in computational models it is often desirable to simplify, or even ignore, the coupling between waves and currents because of the computational expense. In order to assess the errors associated with different forms of wave-current coupling in a realistic coastal inlet environment, wave and current models been applied to the Humboldt Bay, California region. These models will also ultimately be used to help understand the details of sediment transport and the implications of alternative dredging schemes at Humboldt Bay.

The wave model, STWAVE, is a steady state spectral wave model developed by the Army Corps of Engineers (ACE). It is a two dimensional finite difference model based on linearized wave theory and is designed to be applied over a limited area near shore. The current model, ADCIRC, was developed by Dr. Luettich of the University of North Carolina and Dr. Westerink of the University of Notre Dame. ADCIRC is a finite element model. STWAVE and ADCIRC are coupled through the Surface-Water Modeling System (SMS), developed by the Environmental Modeling Research Laboratory (EMRL) at Brigham Young University. The models are initially validated against observations from a permanent tide gauge station in the bay and from moorings installed during an ACE field study near the bay entrance in the spring of 2002.

The models are then examined under a variety of climatological wave and tidal forcing conditions using uncoupled, one-way coupled, and two-way coupled forms of the wave and current models. Current fields, radiation stress, wave height, wave period, and wave turning are compared in the coupled and uncoupled applications to determine the importance of modeling wave-current interaction accurately at Humboldt Bay. Two-way coupled runs were defined as the standard (most accurate); uncoupled and one-way coupled runs were then compared against the two-way coupled runs.

A general set of guidelines for coupled model application are presented based on the results from this study. For modest waves and tidal currents (significant wave height, H_s, < 1.8 m; dominant period, T_p, < 9 s; tidal currents, U < 1.0 m/s) and a dominant wave direction roughly aligned with the jetties, the one-way coupled runs reproduced the two-way coupled runs satisfactorily. For large waves (H_s > 2.4 m, T_p > 11 s), large tidal flows (U > 1.5 m/s), or more oblique wave directions (greater than about 20° from the jetty orientation), two-way coupling is required to produce satisfactory results.

ACKNOWLEDGEMENT

Although it is my own name that appears on the front of this document, there are many others who have given both time and resources to produce this work.

The research herein documented was funded and directed by the Coastal Inlets Research Program, a unit of the United States Army Corps of Engineers. Innumerable thanks are due to the Corps in general as well as specifically to Dr. Nicholas Kraus, Dr. Adele Militello, Dr. Mary Cialone, Dr. Jane McKee Smith and Mr. Mitch Brown. Without their dedication and expertise, this project would have been impossible.

Thanks are also due to the Mathematics Department of Humboldt State University. I am greatly in debt to Dr. Rollie Lamberson, Dr. Ken Owens, and Dr. Dale Oliver for encouragement and support in pursuit of this degree.

A very heartfelt thanks goes also to Dr. Greg Crawford, a mentor and a friend. Thanks for the countless hours that you have spent with me over the course of the last three years. Thanks for giving of yourself to me. I truly am honored to have had the opportunity to have worked with you.

Thanks too to Mom and Dad, for all the encouragement and patience. I am now officially free to help with the retaining wall.

Thanks to you also, Elizabeth, for putting up with the late nights and distractions that you have worked through with me. I am truly blessed to have you as my wife.

Table of Contents

TABLE OF CONTENTS (CONTINUED)

LIST OF TABLES

LIST OF TABLES (CONTINUED)

LIST OF FIGURES

LIST OF FIGURES (CONTINUED)

LIST OF FIGURES (CONTINUED)

LIST OF FIGURES (CONTINUED)

LIST OF FIGURES (CONTINUED)

LIST OF FIGURES (CONTINUED)

LIST OF FIGURES (CONTINUED)

LIST OF FIGURES (CONTINUED)

LIST OF FIGURES (CONTINUED)

1. INTRODUCTION

Coastal inlets are short, narrow connecting channels between the open ocean and sheltered bays or lagoons. Ranging from a few hundred meters to several kilometers in width, they provide an important link between harbors and shipping lanes as well as access to shelter for regional fishing vessels. Local economies are improved with the ability to efficiently import and export commodities such as lumber, industrial goods, and petroleum products over water.

Coastal inlets are by nature dynamic, continually shaped and reshaped by strong hydrodynamic forces. It is the ever-changing nature of these inlets that raises concern for those who would navigate them. Powerful ocean waves and strong tidal currents cause erosion in some places, picking up sediment for deposition elsewhere. Shipping channels are filled in, decreasing the size of ship and load that can pass. Underwater sandbars are formed, increasing wave steepness and refocusing wave energy, which in turn increases risk to ships using the inlet. Expensive engineering projects, such as jetty construction or dredging, are often undertaken to maintain or increase both the safety and the accessibility of a given inlet. Understanding the physical processes involved allows for design and construction of stable navigation channels and increases the usefulness of the harbors to which they lead. Since tidal currents and wave stresses play such a large part in the dynamics of coastal inlets, much effort has been given to understanding these processes.

Waves and currents in coastal inlets interact with each other. In the presence of a current, waves can be refracted, steepened, or even blocked (Wright *et al.* 1999). If the current is strong enough, it may even cause wave breaking. Currents also may change the distance to which wave energy propagates into an inlet. Wave period is not changed in the presence of a current, although the wavelength may be (Wright *et al.* 1999). Initial work in quantifying the changes in wave properties in the presence of currents was done by Thompson (1949), who was able to calculate wavelength and wave phase speed when the depth, current velocity, and wave frequency were known. A detailed review of the subject is provided by Jonsson (1990).

Currents are also modified by the presence of waves. Waves generate mean horizontal stresses; gradients of these stresses generate net currents. The original derivation and quantification of these gradients was done by Longuet-Higgins and Stewart. In a series of papers (Longuet-Higgins and Stewart, 1960; 1961; 1962) they present an analytical derivation and perturbation analysis of the non-linear properties of waves, in the process coining the term radiation stress. In a subsequent paper, they present results from the previous papers in an expository form with application to observed wave phenomena such as wave set-up and current-induced wave steepening (Longuet-Higgins and Stewart, 1964).

In numerical studies of sedimentation at tidal inlets, the interaction of wave and tidal current interaction have been limited by computational complexity and model sophistication. In the last decade advances in computing power have allowed numerical simulation of complex wave-current interactions on the scale of coastal inlets (e.g., Zhang and Wu 1999; Li and Davies 1996). Many models for simulating full wave-current interactions are designed for high-performance computers. In practical engineering applications, however, uncoupled wave and current models have often been applied. For example, STWAVE is a wave model based on linear wave theory (Smith 2001). ADCIRC is a validated, two-dimensional depth-integrated (2DDI) circulation model (Luettich *et al.* 1992).

STWAVE and ADCIRC are often run independently, without coupling of waves and currents. There have, however, been some studies that have included partial coupling of these models, specifically the incorporation of wave-generated currents. One example of such studies is the U.S. Army Corps of Engineers' (USACE) modeling work at Grays Harbor, Washington State (M. Cialone, pers. comm. 2001). Such approaches may be effective under modest wave conditions and currents, but it remains to be seen how critical a complete solution is in the presence of high-energy wave conditions and large currents.

Recent software enhancements now allow STWAVE and ADCIRC to be coupled to each other in a variety of ways. The primary goal of this project is to address the significance of the choice of model coupling in an environment where waves and currents can strongly interact.

Humboldt Bay, California, the inlet that is the focus of this project, experiences high-energy waves and large tidal currents. Tidal currents are strong through the inlet, averaging 2.1 m/s for peak ebb near the entrance (Costa and Glatzel 2002). Wave climates are extreme, with significant wave heights on the order of 7 m observed annually. The high-energy environment of the Humboldt region provides for a study area in which the wave-current interactions are expected to be strong.

Model performance is evaluated through intercomparison of model results for different coupling options, as well as comparisons against available observations. Wave model solutions are evaluated by comparing wave height, period, direction, and breaking fields for coupled and uncoupled model runs. The current model is evaluated on the basis of current direction and magnitude. Specific questions are addressed such as: Should the wave model be given current velocity input? Are wave model-generated radiation stresses significant in current model calculations? Tradeoffs between model run-time vs. model accuracy are also examined. The product of this study, a better understanding of the significance of wave-current interaction in modeling, may be applied in future engineering studies dealing with sediment transport, channel reliability, and navigational safety at Humboldt Bay and elsewhere.

2. STUDY AREA: HUMBOLDT BAY, CALIFORNIA

This chapter presents the physical features and oceanography of Humboldt Bay and the surrounding region. Wave climate, weather patterns, and bathymetric features pertaining to modeling waves and currents are described in detail.

2.1. Location and Physical Oceanography

Humboldt Bay is a multi-basin coastal lagoon and is the only deep-draft harbor in a 400-mile stretch of the Pacific coast between San Francisco, California and Coos Bay Oregon. The section of coastline that contains the bay runs in a relatively straight northeast/southwest line from Cape Mendocino in the south to Trinidad Head in the north (Figure 2.1).

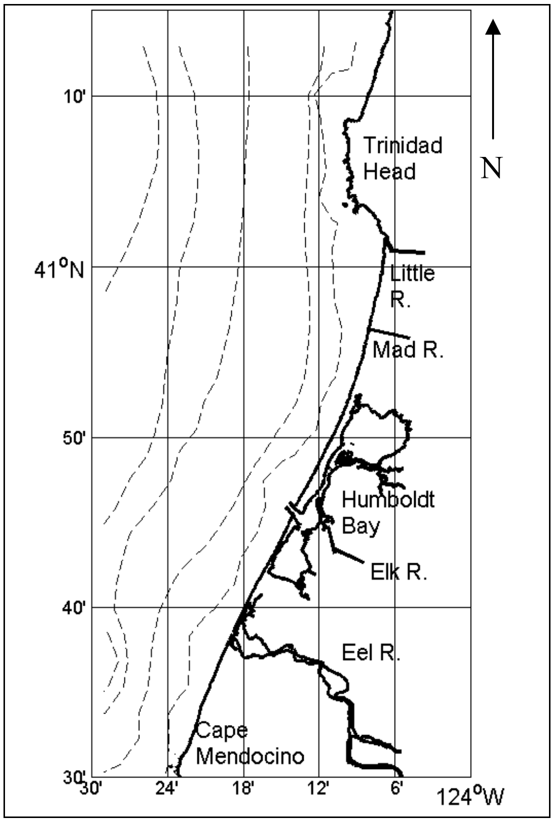

Figure 2.1. Northern California coastline. Dashed lines represent isobaths at 20, 50, 100, 200, and 500 m (derived from a subset of the GTOPO30 [Smith and Sandwell 1997] topographic data set).

According to Costa and Glatzel (2002), the watershed of the bay is 223 square miles with no major rivers in the area emptying directly into the bay. The annual freshwater input to the bay is estimated to be on the order of the tidal prism; 7.4 x 10^7 m^3 (Costa 1982). Humboldt Bay is made up of three sub-bays, the North Bay (or Arcata Bay), the Entrance Bay, and the South Bay. Both the North Bay and the South Bay consist of a series of deeper channels and large areas of intertidal flats. The long thalweg between the Arcata Bay and the entrance contributes additional complexity to tidal circulation near the interior of the entrance. At lower low tide the total area of the bay is

21 km^2 while at high tide, the bay spans an average of 67 km^2 (Costa and Glatzel 2002). Recently work has been done on the entrance channel, deepening it from 12 m to 15 m.

Climate for the region is moderate, and is marine-dominated due to the southward flowing California current system (Costa and Glatzel 2002). Ocean temperatures range between 12 and 18° C with little annual variation. Air temperatures range mostly between freezing and 23° C. Rainfall for the area is typically between 30 and 40 inches per annum, with no storms of hurricane magnitude (Costa and Glatzel 2002).

Winds are seasonal, with the strongest winds occurring in the winter. Peak winds are often associated with storm events and come out of the southwest or southeast. In the spring, typically beginning in March, winds are more constant and come out of the north to northwest. By mid summer, sea breeze is typical with winds increasing throughout the day and dying at night. The orientation of Humboldt Bay combines with the prevailing wind direction to produce significant wind generated waves in the bay (Costa and Glatzel 2002).

Circulation in Humboldt Bay is tidally dominated which makes for generally well-mixed marine water hydrography within the bay. Tides are mixed semi-diurnal, with a mean range of 1.51 m and a diurnal range of 2.11 m at the entrance. About 50 % of volume of the tidal prism flows to the North Bay and 30 % to the South Bay (Costa and Glatzel 2002). Peak currents at the Humboldt Bay entrance exceed 2.1 m/s regularly (Costa 1982) with average peak velocity on ebb tide of 1.0 m/s and 0.82 m/s on flood.

The wave climate at Humboldt Bay is extreme in comparison to most United States inlets. Waves from the northwest are the most common, with waves out of the southwest having the greatest energy (Costa 1982). Significant wave heights of up to 8 m can occur annually and wavelengths as long as 1000 m have been observed (Costa 1982). Average monthly values for wave heights and wind stresses can be seen in Table 2.1. The highest-energy waves acting in the inlet are thought to significantly influence currents in the bay itself (Costa 1982). The convex nature of the bar, the incident wave direction, and the alignment of the jetties tend to focus wave energy into the Entrance Bay, causing erosion and influencing sedimentation, mixing, flushing, and circulation within the Entrance Bay (Costa and Glatzel 2002).

Table 2.1. Mean wave properties measured at buoy NDBC (National Data Buoy Center) 46022 (40.74 °N 124.51 °W), based on observations from January, 1982 through May, 1997 [after Harris, 1999]. High discharge (i.e., flood) conditions are based on data from the Eel River gauge at Scotia, California.

Month	**WAVE CONDITIONS**	
	Mean Significant Wave Height (m)	**Mean Dominant Period (s)**
January	3.1	13.2
February	2.9	12.6
March	2.9	12.3
April	2.4	11.3
May	2.1	9.8
June	2.0	9.4
July	1.8	8.8
August	1.7	8.7
September	2.0	9.6
October	2.3	11.0
November	2.8	12.0
December	3.0	12.8
Overall	2.4	10.9
During High River Discharge:		
$Q > 1000\ m^3/s$	3.8	12.8
$Q > 2000\ m^3/s$	4.2	12.9

Sources of sediment to the entrance are the Eel River, 14 km to the south, and the Mad River, about 24 km to the north. The Eel River has been known to produce massive quantities of sediment during winter high currents. On one day in January of 1980, for example, 2.25 million tons of sediment was emptied from the Eel into the Pacific (Gates 1986). Due to the wind/wave climate during the winter months, sediment coming from the Eel during those months is thought to travel northward, providing material for the ebb shoal as well as depositing in the bay (Costa 1982).

2.2. History of Engineering Projects at Humboldt Bay

According to Costa (1982) studies for the improvement of the Humboldt Entrance began in 1871 with the first dredging and jetties completed in 1881. Because of large waves, the jetties were destroyed that first winter. Several other revisions of the jetties include the completion of brush and stone structures in 1900, repair and improvements between 1911 and 1917, and completion of new rubble-mound structures in 1939. The jetties continued to sustain damage from the high-energy conditions including the washing away of 100-ton blocks in 1964. By 1971, the heads of the jetties had been completely destroyed. At that time revolutionary new armor, in the form of concrete dolosse, was used to protect rebuilt jetties.

The dredging of channels within the bay and entrance has been an ongoing project. Initially dredged to a depth of 7.6 m in 1896, the bar channel has been progressively deepened and widened. In 1939 the channel was dredged to 9.1 m and in 1954 it was dredged to 12 m. In 1954 the Eureka and Samoa channels were also dredged to 9.1 m. In 1999 a new deepening project increased the depth of the entrance channel and the turning basin to 14.6 m. According to the USACE inlet database (http://cirp.wes.army.mil/cirp/inletsdb/inletsdb.php3?id='112' 2002), the present day jetties are 680 m apart at the narrowest point and over 1600 m in length. They are offset 500 m and angled approximately 17° north of cross-shore.

3. OCEAN WAVES: THEORY AND MODELS

This chapter presents the mathematical development of wave equations and other important concepts relating to the steady state spectral wave modeling. STWAVE, the model used in this research is also described.

3.1. Description of Waves: Basic Terminology and Linear Wave Theory

The surface of the ocean may have a widely-varied appearance depending on the current wave conditions. Sometimes nearly sinusoidal waves march in regular rows from a single distinct direction. At other times, the ocean surface may appear to consist of random motion. Because of this natural variation in wave conditions, it is often useful to represent the ocean state as a spectrum of different waves, with a range of properties and directions. This spectral approach simplifies mathematical analysis and is also an efficient way to conceptualize a given sea state. Mathematically, waves can be classified and differentiated according to energy using Fourier transforms.

The spectral representation depends on a few basic wave properties. When referring to theoretical (sinusoidal) water waves the wave height (H) is defined as the vertical distance between the wave peak and the wave trough.

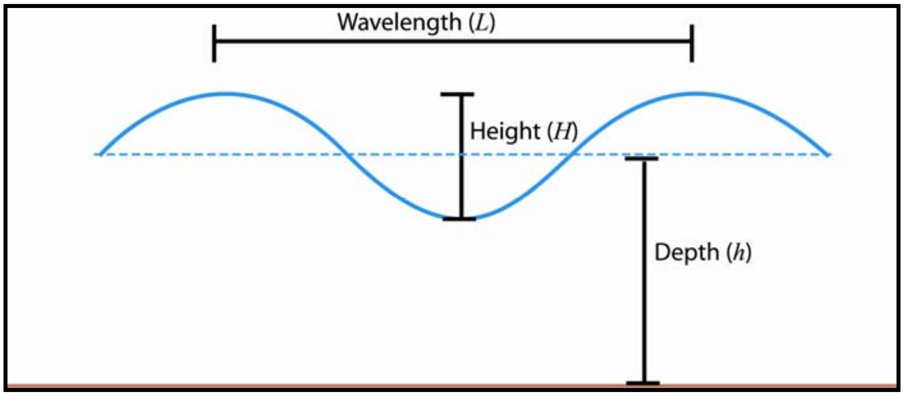

Figure 3.1. Simplified monochromatic sinusoidal wave depicting basic wave properties.

Table 3.1. Description and notation for basic wave properties. Refer to Figure 3.1.

Name	Notation	Description
amplitude	a	one half of the wave height (H)
wave number	k	$k = 2\pi / L$
period	T	the time for a full cycle of the wave to pass a fixed point
celerity	C	speed at which the individual wave propagates
group speed	C_g	the rate at which the wave energy is propagated
frequency	f	the number of wave peaks that pass a certain point in a second
angular frequency	ω	$\omega = 2\pi f$
significant wave height	$(H_{1/3})$	the average height of the highest one-third of all waves occurring in a particular time period

Wave models are a subset of a larger class of oceanic models. All oceanic models, both wave and circulation, solve some form of the Reynolds-averaged Navier-Stokes equations for mean quantities (Kantha and Clayson 2000), which are based on fundamental conservation equations. Dominant physical processes and properties in the realm of wave and current motions in water are surface forces, body forces, mass conservation, and momentum conservation.

In a real fluid, mass must be conserved. Thus when considering any small volume of fluid, there is a balance between the ratio of mass accumulation and the net fluxes of mass into that volume. The basic equation for the conservation of mass at a point in any fluid is:

$$\frac{\partial \rho}{\partial t}+\frac{\partial \rho u}{\partial x}+\frac{\partial \rho v}{\partial y}+\frac{\partial \rho w}{\partial z}=0 \qquad [3.1]$$

where ρ is the density of the fluid and *t* is time. The first term $\frac{\partial \rho}{\partial t}$, represents the rate of accumulation of mass at a fixed point; the three remaining terms represent the flux of mass in the *x*, *y*, and *z* directions respectively. The conservation equation can be rewritten, taking advantage of the total derivative of ρ as:

$$\frac{1}{\rho}\left(\frac{\partial \rho}{\partial t}+u\frac{\partial \rho}{\partial x}+v\frac{\partial \rho}{\partial y}+w\frac{\partial \rho}{\partial z}\right)+\frac{\partial u}{\partial x}+\frac{\partial v}{\partial y}+\frac{\partial w}{\partial z}=0 \qquad [3.2]$$

where the quantity in parenthesis represents the total derivative of ρ with respect to time $(d\rho / dt)$, given $u = dx/dt$, $v = dy/dt$, and $w = dz/dt$.

The quantity $(1/\rho)(d\rho/dt)$ is related to the change in pressure through a property called the bulk modulus that describes resistance to compression in the fluid. The bulk modulus of a fluid is defined as follows:

$$E \equiv \rho\frac{dp}{d\rho} \qquad [3.3]$$

where p is the pressure of the fluid. In essence the bulk modulus describes the incremental dependence of the density of a fluid on pressure. Further manipulation yields the following equality.

$$\frac{1}{\rho}\frac{\partial \rho}{\partial t} = \frac{1}{E}\frac{\partial p}{\partial t} \qquad [3.4]$$

For water, the bulk modulus is a large number, (2.07×10^9 Nm^{-2}). Practically this means that when pressure is increased by a factor of one million, density is increased by 0.05%. Thus water may be assumed to be incompressible, so that [3.2] can be approximated as

$$\frac{\partial u}{\partial x} + \frac{\partial v}{\partial y} + \frac{\partial w}{\partial z} = 0 \qquad [3.5]$$

Equation [3.4] is a simplified version of the conservation of mass equation, also known as the continuity equation. Often it is written $\nabla \bullet \vec{u} = 0$. The conservation of mass equation requires a fluid to be non-divergent.

Water is a Newtonian fluid, which is a fluid that deforms continuously under shear stress (opposing forces not acting through the center of mass of a given particle). The movement of any such fluid particle then is governed by Newton's second law, $\vec{F} = m\vec{a}$, for a volume of constant mass. Note that the acceleration is the total derivative of the velocity; $\vec{a} = d\vec{u}/dt$. Under the influence of several forces, the equation of motion can be written in the general form:

$$\sum \vec{F} = m\frac{d\vec{u}}{dt} \qquad [3.6]$$

Using a Taylor expansion to calculate the forces involved and dividing the resulting equation by the volume of the particle under consideration yields, for the components of the terms operating in the *x* direction:

$$\frac{du}{dt} = -\frac{1}{\rho}\frac{dp}{dx} + \frac{1}{\rho}\left(\frac{\partial \tau_{xx}}{\partial x} + \frac{\partial \tau_{yx}}{\partial y} + \frac{\partial \tau_{zx}}{\partial z}\right) + \mathrm{X} \qquad [3.7]$$

where X is the body force per unit mass acting in the x direction and the τ terms are internal shear stresses acting on the particle (Dean and Dalrymple 1991). Analogous equations can be written for the y and z directions.

Because of the low viscosity of water, a simplifying assumption is often made that the internal shear stresses are zero. This assumption confines the system to irrotational current, (i.e., no vorticity). Using this assumption and combining the conservation of mass and momentum equations yields the Euler equations.

$$\begin{aligned} \frac{du}{dt} &= -\frac{1}{\rho}\frac{\partial p}{\partial x} \\ \frac{dv}{dt} &= -\frac{1}{\rho}\frac{\partial p}{\partial y} \\ \frac{dv}{dt} &= -\frac{1}{\rho}\frac{\partial p}{\partial z} - g \end{aligned} \qquad [3.8]$$

where body forces in the x and y directions are zero and g represents the gravitational body force. Note that if turbulence is significant, the irrotational current assumption is rendered invalid and all of the terms must be kept as in [3.7] (Dean and Dalrymple 1991).

The Bernoulli equation relates the pressure field and the kinematics of the actual waves themselves and is useful in defining boundary conditions for actual solutions. It is derived by writing the Euler equations in integrated form, assuming two-dimensional irrotationality, and defining the velocity potential $\frac{\partial \phi}{\partial t}$ for the x and z directions. The actual form of the equation is:

$$-\frac{\partial \phi}{\partial t} + \frac{1}{2}\left(u^2 + w^2\right) + \frac{p}{\rho} + gz = C(t) \qquad [3.9]$$

In order to be solved, the Euler equations require boundary value information. In the case of linear wave modeling, there are two boundary conditions that apply. The first is known as the kinematic boundary condition, which states that there can be no current across an interface between the fluid and a surface. The surface itself, however, may or may not move. There are two possible kinds of surfaces, those which vary temporally and those which do not.

The bottom of the ocean is a boundary that is assumed not to vary with time. Since it is also impermeable, the bottom boundary condition can be defined:

$$\left.\vec{u}\bullet\vec{n}\right|_{z=bottom}=0$$

where $\vec{u}$ is the velocity vector and $\vec{n}$ is the unit normal vector to the surface. At the top of the water column is the free surface boundary, the part that moves up and down freely. The kinematic free surface boundary condition then combines the description of the physical surface of the wave as well as the current at that surface.

$$\left.\vec{u}\bullet\vec{n}\right|_{z=\eta}=\frac{\partial\eta/\partial t}{\sqrt{\left(\partial\eta/\partial x\right)^2+\left(\partial\eta/\partial y\right)^2+1}} \qquad [3.10]$$

where $\eta(x,y,t)$ describes the temporal vertical displacement of the free surface about the horizontal plane.

The other boundary condition is the dynamic free-surface boundary condition, which assumes that pressure on the free surface is uniform along the waveform. This is where the Bernoulli equation is helpful. Set p_η, the pressure at the free surface to be constant and apply the Bernoulli equation.

$$-\frac{\partial \phi}{\partial t}+\frac{1}{2}\left(u^2+w^2\right)+\frac{p_\eta}{\rho}+gz=C(t) \qquad [3.11]$$

Solution of these equations for a linearized water wave is then accomplished by separation of variables. Periodic functions are chosen with boundary conditions determining the associated parameters. To simplify the Bernoulli equation further, a small wave assumption is made. This means that a first order Taylor approximation, or linear term, is sufficient to describe the wave properties. For example, if $\eta << 1$, then $\eta^2 << \eta$ and thus can be ignored. After linearization and application of boundary conditions, the velocity potential is

$$\phi=\frac{Hg\cosh\left(h+z\right)}{2\omega\cosh kh}\cos kx\sin\omega t \qquad [3.12]$$

where g is the gravitational force and z is the water depth. A complete derivation of the linear form for velocity potential is available in many texts, for example Dean and Dalrymple (1991).

For waves traveling at angle α in the presence of an ambient current with magnitude U and traveling at angle δ, the velocity potential function and a kinematic free surface boundary condition can be combined to give the general dispersion relation:

$$\omega^2=\overline{U}k\cos(\delta-\alpha)+gk\tanh kh \qquad [3.13]$$

where $\overline{U} = \left(U_x, U_y\right)$ represents the velocity of the local current, δ is the direction of current current, and α is the direction of wave propagation. One can also show the celerity or rate of travel and group speed of the waves are given by:

$$\overline{C} = \frac{\omega}{k} + \overline{U}\cos\left(\delta - \alpha\right) \qquad [3.14]$$

$$\vec{C}_g = \frac{\overline{C}}{2}\left(1 + \frac{2kh}{\sinh 2kh}\right) + \overline{U} \qquad [3.15]$$

The direction of absolute celerity is called the wave orthogonal and is perpendicular to the wave crest. The wave ray describes the direction of energy propagation. Note that in the presence of ambient currents, the wave ray might differ from the wave orthogonal.

Waves can also generate a net current in the nearshore region. Longuet-Higgins and Stewart (1964) derived expressions for what they describe as “the excess flux of momentum due to the presence of waves” or radiation stress. Derivation of the radiation stress equations begins with the expressions for hydrostatic pressure ($p = -\rho g z$), total flux of horizontal momentum between the surface and the bottom ($\int_{-h}^{0} p_0 dz$), and wave velocity equations:

$$\begin{aligned} u &= \frac{a\sigma}{\sinh kh}\cosh k\left(z + h\right)\cos\left(kx - \sigma t\right) \\ w &= \frac{a\sigma}{\sinh kh}\sinh k\left(z + h\right)\sin\left(kx - \sigma t\right) \end{aligned} \qquad [3.16]$$

$$S_{xx} = \rho g \iint E\left(f, \alpha\right)\left[0.5\left(1 + \frac{2kh}{\sinh 2kh}\right)\left(\cos^2\alpha + 1\right) - 0.5\right] df d\alpha \qquad [3.17]$$

$$S_{xy} = \rho g \iint \frac{E(f,\alpha)}{2}\left[0.5\left(1+\frac{2kh}{\sinh 2kh}\right)\sin 2\alpha\right] df d\alpha \qquad [3.18]$$

$$S_{yy} = \rho g \iint E(f,\alpha)\left[0.5\left(1+\frac{2kh}{\sinh 2kh}\right)\left(\sin^2\alpha + 1\right) - 0.5\right] df d\alpha \qquad [3.19]$$

where $E(f,\alpha)$ is the expression for spectral wave energy as discussed below. S_{xx} is the flux of momentum in the direction of wave travel, S_{yy} is the flux of momentum perpendicular to the direction of wave travel, and S_{xy} represents the flux in the *x* direction of the *y* component of momentum.

Gradients of the radiation stresses can be applied to calculate wave driven currents in circulation models. STWAVE, the wave model used in this study, calculates quantities known as radiation stress tensors.

$$\tau_x = -\frac{\partial S_{xx}}{\partial x} - \frac{\partial S_{xy}}{\partial x} \qquad [3.20]$$

$$\tau_y = -\frac{\partial S_{yy}}{\partial y} - \frac{\partial S_{xy}}{\partial y} \qquad [3.21]$$

In most ocean current models, the radiation stress tensors are applied in the momentum equations as additional forcing terms. In the case of the models applied in this project, the radiation stress tensors are converted into spherical coordinates (as $\frac{\tau_{s\phi}}{\rho_0 h} - \frac{\tau_{b\phi}}{\rho_0 h}$ in equation [4.4]). This is done to limit error in calculation over a large mesh domain.

Direct application of these equations to ocean waves is complicated by the random variability of the ocean surface. Thus a more complete understanding of the mechanisms of wave generation is important for the modeling process. Ocean waves are generated by wind blowing over the surface of the water. A wave field is an area containing waves of varied size (wavelength and wave height) produced by variation in wind direction and speed. Each wave has an associated wave energy (*E*) and frequency (*f*). Although in nature the spectrum of frequencies in a wave field is continuous, for the purposes of observations and modeling, wave frequency and direction are classified discretely. For example at a wave gauge, observations are composed of many frequencies (σ_n) and amplitudes (a_n) with different phases (ε_n). Sea surface elevation then is expressed as a sum:

$$\eta(t) = \sum_{n=0}^{\infty} a_n \cos(\sigma_n t - \varepsilon_n) \qquad [3.22]$$

The total energy in the wave field can be found by integrating $a_n^{\,2}/\Delta\sigma$ when expressed as a function of σ.

The energy distribution associated with a wave field can be represented in a number of ways. A one dimensional spectrum (1-D spectrum) as in Figure 3.2 gives wave energy without direction, while a two dimensional spectrum (2-D spectrum) as in Figure 3.3 gives wave energy with its associated direction.

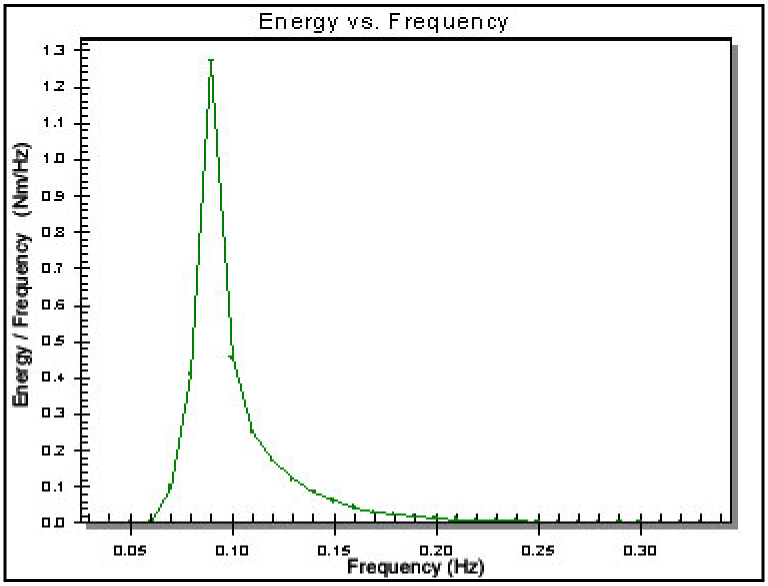

Figure 3.2 An example of a 1-D wave spectrum.

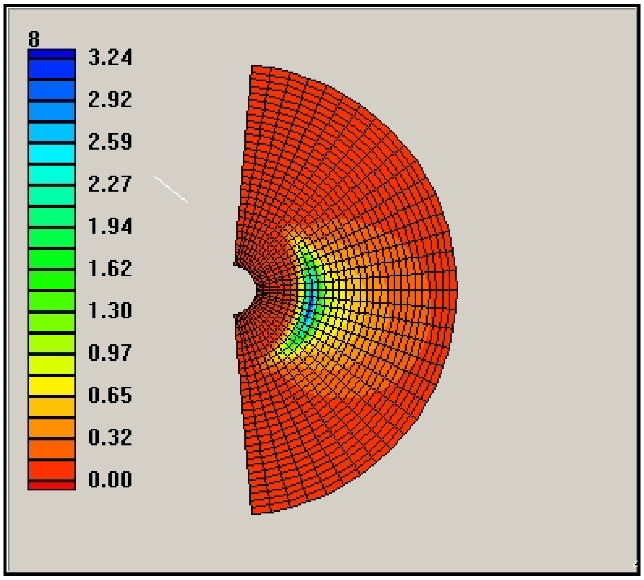

Figure 3.3 Plot of a 2-D spectrum used for STWAVE model input. Contours show energy magnitude for each frequency and direction. Frequency increases from the center outward.

3.2. Wave Model Development

Application of wave spectra as a descriptor of wave properties provided for an advance in wave modeling by allowing the use of the energy balance equation.

$$\frac{\partial E}{\partial t} + \vec{C}_g \bullet \vec{\nabla} E = \sum S_i \qquad [3.23]$$

In other words, the total energy E of the system can be determined according to the initial energy present and the source/sink terms S_i, which include atmospheric input, non-linear wave-wave interaction, and dissipation due to breaking. Source and sink terms were initially described by Miles (1957) and Phillips (1957) as occurring due to the influence of wind on the water and wave breaking respectively.

This approach was further refined by Hasselmann (1962, 1963a,b). He found that while the models had been using coupled linear systems for the explanation of energy input and dissipation, adding a non-linear wave-wave interaction term would allow for the energy exchange between frequencies. Data from the JOint North Sea WAve Project (JONSWAP; Hasselmann et al. 1973) and the research of Mitsuyasu (1968) highlighted the significance of the non-linear energy spreading terms.

Despite these advances, there still was some difficulty in describing energy input from wind-wave growth. Over reasonable fetch, which is the distance of wind-water interaction, wind-wave models often generated unnaturally large waves. One method of dealing with energy sources was to limit the spectral energy growth at a predetermined maximum value (Jensen 1994). Hasselman *et al.* (1973) proposed the following form for fetch limited wind waves

$$\phi(f) = \alpha g^{2}(2\pi)^{-4} f^{-5} e^{-\frac{5}{4}\left(\frac{f}{f_m}\right)^{-4}} \gamma^{e^{\frac{-\left(\frac{f}{f_{m-1}}\right)^{2}}{2\sigma^{2}}}} \qquad [3.24]$$

where α and f_m are fetch dependent scale parameters, and γ and σ are shape parameters. Hasselman *et al.* (1973) suggested values for these parameters to give the JONSWAP spectrum. Mitsuyasu (1968) modified and corrected the parameters γ and α based on dimensionless fetch dependence. Wave spectra are then defined in a model by the peak frequency f_p and a shape parameter defined by Phillips (1957).

A comparison of nine similar models based on these new spectral criteria yielded differences in wave energy by as much as a factor of four and motivated the formation of the SWAMP group (Sea Wave Modeling Project). The SWAMP group set out to remove the restrictions on spectral shape and wind input conditions that had been hampering the current crop of wave models (SWAMP 1985). This research led to the creation of verified ocean water models such as WAM, WAVEWATCH, and OWI-3G. These models are more true to the physical processes involved in wave generation and propagation than any of the prior models. The wave model implemented in this study, STWAVE, is a hybrid of these later techniques.

3.3. The STWAVE Model

STWAVE is a finite difference, nearshore wave transformation model (Smith *et al.* 2001). It is based on the energy balance formulation of Jonsson (1990) for steady-state conservation of wave action along a wave ray:

$$\left(C_{ga}\right)_i \frac{\partial}{\partial x} \frac{C_a C_{ga} \cos(\mu - \alpha) E(\omega_a, a)}{\omega_r} = \sum \frac{S}{\omega_r} \qquad [3.25]$$

where the direction of the wave ray is given by

$$\mu = \tan^{-1}\left(\frac{C_{gr} \sin\alpha + U \sin\delta}{C_{gr} \cos\alpha + U \cos\delta} \right) \qquad [3.26]$$

E is the dimensionless spectral energy density, and S represents associated source and sink terms. The typical use for STWAVE and models like it is to quantify the change in wave parameters as waves move from deep water onshore. STWAVE is designed to work on a rectangular grid oriented roughly parallel to the shoreline. Wave conditions are specified as a 2-D spectrum at the outermost boundary. The model then propagates wave energy throughout the domain. STWAVE simulates depth-induced wave refraction and shoaling, depth and steepness-induced wave breaking according to the Miche (1951) criterion, simplified diffraction, wind-wave growth, and wave-wave interaction and whitecapping that redistribute and dissipate energy in a growing wave field.

STWAVE accepts two-dimensional spectra as input along with wind speed and direction for inclusion of wind-wave generation. Wave propagation is accomplished by the ray-tracing technique. Essentially the model looks back at previously calculated points within an angular interval, assessing the energy available at a given grid node by accumulating the appropriate portions of the frequency spectrum by distance and projected speed (SWAMP 1985). A model assumption is that the relative phases of the individual spectral components are random. This assumption, while limiting applicability in specific situations, allows STWAVE to neglect the tracking of wave phases.

Because STWAVE is a half plane model, energy can propagate shoreward but not seaward. Waves that are reflected from either shoreline or from a steep bottom features are neglected, as is forward wave scatter. STWAVE assumes mild bottom slope and negligible wave reflection.

The input conditions at the outer boundary are assumed to be uniform over the whole edge of the domain. As a steady state spectral model, STWAVE propagates waves over the whole domain instantly.

Other model assumptions include linearized refraction, shoaling, and radiation stress. This means that large, steep waves are not described well (Smith 2001). Also STWAVE assumes that currents are depth-uniform. STWAVE accepts wind input with the assumption that wind direction and speed are uniform over the whole grid.

When two-dimensional wave spectra are unavailable for input data, a parametric approximation of the two-dimensional spectra is used as model input. Development of spectra for STWAVE can be conducted using a module in the Surface-water Modeling System (SMS) (BYU-EMRL 1997). SMS is a grid development and pre- and post-processing environment for running various wave and current models. In SMS, spectral generation is performed according to the TMA one-dimensional shallow-water spectral shape (named for the three data sets used to develop the spectrum: TEXEL storm, MARSEN, and ARSLOE; see Smith *et al.* 2001) and a directional distribution function. According to the STWAVE Manual (Smith 2001), a TMA spectrum is generated from specified peak wave period (T_p), significant wave height, water depth, and a spectral peakedness parameter ($\gamma.$)̃.. Small values of the γ give broad peaks while large values give narrow peaks. The directional distribution of the spectrum is defined by a mean direction (α) and a spreading coefficient (*nn*) spreading the energy according to $\cos^{nn}\left(\alpha - \alpha_{nn}\right)$, where α is the spectral direction and α_{nn} is the mean wave direction. Guidance for selecting χ and *nn* is given in the SMS software according to Thompson *et al.* (1996).

4. TIDAL CIRCULATION

This chapter presents relevant information about tides, tidal currents, and circulation modeling. Mathematical formulae are presented both in general form and specifically as they are applied in the circulation model ADCIRC.

4.1. Tides and Tidal Currents

Wind-waves are by no means the only source for oceanic surface variation. In fact the ocean surface varies greatly due to tides. Tides induce sustained pressure gradients, which generate coastal currents (Kantha and Clayson 2000). Although there are other forces that modify coastal currents such as local wind stress and storm surges, tide-generated currents are particularly dominant in coastal inlet systems, forcing current velocities in excess of 2 m/s in some cases (Kantha and Clayson 2000).

Tidal waves are known as 'forced waves' because they are generated by periodic external (gravitational) forces. To completely describe the gravitational interactions between the earth and local heavenly bodies as well as the resultant forces at the surface of the earth's oceans is beyond the scope of this paper. Instead, a generalized conceptual framework will be presented. An introduction to the topic can be found in Wright *et al.* (1999) as well as a more detailed explanation in Kantha and Clayson (2000).

Gravitational forces are directly related to the product of the masses of the involved bodies and inversely proportional to the cube of the distance between them. Because of the proximity of the moon and the mass of the sun in relation to the other heavenly bodies, most observed changes in sea level can be described in a simplified earth-moon-sun relationship. Gravitational forces from the moon and sun cause bulges in the Earth's oceans. During new and full moons, periods when the earth, moon, and sun are roughly aligned, the moon and sun pull together on the Earth's oceans, creating periods of maximum tide range called spring tides. When the moon and sun are at right angles to each other relative to Earth, the net forces and the resultant tides are much smaller. Tides at these times are called neap tides. As the earth, moon, and sun move relative to each other, gravitational gradients are created, moving the tidal waves across the surface of the earth. Declination variation, orbital harmonics, and orbital eccentricity modulate the tidal forces diurnally (daily), semidiurnally (twice daily), fortnightly, and monthly. Frictional forces, the Coriolis force, inertia, and land masses further complicate the system, introducing phase lags and reflective action (Kantha and Clayson 2000).

If the conditions required for static equilibrium of the ocean in the presence of the tide producing forces at a given instant are fixed, it is possible to evaluate the equilibrium form of the surface of an ocean covering the entire earth. Deviation of this imaginary equilibrium is known as the potential of the tide producing force or tidal potential. In the mathematical development of tidal potential, it is useful to separate the observed forces into constituents, representing specific periodic changes in the earth-moon-sun system. For example the semidiurnal constituent known as M2 represents tidal variations with periods corresponding to the rotation of the earth relative to the moon. According to Kantha and Clayson (2000) in most cases only the four largest semidiurnal constituents (M2, S2, N2, K2) and diurnal (K1, O1, P1, Q1) are necessary to compute tides. Tidal constituents calculated by verified global tidal models can be applied as boundary conditions to drive regional circulation models

Wind-generated currents can also contribute to the residual current in near-shore seas. Simplistically, onshore winds tend to pile up water along the coast, creating a seaward-directed horizontal pressure gradient. This pressure gradient produces an associated current that is deflected by the Coriolis force to the right in the Northern Hemisphere. Northerly winds generate periods of coastal upwelling due to an offshore transport of surface waters (Wright *et al.* 1999). Since the focus of this paper is on the interaction of waves and currents at a tidal inlet, these wind-generated currents are ignored in the application, although the models applied do provide for wind input.

4.2. Circulation Modeling and the ADCIRC model

All oceanic circulation models solve some form of the continuity equations for mass and average momentum (Kantha and Clayson 2000). The basic equation for fluid conservation of mass was introduced in the wave-equation discussion above. Kolar *et al.* (1994) found that for large domains, the use of spherical coordinates was preferable to a Cartesian system in circulation models. The spherical form of the mass equation is given as

$$\frac{1}{(R+z)\cos\phi}\frac{\partial U}{\partial\lambda}+\frac{1}{(R+z)\cos\phi}\frac{\partial(V\cos\phi)}{\partial\phi}+\frac{1}{(R+z)^2}\frac{\partial\left[(R+z)^2 W\right]}{\partial z}=0 \qquad [4.1]$$

where R is the radius of the earth, λ is the longitude, ϕ is the latitude, and $U, V,$ and W are the velocity components in the north, east, and vertical directions. Note that $z << R$ so often the $R + z$ term is simplified to R. The depth averaged (two dimensional, depth integrated: 2DDI) form of the mass or continuity equation is used in ADCIRC (Luettich *et al.*1992), the finite element ocean circulation model employed in this study

$$\frac{\partial \zeta}{\partial t} + \frac{1}{R\cos\phi}\frac{\partial Uh}{\partial \lambda} + \frac{1}{R}\frac{\partial Vh}{\partial \phi} - \frac{Vh\tan\phi}{R} = 0 \tag{4.2}$$

where $\frac{\partial \zeta}{\partial t}$ is the time rate of change of the mean free surface boundary and *h* is the total water depth.

Along with the conservation of mass equation, the momentum of the fluid must be accounted for. Fundamental forces on the fluid must be taken into account including body forces, pressure, and frictional forces. Kolar *et al.* (1994) present the time-averaged conservation of momentum equation

$$\frac{\partial \rho \mathbf{v}}{\partial t} + \nabla \bullet (\rho \mathbf{v}\mathbf{v}) - \rho(\mathbf{g} + \gamma) + \nabla p - \nabla \bullet \tau + 2\Omega \times \rho \mathbf{v} = 0 \tag{4.3}$$

where γ is the gravitational pull by celestial bodies, p is the pressure of the fluid, and τ is a stress tensor. ADCIRC applies this relationship in non-conservative depth averaged form

$$\begin{aligned}
&\frac{\partial U}{\partial t} + \frac{1}{R\cos\phi}\frac{\partial U}{\partial \lambda} + \frac{V}{R}\frac{\partial U}{\partial \phi} - \left(\frac{U\tan\phi}{R} + f\right)V = \\
&-\frac{1}{R\cos\phi}\frac{\partial}{\partial \lambda}\left[\frac{p_s}{\rho_0} + g\zeta - g(\eta + \Upsilon)\right] + \frac{\tau_{s\lambda}}{\rho_0 h} - \frac{\tau_{b\lambda}}{\rho_0 h} + D_\lambda - B_\lambda
\end{aligned} \tag{4.4}$$

$$\frac{\partial V}{\partial t}+\frac{1}{R\cos\phi}\frac{\partial V}{\partial\lambda}+\frac{V}{R}\frac{\partial V}{\partial\phi}+\left(\frac{U\tan\phi}{R}+f\right)U=$$
$$-\frac{1}{R}\frac{\partial}{\partial\phi}\left[\frac{p_s}{\rho_0}+g\zeta-g\left(\eta+\Upsilon\right)\right]+\frac{\tau_{s\phi}}{\rho_0 h}-\frac{\tau_{b\phi}}{\rho_0 h}+D_\phi-B_\phi \qquad [4.5]$$

The expression $\left(\eta+\Upsilon\right)$ describes Newtonian tidal potential, earth tide, self attraction and load tide (Luettich *et al.*1992). The τ terms describe surface and bottom stress, D_* (where * can be either λ or ϕ) terms describe two-dimensional, depth integrated (2DDI) momentum diffusion, and B_* terms describe the 2DDI baroclinic pressure gradients. ADCIRC accepts both wind and radiation-stress input.

Other than body forces such as gravity and self-attraction, boundary conditions dictate the behavior of forcing in ADCIRC. It should be noted that all forces are gradually increased from zero to full strength at the beginning of an ADCIRC simulation to avoid potential numeric error by sudden forcing.

The mathematical method which ADCIRC uses to solve the governing equations is a Galerkin finite element method (Kolar *et al.* 1994). Use of the finite element scheme allows for computational efficiency by incorporating variable resolution over the model domain.

5. APPLICATION OF STWAVE AT HUMBOLDT BAY

This chapter presents the testing and validation of the STWAVE model at the entrance to Humboldt Bay. Issues resolved included defining appropriate domain, input data, as well as grid orientation.

5.1. Grid Domain and Orientation

Model application at Humboldt Bay began with the creation of a computational grid from bathymetric data. In this case, the bathymetric data came from the STRATAFORM project (Nittrouer 1996), a local high-resolution survey done by R. Flood (pers. comm.) and supplementary data from the GEOphysical DAta System (GEODAS) compiled by the National Geophysical Data Center.

In order to develop an appropriate bathymetric grid, a number of issues must be addressed, including the grid domain and orientation. Several different grids were tested to determine optimum grid configuration. Preliminary versions of the grid were based on suggestions from A. Militello (pers. comm., 2001) as well as from Smith (2001) and the STWAVE user's manual (Smith *et al.* 2001) to adequately resolve the features of the Humboldt Bay entrance, an initial grid resolution of 50 m was used (providing 12 grid points across the narrowest part of the entrance).

To the north of the entrance the grid domain extended to Trinidad Head to allow for future studies of sediment dynamics in this region (Fig. 5.1). Domain for the STWAVE grid included the Eel River because it is thought to be the dominant source of sediment for the Humboldt Entrance (Costa 1982). Several test cases were undertaken which further extended the southern edge of the model domain beyond Cape Mendocino. These cases showed that the change in modeled wave properties at the Humboldt Entrance by the inclusion of the Cape were insignificant. Inclusion of Cape Mendocino also increased model run time by 50%.

The only observational offshore wave data available in the vicinity of Humboldt Bay are hourly 1-D spectra measured at National Oceanic and Atmospheric Administration’s (NOAA) buoy 46022. This buoy lies offshore about 10 miles west of the Humboldt Bay mouth, in a water depth of roughly 250 m (Figure 5.1). Near-real time and historical quality-checked wave data from buoy 46022 are available from NOAA’s National Ocean Data Center (NODC) website (http://nodc.noaa.gov). Any use of these data to drive STWAVE, however, requires knowledge (or an assumption) of the dominant offshore wave direction.

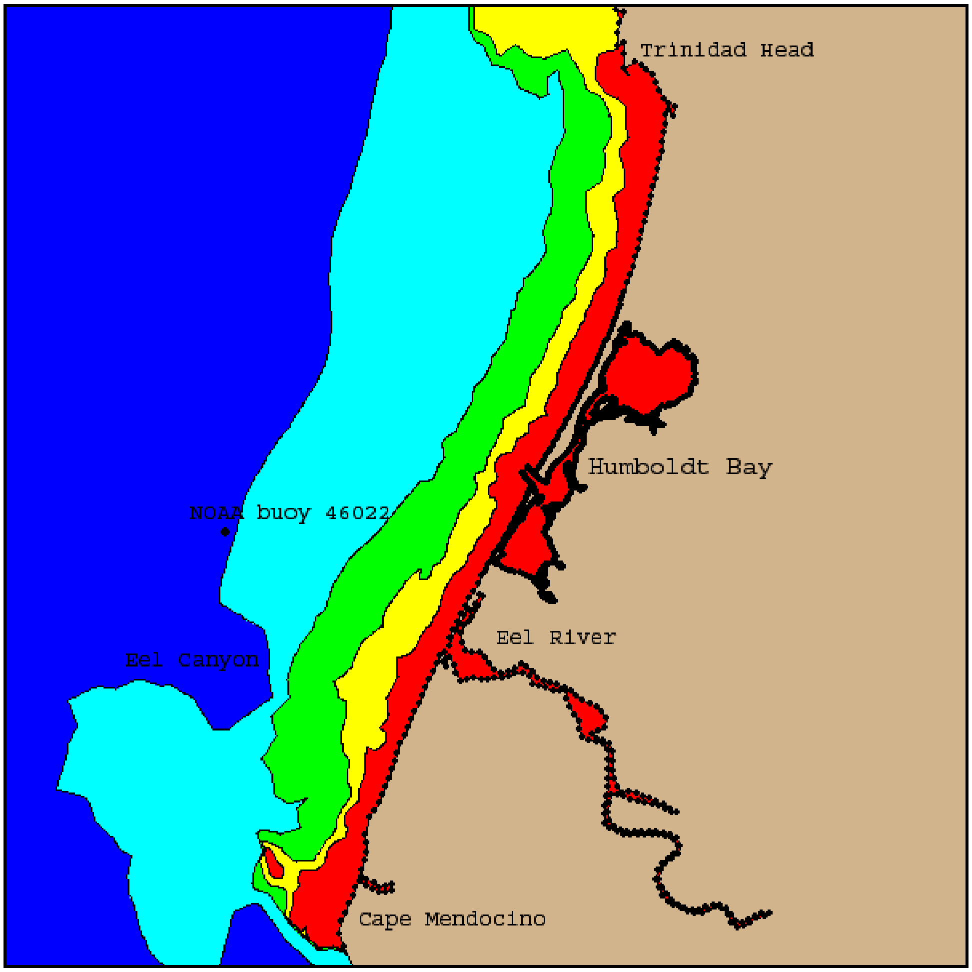

Figure 5.1. Humboldt Bay vicinity map showing NODC buoy 46022 and local bathymetry. Contours are drawn at 250, 100, 50, and 25 m. The dotted line represents the actual shoreline.

Waves approaching northern California can reach 1000 m in wavelength (G. Crawford, pers. comm., 2001). Waves are known to begin to be influenced by the presence of the ocean bottom when the depth is half of the wavelength. Because the depth at the buoy is less than *L/2* for the longest possible storm generated waves, there was initial concern that the longest possible waves approaching from offshore might be significantly modified by the variable bathymetry by the time the buoy was reached, so that the uniform outer boundary condition requirement of STWAVE might not be justified in this case. In order to test this concern, a new model grid was built that extended beyond the buoy into depths of 500 m. Grid cells were 100 m square, resulting in a 527 column by 910 row grid and 479570 calculation points. Six wave cases of different directions were run over this grid with sinusoidal waves 8 m in height, approximately 1000 m in wavelength, and with a 25 s period. STWAVE showed no significant changes for the test waves at depths greater than 200 m. Sample output from the initial model run as well as the grid domain can be seen in Figure 5.2. Note the lack of appreciable turning and wave height change until the waves are within approximately 10 km of shore, where the depths are about 180 m (*L*/5.5). Thus, bathymetric factors were determined to be insignificant in the vicinity of buoy 46022 and the outer boundary could legitimately be positioned in this region.

Additional model runs were conducted for more typical wave conditions. Climatological values of significant wave height and dominant period, corresponding to the months of January, April, and August (see Table 2.1), were used to develop wave forcing conditions for STWAVE. For each of these conditions, four different, specified dominant wave directions (295, 270, 245, and 220 degrees, defined clockwise from North) were also used, leading to a total of 12 different tests. Two-dimensional spectra were defined using [3.24]. The models were run on a shore normal grid whose outer boundary passed through the location of buoy 46022. At depths greater than 40 m, wave heights and wave directions were almost identical to the conditions at the outer boundary (see Table 5.2). Thus, for these climatological wave conditions, it was deemed reasonable to move the outer boundary in to roughly 40 m depth.

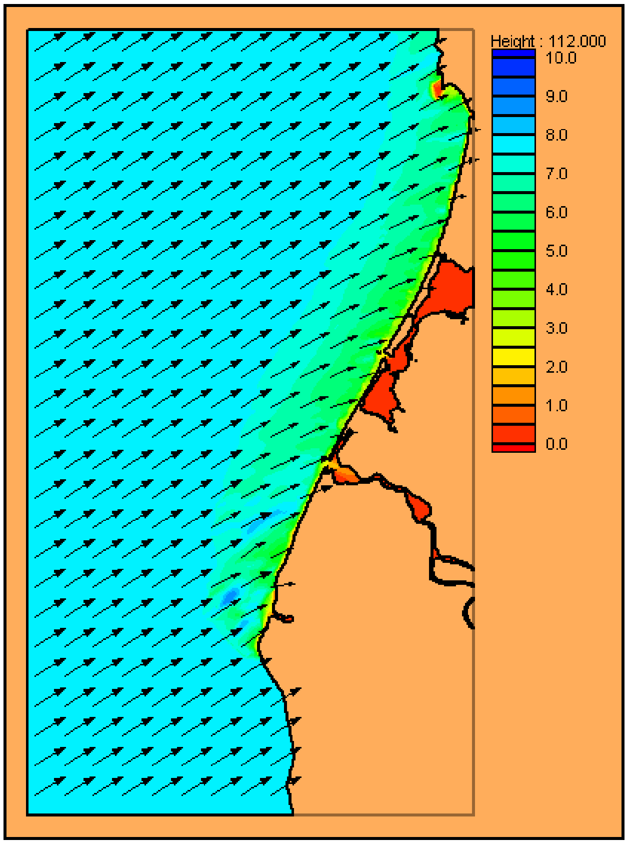

Figure 5.2. STWAVE grid domain and sample output for large, long wave study. The outer boundary is roughly 25 km offshore. Color scale shows wave height in m and vectors show wave direction for selected grid points. Note 112.000 is a numerical run identifier.

Table 5.1. Comparison between input wave properties, in 250 m water depth, and STWAVE model predicted wave properties at the 40 m isobath.

Month	**Offshore Wave Direction**	**Offshore Significant Wave Height (m)**	**Dominant Period (s)**	**Maximum Significant Wave Height in water > 40 m depth (m)**	**Maximum Turning in water > 40 m depth**
January	SW	3.1	13.2	3.2	≤ 3 °
	W	3.1	13.2	3.2	≤ 3 °
	NW	3.1	13.2	3.1	< 3 °
April	N	2.4	11.3	2.4	≤ 2 °
	NW	2.4	11.3	2.4	≤ 2 °
August	NW	1.7	8.7	1.7	≤ 2 °

That fact along with the cumbersome manual application of nested grids in the current version of the Surface-Water Modeling System software led to discarding the outer coarse grid in the wave-current interaction portion of this study. Instead only the fine (~40 m) resolution grid would be used and forcing conditions would be applied to its outer boundary.

5.2. Understanding Wind Input

As stated in the model overview, STWAVE accepts wind forcing as input in model runs with actual energy input directly dependent on fetch. Wind forcing is assumed to be half-plane (shoreward) and the wind field is assumed to be constant over the whole grid domain. It should be noted that the domain of the Humboldt model provides for as much as a 15 km fetch such that even a moderate wind (3 m/s) can generate waves over 0.3 m (Dean and Dalrymple 1991). Therefore in order to better apply STWAVE, a local wind study was completed.

STWAVE was set up to run with only wind input with a wind velocity of 16 m/s and slowly varying direction. It was found from this set of model runs that the wind input does affect model output, but not to the extent of our early estimates. Maximum significant wave height generated by the 16 m/s wind was only 0.17 m. Although this is an arguably significant value, field data showed that wind velocity was much closer to 6.3 m/s on average with peaks over 10 m/s for the study period. Because of these results and the nature of STWAVE as a propagation and transformation model (not a generational model), the majority of wave growth is assumed to have taken place before the waves are propagated onto the grid.

5.3. STWAVE Model Assessment – Case Study

In order to assess actual STWAVE performance at Humboldt Bay, it was necessary to compare model output to actual wave observations. For this purpose three events from February to May of 2001 were chosen as representative of a range of possible conditions at Humboldt Bay. The time period of the events coincided with the period of time that the USACE had placed moorings in the interior of Humboldt Bay, near the entrance (Figure 5.3). Water level was input for the time period from observations at each mooring.

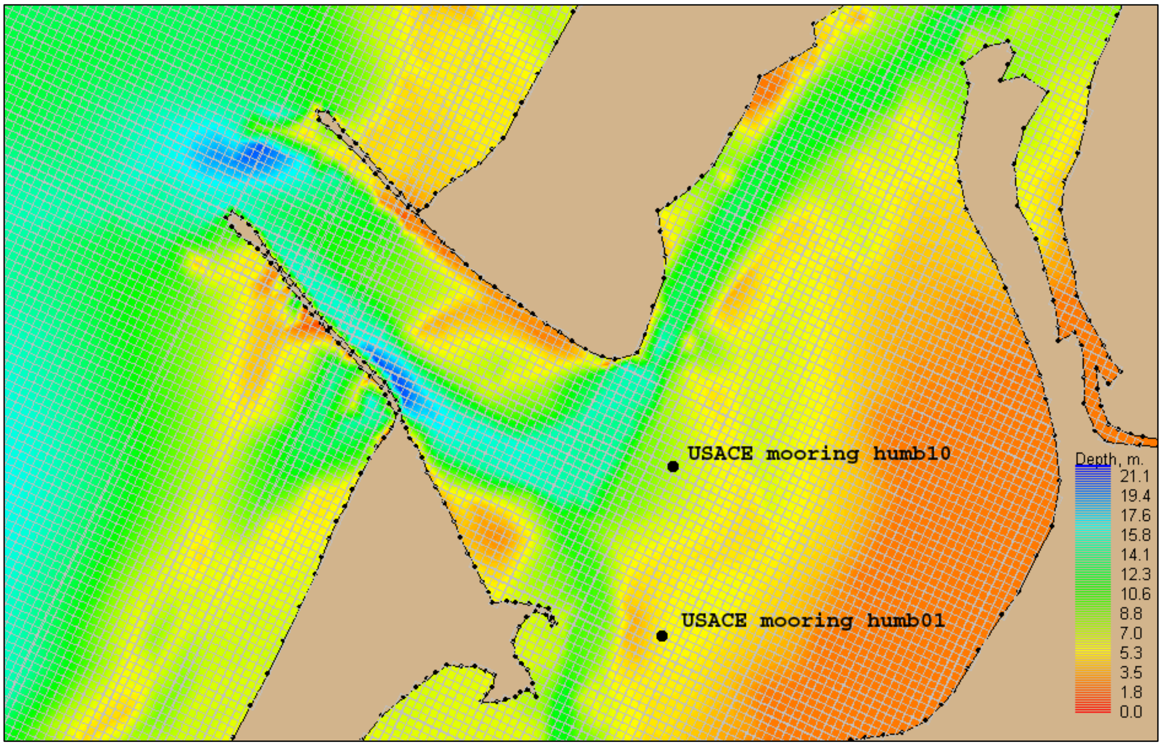

Figure 5.3. Location detail of USACE wave monitoring stations for the time period between February 8th, 2001 and June 25th, 2001. Mooring humb01 was used from February 8th to April 11th while mooring humb10 was used for the remainder of the study period.

The three events were selected to represent the following three cases: large waves offshore that produce large waves within the bay, large waves offshore that do not produce large waves in the bay, and moderate waves offshore that produce moderate waves in the bay. Table 5.2 shows the times of the three events and the associated significant wave heights offshore and in the bay. Figure 5.4 displays the longer-term time series of significant wave height offshore and in the bay, with the specified events identified.

Table 5.2. Three events chosen for STWAVE model assessment along with average wave heights both offshore at NODC buoy 46022 and at USACE mooring humb01 and humb10 in the Entrance Bay.

Event Period	**Average Offshore Significant Wave height During Event (m)**	**Average Significant Wave height at USACE mooring During Event (m)**
February 20-21, 2001	3.8	0.51
April 14-15, 2001	2.9	1.6
May 1-3, 2001	5.2	1.4

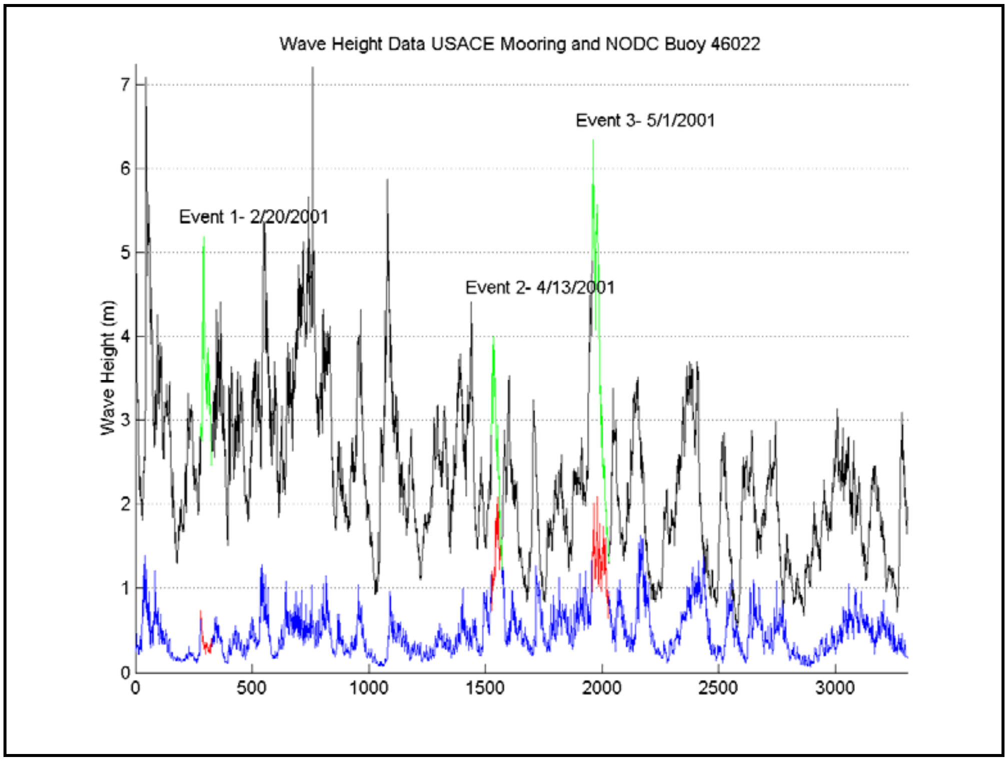

Figure 5.4. Plot of wave heights for the USACE observation period in the spring of 2001. Wave heights from NODC buoy 46022 are plotted in black, while wave heights at the moorings (humb01 and humb10) in the entrance bay are plotted in blue. Green and red lines represent the three chosen events.

The wave field was updated every hour based on the sampling rate of wave spectra at buoy 46022. Due to the lack of wave direction information at this buoy, care had to be taken in the evaluation of model performance. Initial wave spectra, calculated according to Hasselmann's (1973) shape parameters, were based on dominant period and mean significant height data from NODC buoy 46022. Frequency and directional spreading for the generated spectra are controlled by factors γ and *nn* which are associated with particular wave period conditions (Smith 2001). Guidance for choosing γ and *nn* is built into SMS. Because directional input was unavailable, three different wave directions were chosen; shore-normal (287 degrees), westerly (270 degrees), and parallel with the channel (253 degrees). These conditions were chosen based on the observation that typical wave crests approach normal to the inlet, while larger storm events approach out of the south (Costa 1982).

Table 5.3. Wave properties used to generate spectra for the three selected events. Wind input (magnitude and direction) was taken from National Weather Service observations at Woodley Island, in Humboldt Bay

	Event #1	**Event #2**	**Event #3**
Mean Wave Height	4 m	2.5 m	4.5 m
Dominant Period	12 s	8-14 s	14 s
Mean Wind Speed	4 m/s	3.5 m/s	7.3 m/s
γ	4	4	5
nn	10	8	16

The choice of offshore wave direction proved to be of primary importance as modeled wave heights could vary by 50% or more based on that factor alone. It was found that both the shore-normal case and the westerly wave case dramatically underpredicted wave heights within the entrance bay for these events (Figure 5.5, Figure 5.6, and Figure 5.7). Westerly wave cases performed the most poorly with the average difference between model and observed values being 51% of the average observed value for Event #1, 65% for Event #2, and 70% for Event #3. Model output for the shore-normal wave case was better, but still not satisfactory. Rather than exhibit the variability of wave energy in the entrance as was observed by the USACE mooring, model output showed smooth sine-waves with energy mirroring the rise and fall of the tides. In the shore-normal wave case, the average differences between observed and model predicted values was 30% for Event #1, 44% for Event #2, and 51% for Event #3. For the case in which waves were directed down the entrance channel, model results were generally in better agreement with the observations.

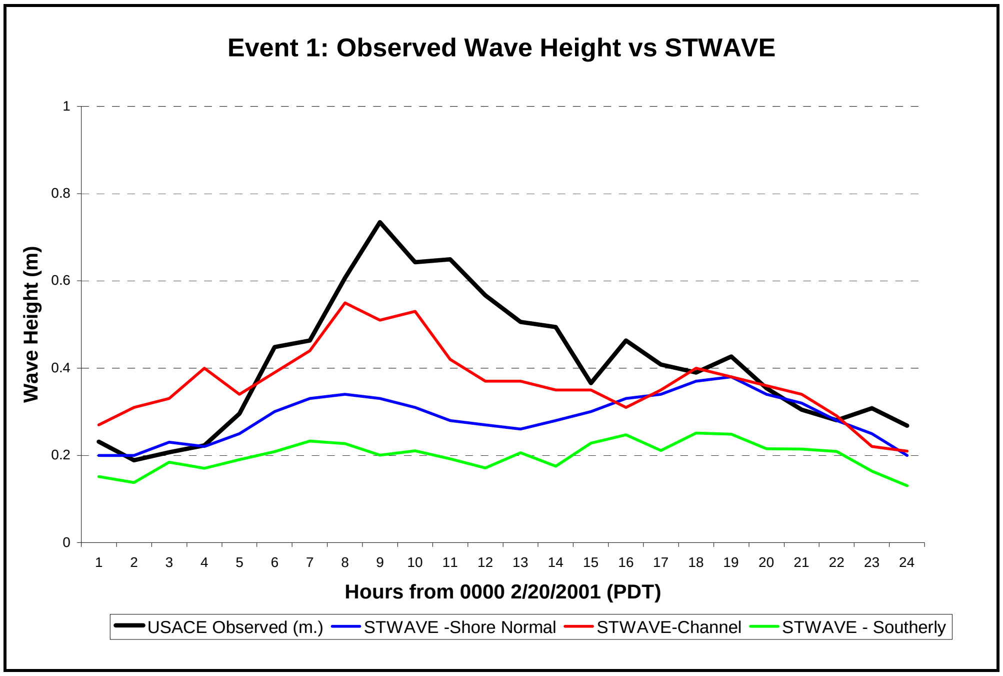

Figure 5.5. Comparison of STWAVE model output to USACE mooring data at humb01 for Event #1.

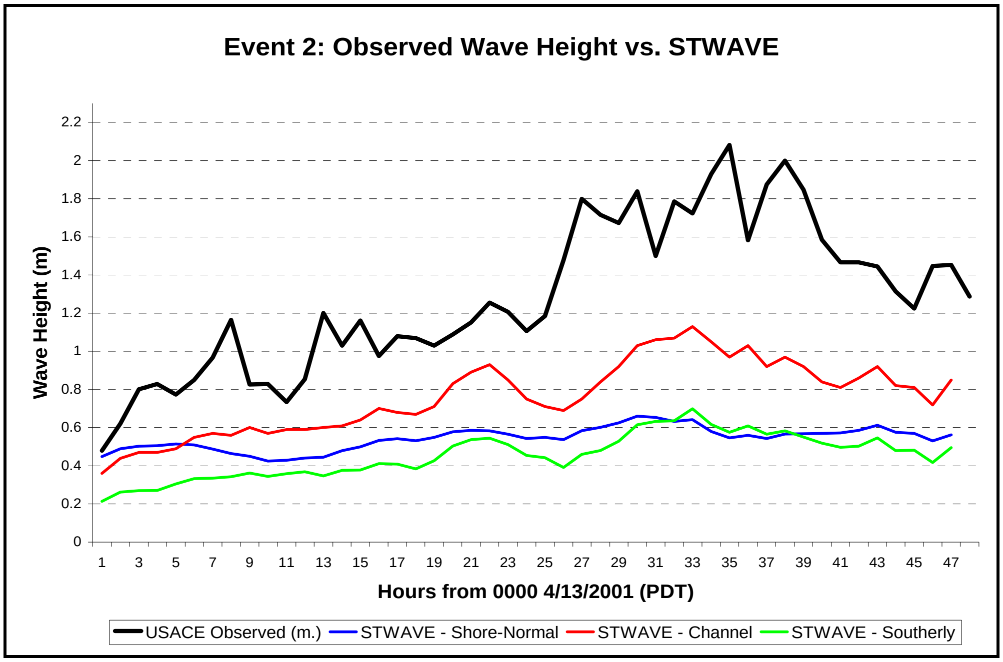

Figure 5.6. Comparison of STWAVE model output to USACE mooring data at humb10 for Event #2.

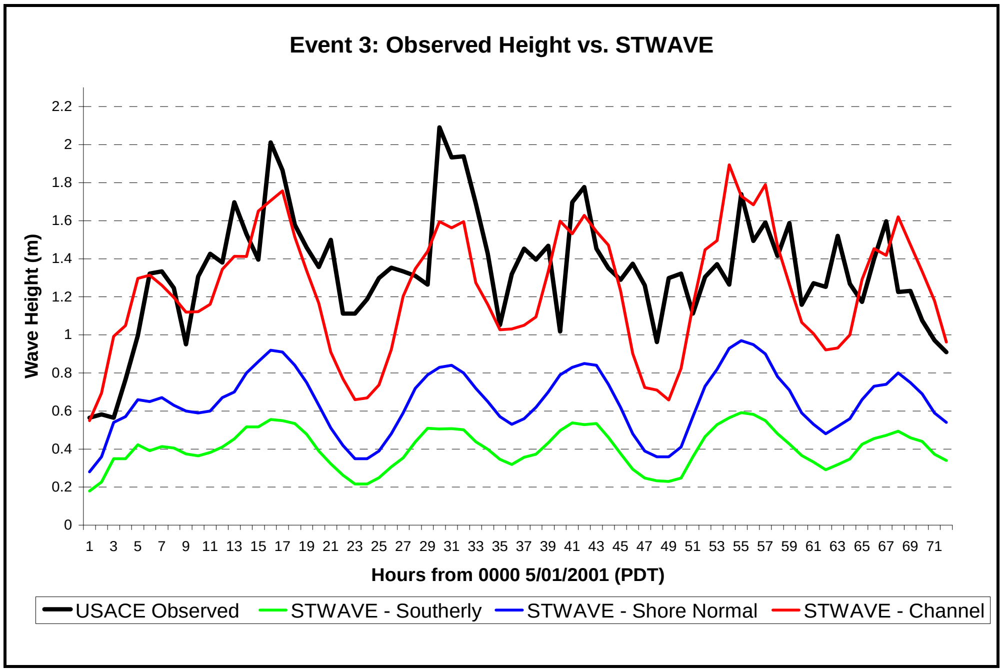

Figure 5.7. Comparison of STWAVE model output to USACE mooring data at humb10 for Event #3.

Even in the case where wave energy was directed straight down the entrance channel, the model underpredicted the observed amount of energy at the moorings. According to A. Militello (pers. comm., 2001) grid orientation is one of the potential factors for underprediction.

5.4. Grid Orientation Case Study

In order to understand the contribution of grid orientation to solution accuracy, especially in the context of this potential shadowing problem, another grid was built, this time aligned so that the jetties were parallel to the grid rows. The new grid will be referred to in this paper as the jetty orientation while the previous grid alignment will be referred to as the original, or cross-shore, orientation. The jetty orientation produced a grid with 32% more calculation points than the original cross-shore grid.

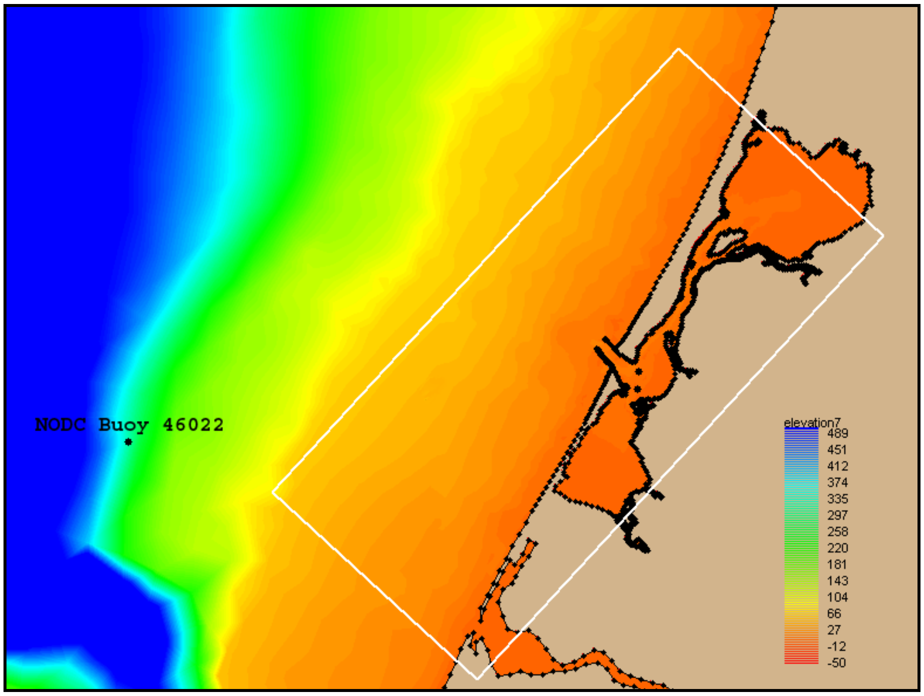

Figure 5.8. Outline of the STWAVE grid with local bathymetry. This grid was built to determine the importance of jetty-grid orientation on wave energy propagation.

For the comparison, each wave event was rerun on the jetty-aligned grid for both the shore-normal and channel offshore wave directions. Spectra were generated with the same shape parameters (significant wave height, dominant period, *nn*, and γ) with directional input changed to compensate for the grid rotation.

In general, model output from the jetty orientation differed significantly from the cross-shore model output. For Event #1, the model over the jetty aligned grid predicted a spike of wave energy late in the event when neither mooring observations nor model predictions from the cross-shore grid did. This spike corresponds with winds that were likely ignored in the cross-shore grid orientation because of STWAVE’s half-plane assumption. Overall, the jetty orientation did not increase model accuracy for Event #1. Mean difference between model output and observed values is summarized in Table 5.4.

For Event #2, a 24-hour period was selected for comparison with the jetty-aligned model results. For the jetty grid orientation, results showed that wave direction does not significantly impact model output. Shore-normal waves were modeled to be higher in the Entrance Bay than the channel directed waves for the jetty orientation. For the comparison period, the jetty orientation more closely modeled observed data than the cross-shore orientation (Figure 5.10). In fact rms error in predicted wave height was reduced by 37%. On the whole, however, the jetty orientation still failed to model observed trends in wave height, often predicting increases or decreases in wave energy inconsistent with mooring data.

For Event #3, results were difficult to interpret. Again, for a given wave direction, the jetty orientation increased the amount of energy that STWAVE modeled in the Entrance Bay compare to the shore-normal grid. Poor performance in tracking wave height trends increased error in the model predicted wave heights over the cross-shore case also. Comparison of wave breaking fields indicated that the cross-shore grid predicted more breaking on the shoal in the entrance channel than the jetty orientation, especially on a low tide. This difference led the jetty orientation model to generally over-predict the observed wave heights at the USACE mooring. For reference, grid cell size in relation to entrance channel features can be seen in Figure 5.3.

Table 5.4. Comparison of mean difference (in m) between model results and USACE mooring observations for two STWAVE grid orientations. For each event two initial wave directions were chosen: one aligned with the Entrance Channel of Humboldt Bay and the other approximately shore-normal. Differences were calculated by subtracting model predicted wave heights from observed values at USACE mooring locations.

	Grid Orientation			
	Shore-normal		**Channel**	
Waves:	**Shore-normal**	**Jetty-aligned**	**Shore-normal**	**Jetty-aligned**
Event #1				
Mean Difference (m)	0.12	0.11	0.12	0.12
Standard Deviation (m)	0.13	0.11	0.22	0.19
Median Difference (m)	0.07	0.05	0.12	0.13
Event #2				
Mean Difference (m)	0.22	0.18	0.16	0.14
Standard Deviation (m)	0.13	0.11	0.07	0.07
Median Difference (m)	0.19	0.19	0.14	0.12
Event #3				
Mean Difference (m)	0.69	0.10	0.19	0.24
Standard Deviation (m)	0.24	0.29	0.35	0.34
Median Difference (m)	0.71	0.11	0.13	0.09
ALL EVENTS (COMBINED)				
Mean Difference (m)	0.55	0.23	0.18	0.18
Standard Deviation (m)	0.31	0.33	0.60	0.54
Median Difference (m)	0.57	0.23	0.09	0.20

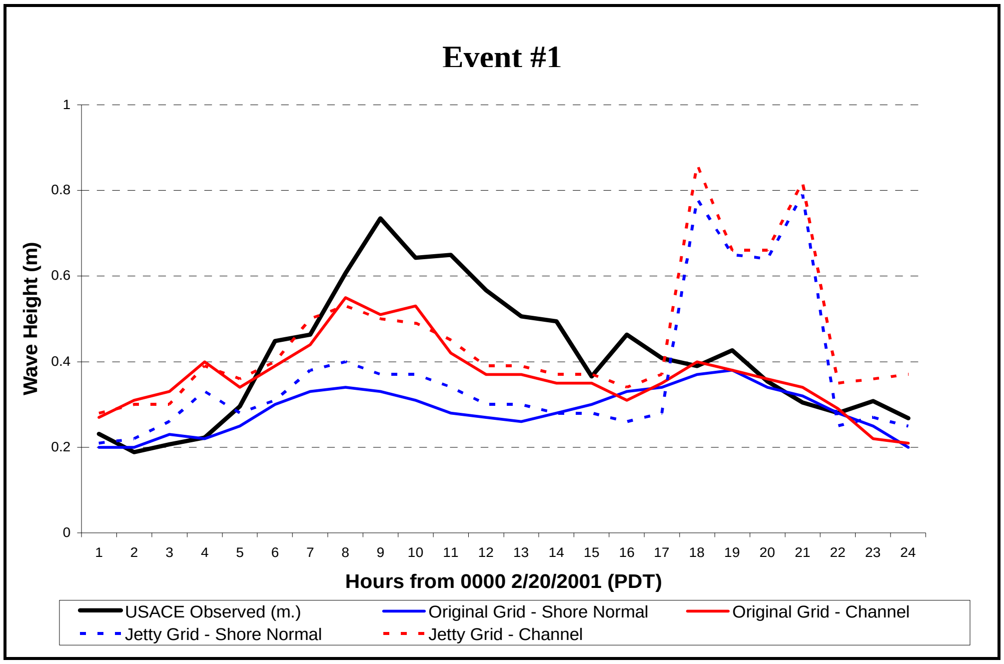

Figure 5.9. Time-series plot of STWAVE model output compared to USACE mooring data for Event #1. The shore-normal oriented grid is referred to as the Original Grid while the jetty aligned grid is denoted Jetty Grid.

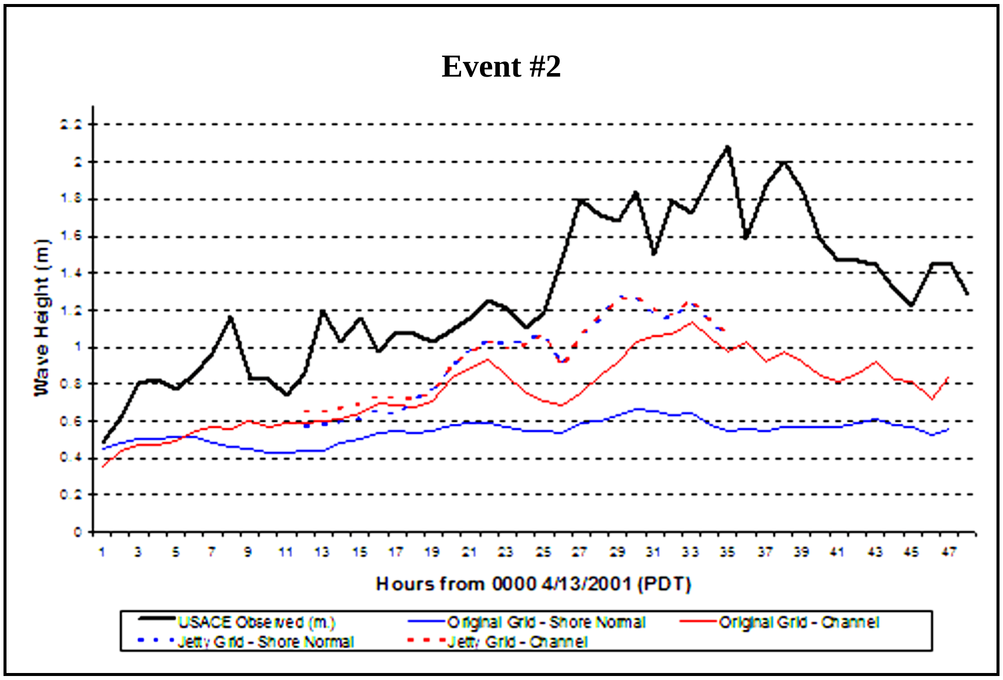

Figure 5.10. Time-series plot of STWAVE model output compared to USACE mooring data for Event #2. The shore-normal oriented grid is referred to as the STWAVE case while the jetty aligned grid is denoted Jetty Grid.

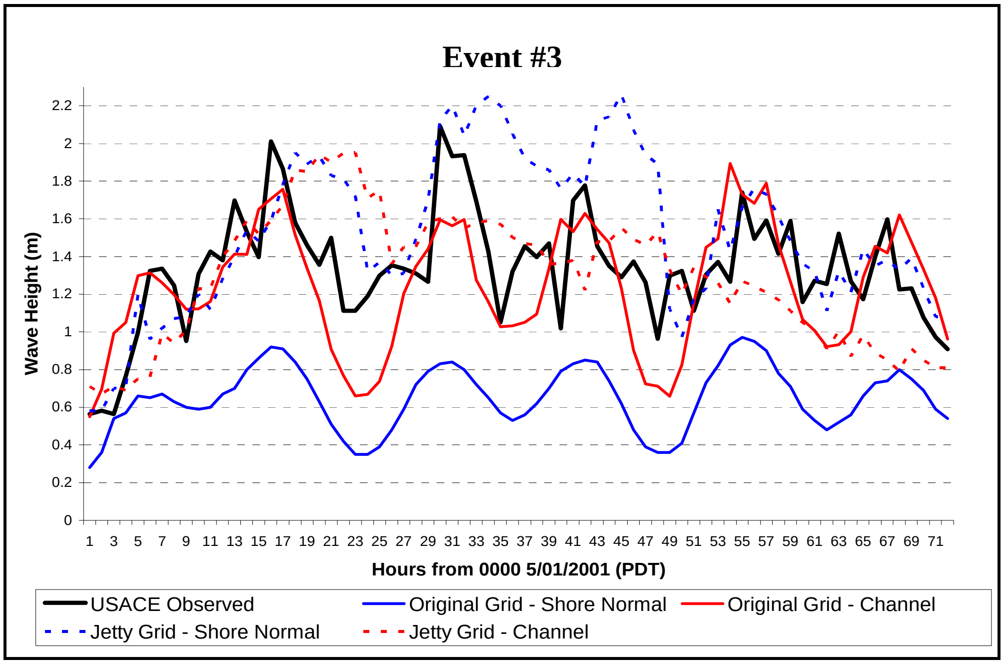

Figure 5.11. Time-series plot of STWAVE model output compared to USACE mooring data for Event #3. The shore-normal oriented grid is referred to as the Original Grid while the jetty aligned grid is denoted Jetty Grid.

In conclusion the grid-orientation study highlighted the complexity of modeling waves at Humboldt Bay. In general, the jetty orientation grid decreased mean difference between modeled and observed wave heights within the Entrance Bay compared with the original grid. At the same time, the jetty-orientation solutions did not always follow the trends in wave height at those same locations as well as the cross-shore orientation. Other factors, such as wind input and current, were not isolated in this study. Overall, Table 5.4 suggests that the best agreement overall (in terms of mean difference, standard deviation, and median difference between modeled and observed values) is obtained from offshore waves aligned with the channel. While grid orientation did modify the results to some degree, the shore-normal grid provided slightly better results than the jetty oriented grid overall.

6. APPLICATION OF ADCIRC AT HUMBOLDT BAY

This chapter presents the testing and validation of the ADCIRC model at the entrance to Humboldt Bay. Issues resolved included refinement of bathymetric data, model domain, and mesh resolution.

6.1. Grid Domain and Development

A preliminary ADCIRC model grid was provided by the USACE (A. Militello, pers. comm.; see Figure 6.1). This hemispherical grid covered the Pacific Coast from midway down the Baja Peninsula to the Alaskan border. The grid appeared to be reasonably accurate with some small amount of adjustment needed for tuning tidal currents in and out of Humboldt Bay itself (A. Militello, pers. comm.). When examining the bathymetry of the USACE grid in the Humboldt region, however, it was noticed that several large coastal features were missing from the bathymetric data.

The original grid domain extended northward of available tidal forcing data used in running the model. In the revised grid, the domain was reduced in size to be brought within the bounds of available forcing data. The smaller domain also reduced the number of mesh nodes by ~5%.

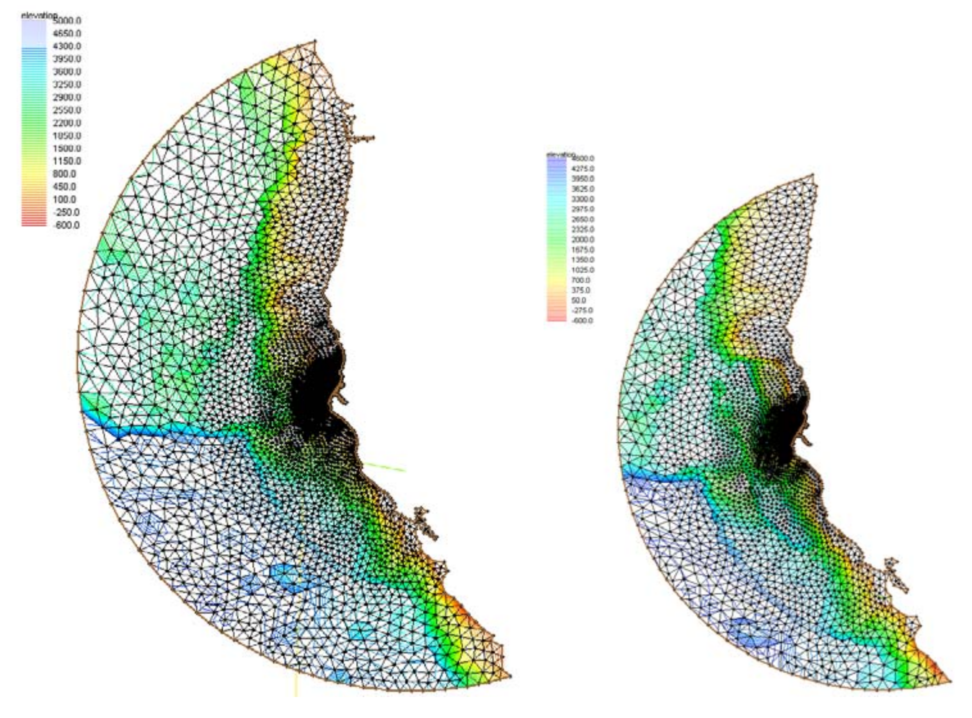

Figure 6.1. Comparison of original USACE ADCIRC mesh (left image) to new mesh (right image). The number of nodes was reduced by 5% and bathymetry was corrected.

The bathymetry of the mud flats in the Arcata Bay and South Bay are known to be inaccurate. This issue could be a source of error for the ADCIRC model, changing both current velocities and shifting tidal peaks (A. Militello, pers. comm.). Recently the USACE completed a bathymetric survey of the Arcata Bay and South Bay, but these new data were not incorporated into the model for this study.

6.2. Preliminary ADCIRC Model Assessment

Initial assessment of the ADCIRC model was limited to the uncoupled case. Forcing data was taken from SMS's built-in LeProvost data and tidal constituents (LeProvost *et al.* 1994). Tidal constituents used in this study included K1, O1, M2, N2, S2, K2, P1, and Q1. ADCIRC was set to ramp forcing according to the hyperbolic tangent function over 2 days with a time-step of 1.5 seconds. ADCIRC tidal height predictions for the month of August 2001 were compared to observations at the NOAA/NOS gauge at the Coast Guard station on the North Spit of Humboldt Bay. Performance was good, with all model values within 6% of observations and a majority of the model values within 4% of observed water-level. A sample day is shown in Figure 6.2. Mean difference between modeled values and observed values at the tide station for the month was 0.04 m with a standard deviation of 0.017 m.

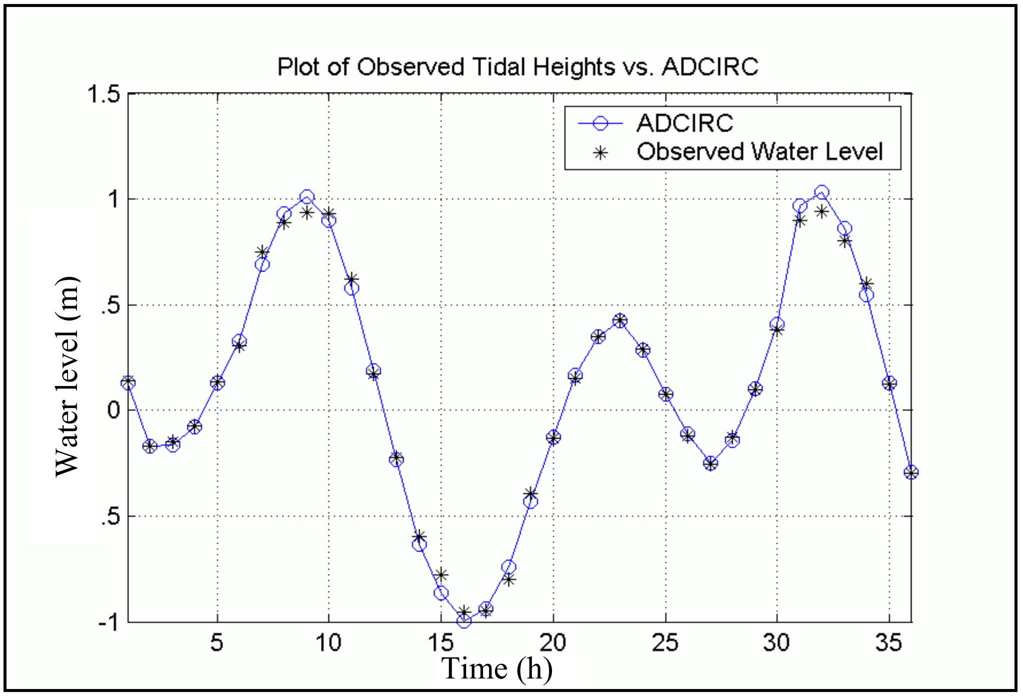

Figure 6.2. Typical ADCIRC model output compared to observations at NOAA/NOS tide gauge 9418767 ($40^{\circ}46.0'\,N\ 126^{\circ}13.0'\,W$) on the North Spit of Humboldt Bay.

7. COUPLED MODEL APPLICATION

In this chapter, relevant issues to the coupling of STWAVE and ADCIRC are discussed. A performance analysis based on a comparison of observed data and model output is presented.

7.1. Model Coupling Mechanics

In the past, coupling the STWAVE and ADCIRC models was accomplished on a step-by-step basis (A. Militello, pers. comm.). Manual interpolation of current and wave fields to the different meshes was necessary, requiring the model runs to be stopped and restarted regularly. Recently, development of the SMS software has included a new Steering Module that automated model control and interpolation of vector and scalar fields between models (Zundel *et al.*, 2002).

SMS software provides a graphical interface for mesh and forcing setup and post-processing for a variety of models, including the two applied in this study. For this wave-current interaction investigation, an ADCIRC simulation is loaded into SMS followed by a corresponding STWAVE simulation. Each model is set up as it would be if it were to run for the complete simulation individually with details found in Zundel *et al.*, (2002).

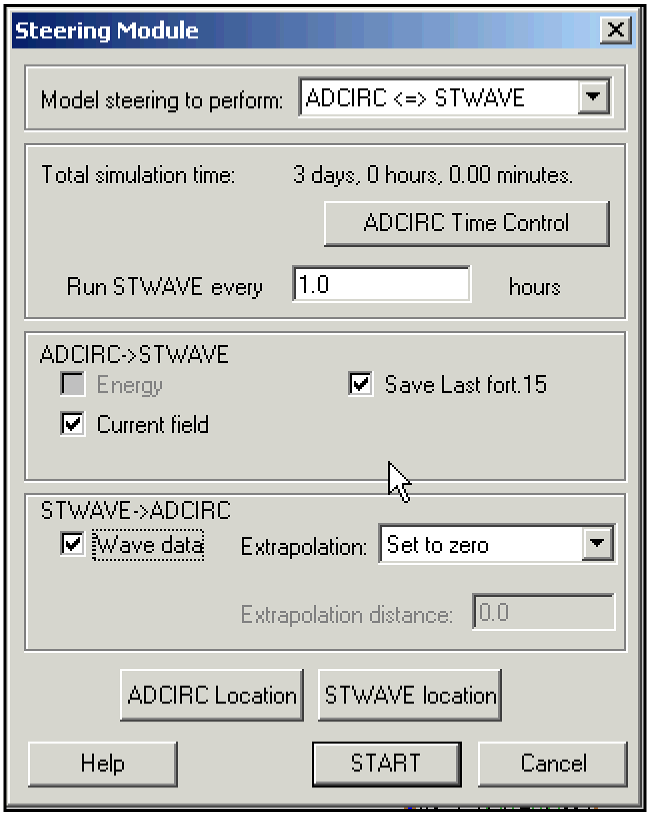

Steering Module

Model steering to perform: ADCIRC <=> STWAVE

Total simulation time: 3 days, 0 hours, 0.00 minutes.

Run STWAVE every 1.0 hours

ADCIRC->STWAVE

☐ Energy

☑ Save Last fort.15

☑ Current field

STWAVE->ADCIRC

☑ Wave data

Extrapolation: Set to zero

Extrapolation distance: 0.0

Figure 7.1. SMS steering module control dialog with options checked to provide full two-way coupling between ADCIRC and STWAVE at 1 hour intervals.

The Steering Module, used to control communication between the models, is set up to indicate the type of coupling, the times at which the models communicate, and which data types will be passed between the models (Figure 7.1). The Steering Module uses the term “Wave data” to indicate the radiation stress tensors calculated by STWAVE. If this option is checked, ADCIRC calculations will include wave-generated currents. Left unchecked, this option will leave ADCIRC calculations unchanged from uncoupled versions of the model. Checking the “Current field” control box indicates that the currents from the ADCIRC solutions will be interpolated to the STWAVE grid as current input. Water level variation is included in coupling by changing the bathymetry of the STWAVE grid according to calculated tidal heights from ADCIRC. It is important to note that ADCIRC still requires ramped forcing functions so the steering module slowly increases wind, radiation stress, and tidal forcing functions over a period of between one and five days as recommended by Zundel *et al.* (2002).

For the modeling applications discussed here, we shall consider three types of model coupling: uncoupled, in which STWAVE and ADCIRC run independently of each other; one-way coupling, in which currents from ADCIRC are not used as input to STWAVE but STWAVE radiation stress tensors are input into ADCIRC; and two-way (or full) coupling, in which ADCIRC currents influence STWAVE and radiation stresses from STWAVE influence ADCIRC.

Sudden changes in the wave field can also introduce error into the ADCIRC solution under coupling. Conventionally wave inputs are held steady for at least an hour at a time (Smith 2001). The Steering Module in SMS deals with this potential problem by running the STWAVE model for two consecutive sets of inputs and applying the changes in the wave field to ADCIRC using linear interpolation. When the Steering Module begins a run, STWAVE is initially run twice, for hours 0 and 1, and the radiation stress gradients for each solution are interpolated in time for input to ADCIRC (Zundel *et al.,* 2002). For the two-way coupled test runs, the input current field used by STWAVE was updated every hour. Further work could identify the sensitivity of the model system to update frequency but such an effort was considered beyond the scope of this paper.

7.2. Model Assessment

The same three observed wave events discussed in Section 5.3 and 5.4 were used to analyze the performance of the coupled model (see Figure 5.4, Table 5.2). Each event was modeled using two different input wave directions and two different coupling modes. Input wave directions were the shore-normal and the channel directions, as described previously. Uncoupled, one-way and two-way coupling options were tested (note, however, that STWAVE results for uncoupled and one-way coupled runs are, by definition, identical). Wave heights at USACE moorings humb01 and humb10 were used again for assessment of model performance along with tidal heights at the NOAA/NOS tide station on the North Spit of Humboldt Bay.

Wave heights were chronically underpredicted in the uncoupled and one-way coupled cases relative to the observations (see Table 7.1). Results from the two-way coupling cases, however, were closer to the observations overall.

Table 7.1. Comparison of wave height differences between USACE observations and STWAVE model output at mooring locations humb01 and humb10 for uncoupled and two-way coupled model cases. Positive values indicate model underprediction.

	Coupling Mode			
	Uncoupled/One-Way		**Two-way**	
Waves:	**Shore-normal**	**Channel**	**Shore-normal**	**Channel**
Event #1				
Mean Difference (m)	0.12	0.11	0.10	0.08
Standard Deviation	0.13	0.11	0.18	0.12
Median Difference (m)	0.07	0.05	0.05	0.05
Event #2				
Mean Difference (m)	0.22	0.18	0.11	0.10
Standard Deviation	0.13	0.11	0.17	0.12
Median Difference (m)	0.19	0.19	0.07	0.08
Event #3				
Mean Difference (m)	0.69	0.10	0.17	0.06
Standard Deviation	0.24	0.29	0.18	0.14
Median Difference (m)	0.71	0.11	0.14	0.09
All Events (Combined)				
Mean Difference (m)	0.55	0.23	0.13	0.07
Standard Deviation	0.31	0.33	0.18	0.13
Median Difference (m)	0.57	0.23	0.09	0.20

Tidal height predictions remained mostly unchanged from uncoupled model predictions. One way coupling and two-way coupling differed from each other by 1-3% in tidal height predictions at the North Spit tidal station. Interestingly they differed by as much as 10% from observed values, particularly at the peaks of the tidal range, about twice the error of the uncoupled model. Sample output for both two-way coupled model runs and uncoupled model runs is shown in Figure 7.2.

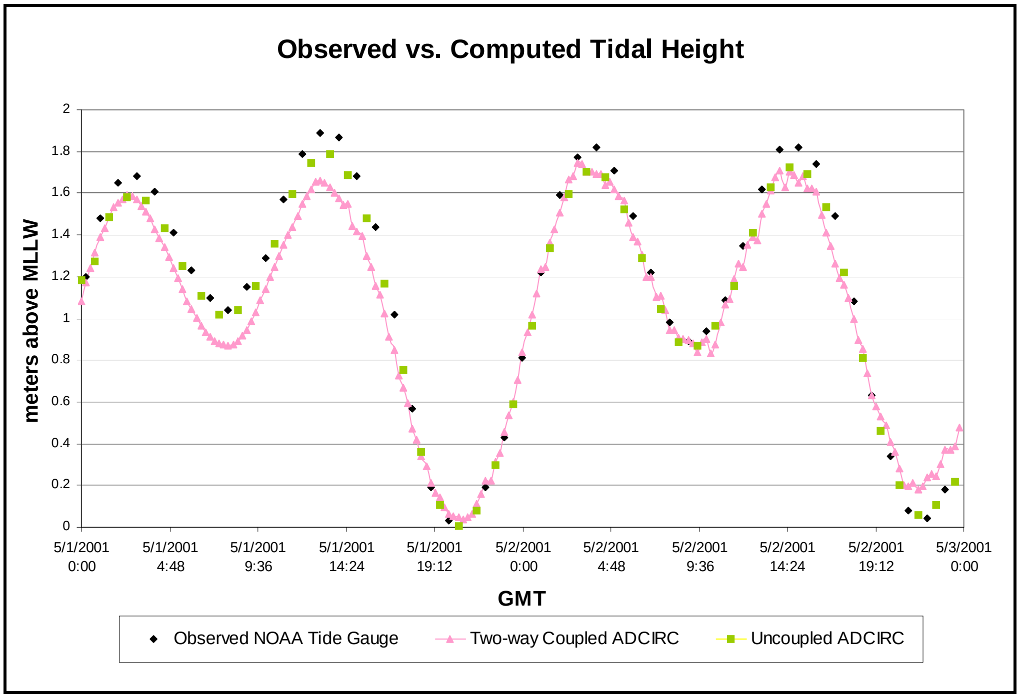

Figure 7.2. Output from two-way coupled ADCIRC/STWAVE model and uncoupled ADCIRC model compared to observed values at NOAA/NOS tide gauge 9418767 ($40^{\circ}46.0'\ N\ 126^{\circ}13.0'\ W$) on the North Spit of Humboldt Bay.

Several interviews with local surfers and others that frequent the Humboldt Entrance were conducted to determine the general pattern of currents in that region (W. Hoopes 2001 and B. Taylor, 2002, pers. comm.). General pattern of currents in and around the inlet, particularly the north jetty were described to be very similar to model predictions. Graphical output of tidal current patterns were shown to two surfers and they confirmed the presence of some key features in the circulation model : a strong circulation cell with an offshore rip current which is consistently present on the north side of the north jetty, and an onshore current immediately on the channel side of the north jetty (Figure 7.5).

Current speeds for the coupled model runs were unreasonably high for the climatological events. Current speeds as high as 28.4 m/s both along the edges of the channel and in the near-shore region were predicted by the one-way model, while speeds of 20.3 m/s were predicted by the two-way coupled model. According to Costa and Glatzel (2002) current rates for the channel at maximum ebb are on the order of 2.1 m/s, or about an order of magnitude less than model predictions. Although no specific information is available for the Humboldt region, typical longshore currents have mean values of 0.3 m/s or less, but values exceeding 1 m/s can occur in storms (Visser 1991). In the presence of large waves, currents may be higher, but not by an order of magnitude.

7.3. Coupling and ADCIRC Mesh Resolution

Conversations with M. Cialone (pers. comm.) suggested that a potential cause of circulation model miscalculation could be inadequate mesh resolution in the near-shore region. She suggested that a resolution on the order of 50 m in the near-shore region rather than the existing 160 m resolution would be adequate. In order to meet this guideline, a new finite element grid was built using the adaptive tessellation routine included with SMS (Figure 7.3 and Figure 7.4). The new grid provided a resolution of up to 35 m in the near-shore region.

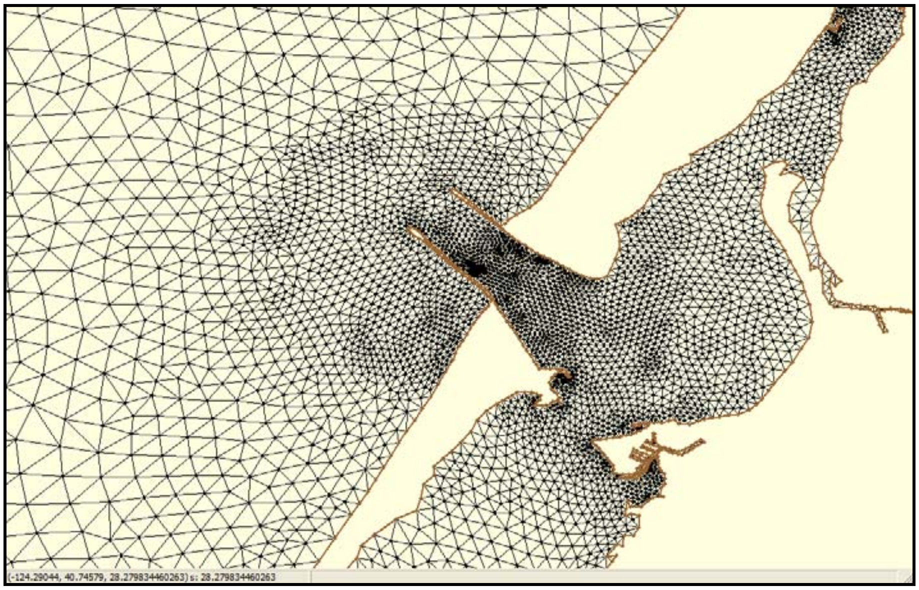

Figure 7.3. Original ADCIRC mesh with resolution near the entrance of Humboldt Bay. Actual resolution ranged between 50 and 500 m over the surf-zone.

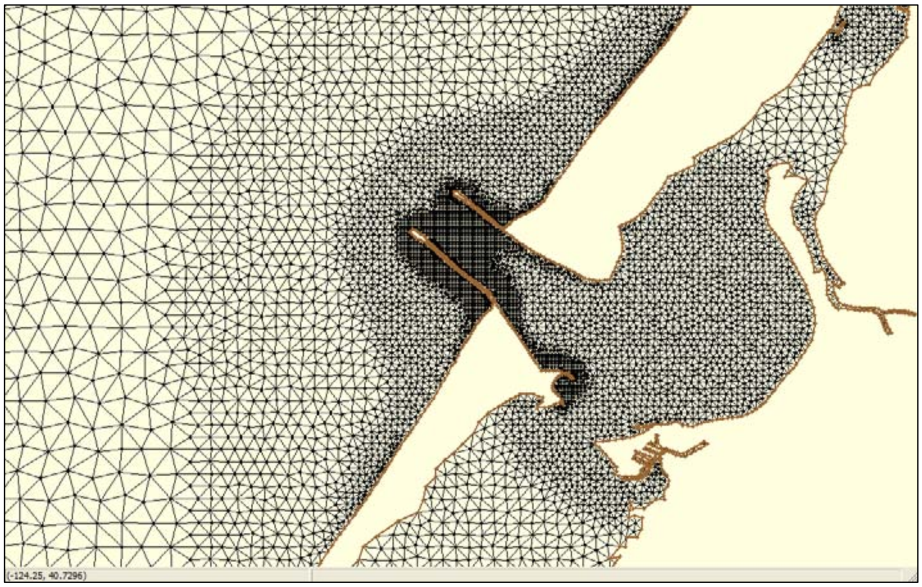

Figure 7.4. New ADCIRC mesh generated with SMS tiling algorithm at the Humboldt Bay entrance. Resolution in the surf-zone ranges between 35 and 75 m with a majority of the entrance channel at 35 m.

Results from the new mesh for the three observed wave events yielded nearly identical overall wave height and water level differences as for the coarser grid, but maximum currents were much more reasonable. For channel currents, the one-way model predicted a maximum velocity of 4.2 m/s for peak flood tide in Event #3 and 4.1 m/s for the maximum ebb. The two-way model predicted channel currents as much as 4.2 m/s on maximum flood tide and 3.9 m/s for maximum ebb. Interestingly, the maximum velocities appeared to be wave-driven as they were directed inward, along the shallow north side of the entrance, during flood tides.

Table 7.2. Summary of maximum predicted current velocities for different climatological cases and different grid resolutions. See Figure 5.4-Figure 5.7, and Table 5.2 for details of wave height.

	Max Current Velocity (m/s) Event #1	**Max Current Velocity (m/s) Event #2**	**Max Current Velocity (m/s) Event #3**
Original Grid:			
One-way coupling (STWAVE -> ADCIRC)	16.4	15.9	20.3
Two-way coupling (STWAVE<->ADCIRC)	19.3	19.1	28.4
New Grid:			
One-way coupling (STWAVE -> ADCIRC)	4.1	3.1	4.2
Two-way coupling (STWAVE<->ADCIRC)	4.1	3.2	4.2

For this event, both the one-way and two-way coupled models predicted inward directed current along the north jetty at all stages of the tide. In particular, during ebb tide, while the majority of the current was directed seaward, there was still a narrow band of current directed into the bay itself along the north jetty, where water depths are relatively shallow (Figure 7.5).

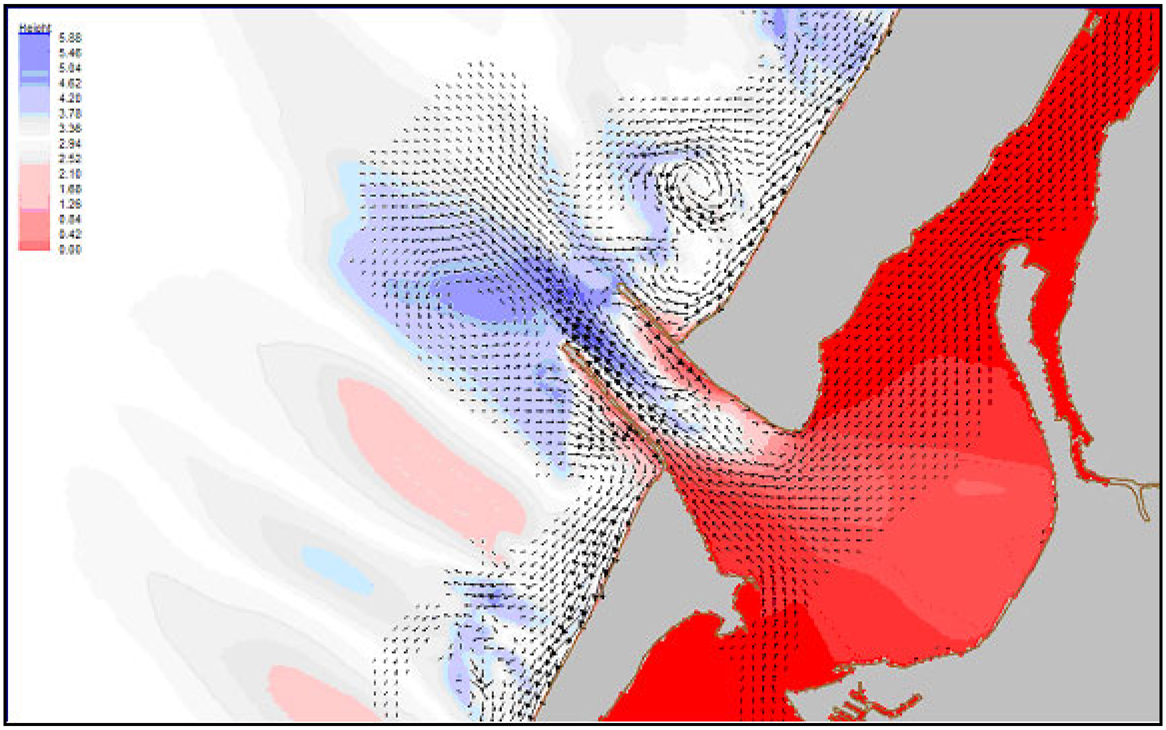

Figure 7.5. Model output for refined model grid during peak ebb tide (1000 hours 5/01/2001 PDT). In this case waves were directed approximately down the channel with an initial significant height of 3.13 meters and dominant period of 14.27 seconds. Color indicates wave height while vectors indicate current.

For the refined grid case, there was also improvement in the wave height prediction at USACE moorings from previous coupled cases. Difference between model predictions and observed values for two-way coupling was reduced 35% compared to previous model runs in the shore-normal wave case. In general, cases in which waves were directed down the channel were more consistent with the observations than cases with a shore normal offshore wave direction. The mean error for all cases was 0.09 m, slightly more than uncoupled model runs.

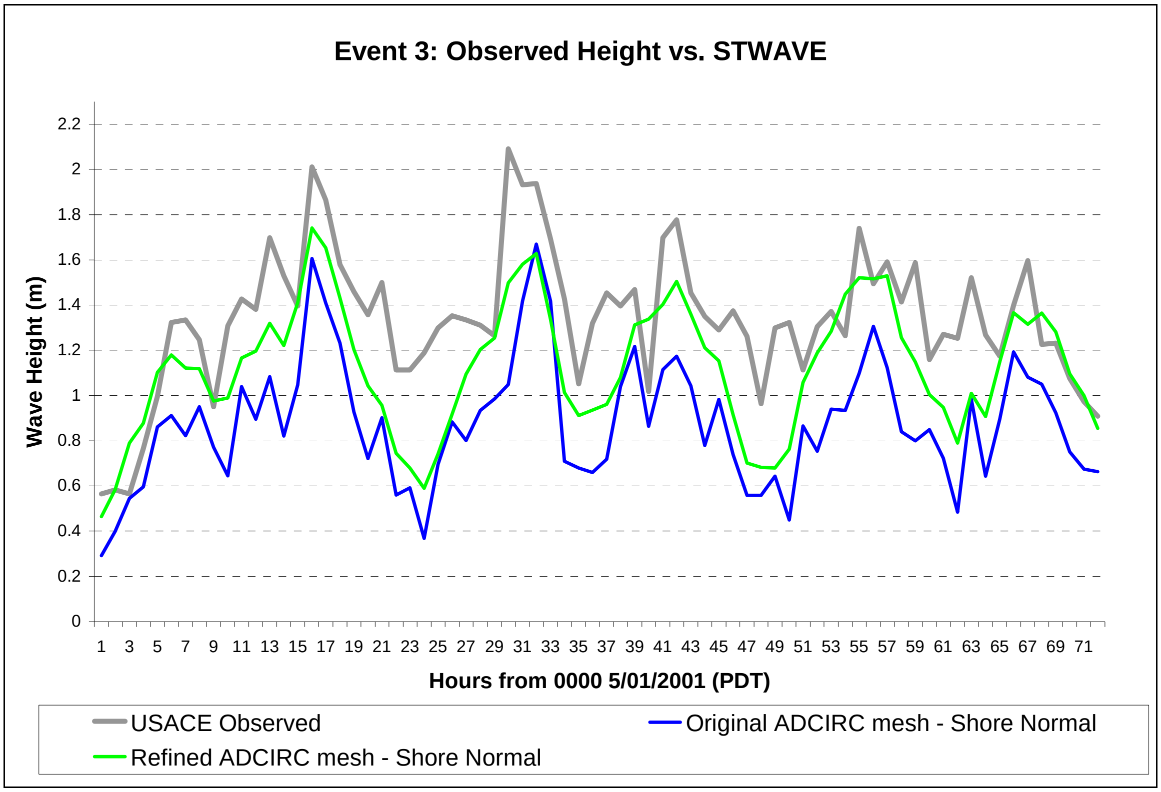

Figure 7.6. Time-series of two-way coupled ADCIRC/STWAVE for two different ADCIRC meshes compared to USACE observed wave heights at humb10 mooring. On average, two-way coupled predictions on the refined mesh had 35% less error than original mesh model predictions.

Clearly adequate mesh resolution is essential for accurate modeling of near-shore currents. In the case of the Humboldt Bay region, reasonable values for currents were obtained with mesh spacing between 35 and 75 m in the surf zone. Further grid refinement could be made to test for improved model output at higher resolutions, but that is beyond the scope of this project. The main focus of this work is on the region immediately around the bay entrance.

8. IMPORTANCE OF WAVE-CURRENT INTERACTION AT THE ENTRANCE TO HUMBOLDT BAY

In this chapter, twenty-four model runs of varying parameters are compared. Current fields, wave height fields, and radiation stress gradient magnitude fields are compared for various coupling modes of the models.

8.1. Model Cases

In order to determine the relative strength of wave-current interactions in the ADCIRC-STWAVE model system, we chose to conduct a series of tests for model sensitivity to environmental conditions and coupling parameterizations. Three representative sets of offshore significant wave heights and dominant periods were chosen to simulate each of the three climatological seasons at Humboldt as described in Chapter 2 (see Table 2.1). For each of these seasons four different choices for predominant offshore wave directions were used, leading to twelve different sets of input spectra. Recall from Chapter 3 that input spectra (boundary conditions) for the STWAVE model are generated within SMS by a parametric function based on equation [3.24] using the peak wave period, wave height, water depth, direction, and the spreading parameters γ and *nn*. For each run the input spectra were held fixed over time. Models were run in uncoupled, one-way coupled, and two-way coupled modes (note that only one uncoupled ADCIRC model case was necessary to establish the current field for all of the uncoupled cases). For one-way coupled runs, the wave fields are not modified by the current fields and are thus identical to wave fields from uncoupled runs.

To examine model conditions over a wide range of current speeds, tidal conditions were chosen based on a three-day period corresponding to a spring tide (January 1 through 3, 2002). These conditions would provide for strong currents during the ebb and flood cycles as well as weak currents at high and low tides.

Model runs are identified by a three-character code according to Table 8.1. The first character, an integer from 1 to 3, identified the choices for significant wave height, dominant period, γ, and nn for the wave input (a larger integer indicates greater significant wave height, dominant period, and overall wave energy). The second character, a capital letter (from A to D see Figure 8.1), defines the offshore wave direction. A third character defines the model-coupling mode (u=uncoupled o = one-way coupled and t = two-way coupled). For example, model run 3Co refers to a one-way coupled model with a 3.1 m significant wave height, a 13.2 second dominant period, and a dominant offshore direction of 308° approximately northwesterly and roughly parallel to the entrance channel. As before, spectral shape parameters were chosen based on the recommendations of Thompson et al. (1996).

Table 8.1. Model run identifiers correspond to the input given. Wave spectra are generated by SMS using values for γ and *nn* based on the work of Thompson et al. (1996).

Input Wave Parameters:	**1**	**2**	**3**
Significant Wave Height (m)	1.8	2.4	3.1
Dominant Period (s)	8.9	11.8	13.2
γ	3.3	4	5
nn	4	8	16

	A	B	C	D
Input Wave Direction	253°	283°	308°	333°
		u	**o**	**t**
ADCIRC-STWAVE Coupling Mode		Uncoupled	One-way coupled	Two-way coupled

We note that direction C corresponds to waves directed roughly parallel to the jetties, while wave from direction A approach the entrance at and angle of about 55° south of the jetty orientation.

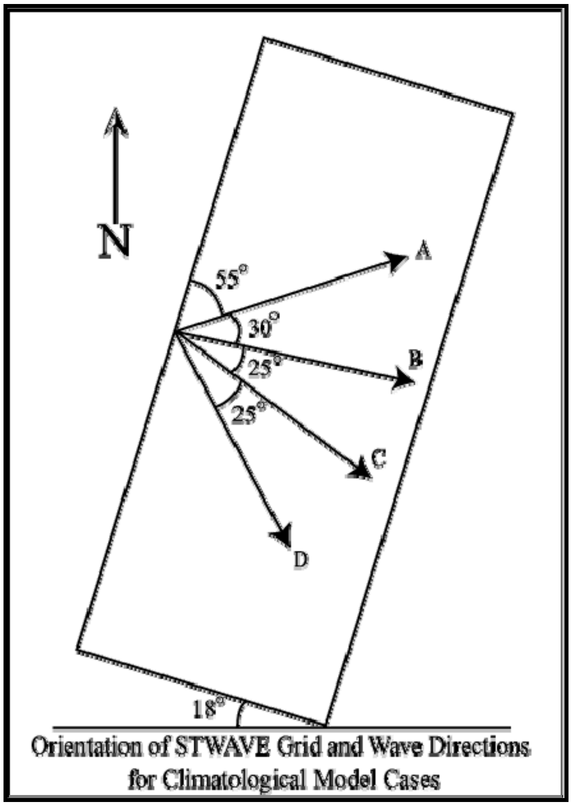

Figure 8.1. Orientation of STWAVE grid and wave directions for climatological model runs. Each arrow represents a modeled wave direction and is labeled with a letter corresponding to the definition described in Table 8.1.

For each model run, forcing in the ADCIRC model was ramped over a two-day time interval according to convention (Zundel *et al.* 2002). Both tidal and wave forcing are scaled from zero to full strength using a hyperbolic tangent function over the first model run day. A second day is allowed to limit any skew in results due to the ramp period. Results for the third day were archived at half-hour intervals for subsequent analysis. The ramping period is necessary for the ADCIRC model as sudden, strong forcing can shock the system, producing instability in the solutions (Zundel *et al.* 2002). A few additional model runs were extended to a fourth day to confirm model behavior. The third and fourth model days showed significant similarity and validated the use of model calculations from the third day.

Model results were compared in five ways. Spatial measures of the tidal currents (vector fields and current magnitudes) and wave field (wave heights and the magnitude of the radiation stress gradients (MRSG)) were evaluated near high (HHW) tide and near maximum ebb and maximum flood current in the entrance channel. Time series of wave heights and currents were examined at three transects within the entrance channel. Because wave-current interaction was observed to be much the same for both highest high tide (HHW) and lowest low tide (LLW), LLW cases are not discussed in this paper. Stages of the tide are defined by averaged data from five entrance channel nodes using the uncoupled ADCIRC model solution. Slack tide (near both high and low tide) was taken at times of minimum average current, while peak ebb and peak flood were taken to be at times of maximum average current at the selected entrance channel nodes.

Because the ADCIRC output was archived at half-hour intervals, estimates of the timing for HHW, maximum ebb, and maximum flood are considered to be +/- 15 minutes. We note however, that both wave-generated currents and the particular choice for coupling could modify the circulation patterns. Thus a “true” definition of HHW and peak current times depends on the particular model run and coupling conditions. Given these issues, it was still considered most useful to compare different model results at the same points in time and to base the choices of those times on the uncoupled ADCIRC model run.

Figure 8.2 displays the bathymetry in the vicinity of the Humboldt Bay entrance. To facilitate subsequent discussion and intercomparison of model results, several key features and regions are identified.

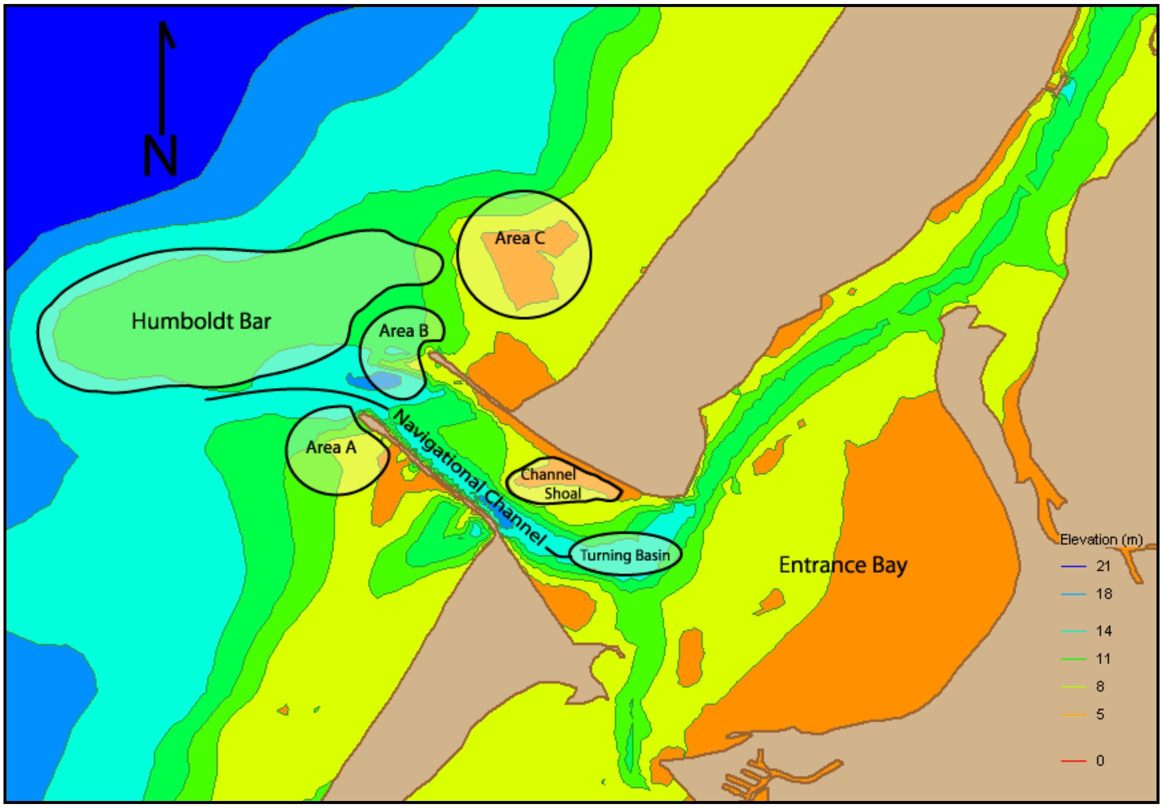

Figure 8.2. Bathymetry and coastline with vicinity of the Humboldt Bay Entrance. Several key features are identified in this plot to facilitate later discussion.

8.2. Comparison Near Slack Tide (HHW)

8.2.1. Model Dependence on Wave Spectra for Direction C (Down-Channel)

8.2.1.1. Current Fields.

Figure 8.3, Figure 8.4, and Figure 8.5 display the magnitude of the current field for model runs 1Cu, 1Co, and 1Ct respectively, near HHW (slack tide). For each of these figures, color indicates current speed. Vectors are included to indicate current direction. For the uncoupled case (Figure 8.3) maximum current in the navigation channel at this time was 0.11 m/s. The overall maximum current speed of 0.46 m/s occurred at the tip of the north jetty. For the one-way and two-way coupled cases, the maximum speeds were significantly higher than the uncoupled case, but comparable to each other. In the navigation channel both the one-way and two-way coupled models produced currents of 0.60 m/s. Over the channel shoal, the one-way coupled model predicted currents of up to 2.2 m/s while the two-way coupled model predicted currents up to 1.8 m/s. Relatively small, short waves produce significant radiation stress gradients only in the most shallow parts of the entrance and along the shore. Stronger currents relate to designated (Figure 8.2) areas A, B, and C along with the channel shoal where radiation stress gradients can be expected to be significant, as will be seen subsequently. Within the critical navigation channel though, all three coupled modes of the model produce relatively small residual currents.

Current patterns differ noticeably between coupling cases. For the uncoupled model, there is little circulation near HHW. At this time, current was ebbing slightly all across the entrance with increased velocities along the jetties. Currents extended offshore in an arc shape to the middle of the Humboldt Bar. No longshore currents were observed in this case since there is no wave induced current. The one-way solution showed a large circulating current pattern formed across the width of the channel, presumably driven by wave radiation stress along the north side of the entrance channel and over the channel shoal. In this case, currents moved away from the jetties, particularly the north jetty, and more into the navigation channel. In contrast to the uncoupled case, current over the channel shoal area was smaller than current in the surrounding area (Figure 8.3). For the one-way coupled model, offshore current did not extend over the Humboldt Bar as in the uncoupled case. Instead, the current field ends just shoreward of the bar. Two-way coupled solutions produced nearly the same current patterns that the one-way solution produced. Again, the strongest velocity tidal currents are found near the navigation channel. Also, currents over the channel shoal was smaller than currents in the surrounding areas (Figure 8.4). For both of the coupled cases, currents along the coastline were directed southwestward. Current fields for both the one-way and two-way coupled solutions exhibit the influence of shallow bathymetry over areas A and C as both coupled cases predict currents of up to 0.34 m/s.

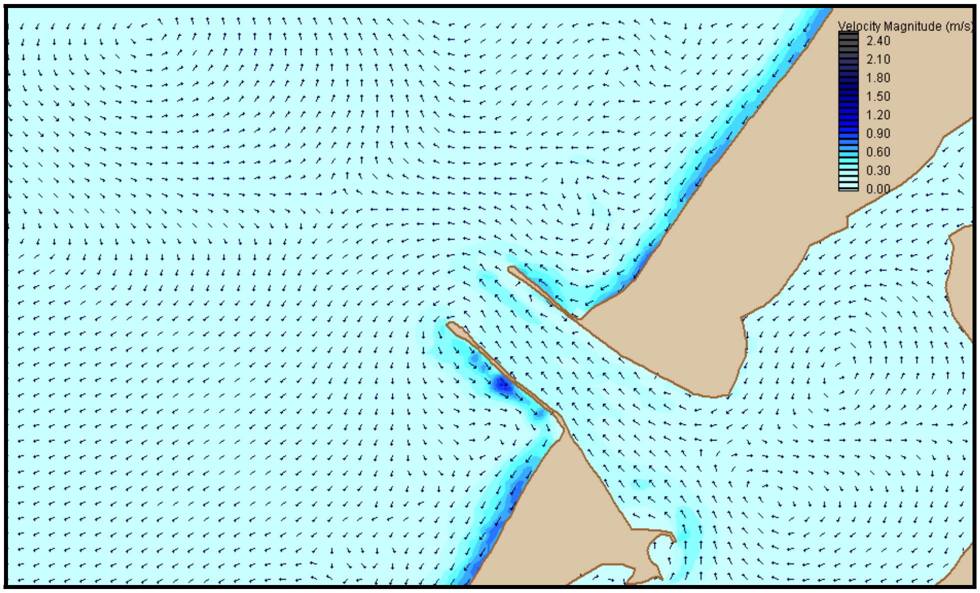

Figure 8.3. Current magnitude near HHW for model run 1Co. One-way coupled currents were slightly higher along the jetties, over the channel shoal, and along the shore than two-way coupled currents.

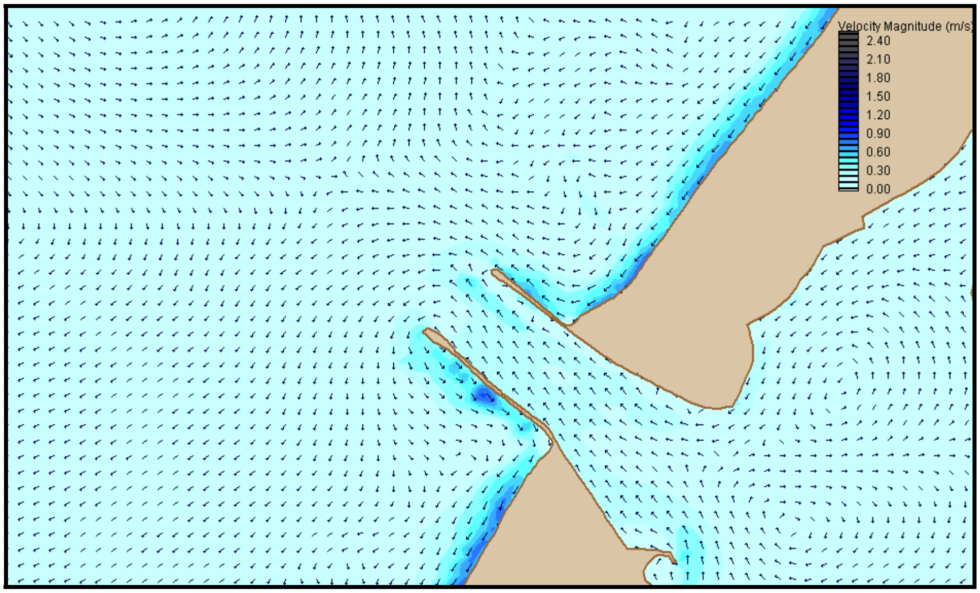

Figure 8.4. Current magnitudes near HHW for model run 1Ct. Speeds are generally less than those predicted by the one-way coupled model solution, but show similar patterns over the channel shoal, along the north jetty, and in area A.

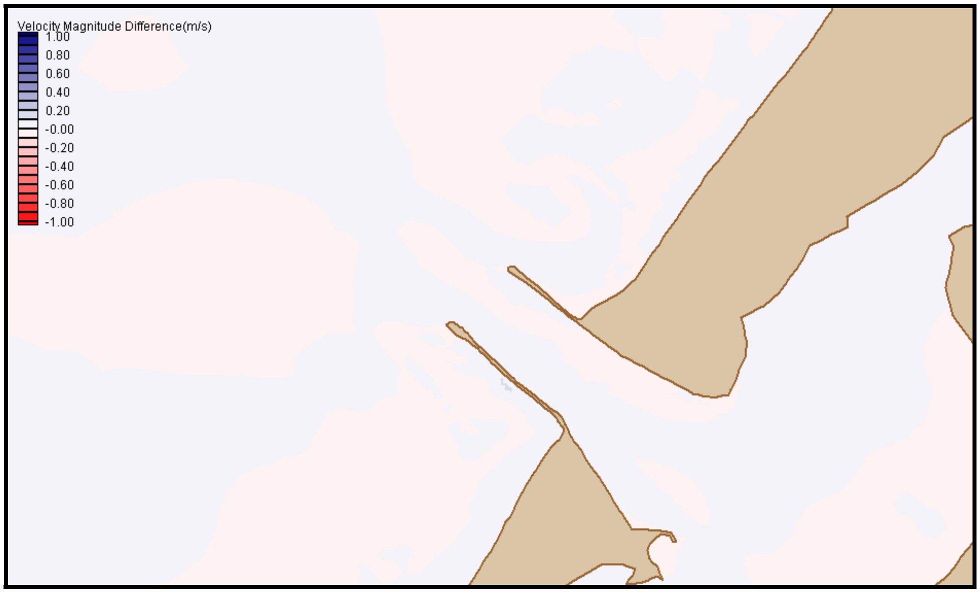

Figure 8.5. Difference magnitude of current velocities for model runs 1Co and 1Ct. Two-way output was subtracted from one-way output. Small differences in the shape of the current fields are responsible for the visible difference between cases.

Figure 8.5 shows the current difference field between one-way and two-way coupled cases (i.e., the difference between Figure 8.3 and Figure 8.4). Differences are generally less than +/- 0.10 m/s over the navigation channel. The most significant differences lie along the jetties where the one-way coupled solution predicts current speeds 0.15 m/s higher than the two-way coupled solution. Small differences in these figures suggest that there should be little net influence of the currents on the wave field under these conditions.

As wave energy and wavelengths increase, differences between model coupling modes also grow. For the 3Co case (Figure 8.6), characteristic circulation pattern in the entrance channel observed in case 1Co remains, but is extended in size. In the 1Co case, it lies between area B and the channel shoal, while in the 3Co case it extends from the jetty tips to the turning basin in the entrance bay. Currents along the north jetty average 2.06 m/s, flooding, while the navigation channel current speed averages 0.43 m/s ebbing (recall again that these conditions pertain to near HHW). Immediately offshore of the entrance, currents are dominated by strong circulation cells around areas A and C (Figure 8.2). Significant currents also occur over the Humboldt Bar area in the 3Co case. Differences between the uncoupled case and the one-way coupled model case are also more pronounced with these larger waves.

For the two-way coupled solution (Figure 8.7), currents near the entrance are dominated by similar circulation cells as seen in the one-way coupled solution. Instead of only one circulating current field as in the case of the one-way coupled model, two distinct circulating fields are seen in the entrance channel. The first is a small nearly circular eddy centered between area B and the channel shoal. The second is oblong lying east of the channel shoal and encompassing the Turning Basin. Currents along the north jetty are flooding and average 1.47 m/s, while currents in the navigation channel are ebbing and average 0.31 m/s. Figure 8.8 shows the velocity magnitude difference between 3Cu and 3Co (note that 3Cu and 1Cu provide identical circulation patterns). Differences between uncoupled and one-way coupled current magnitudes are evident in every area but the portion of the navigation channel that lies between the jetties.

Figure 8.9 displays the difference between model runs 3Co and 3Ct. Currents predicted in the 3Co case are 0.59 m/s higher along the north jetty than those predicted by the 3Ct case on average. In area C, the difference between coupling modes reaches 2.04 m/s. In both the 3Co and the 3Ct cases, longshore currents are generated, since the offshore wave angle is about 17° north of shore-normal. The one-way coupled case predicted currents on the order of 0.5 m/s faster than the two-way coupled case over the near-shore area around the entrance. Within the entrance, in the navigation channel and Turning Basin areas, the differences were less significant, averaging 0.22 m/s.

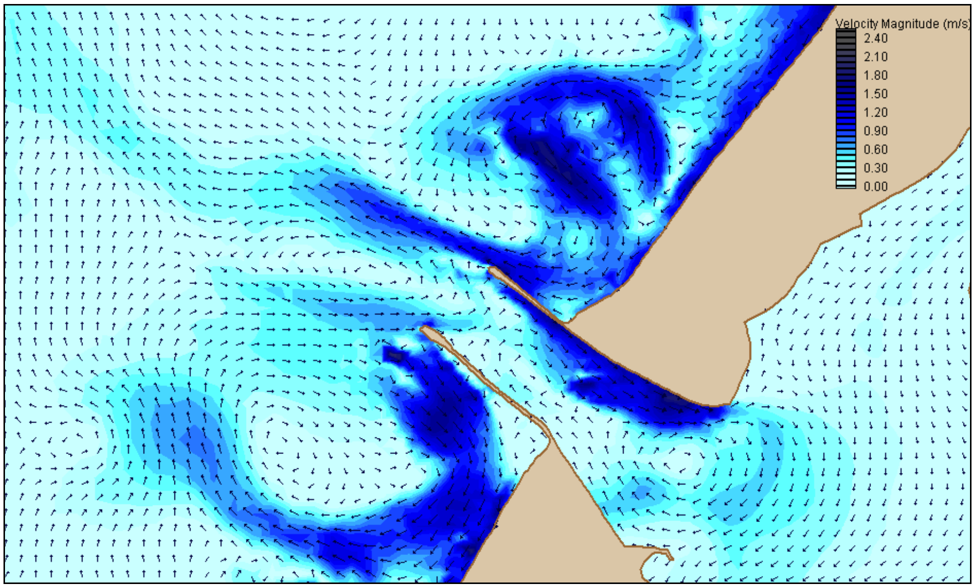

Figure 8.6. Current field near HHW for model run 3Co. Note the strong offshore current immediately north of the north jetty. This is characteristic of the one-way solution and does not appear in the other model coupling cases.

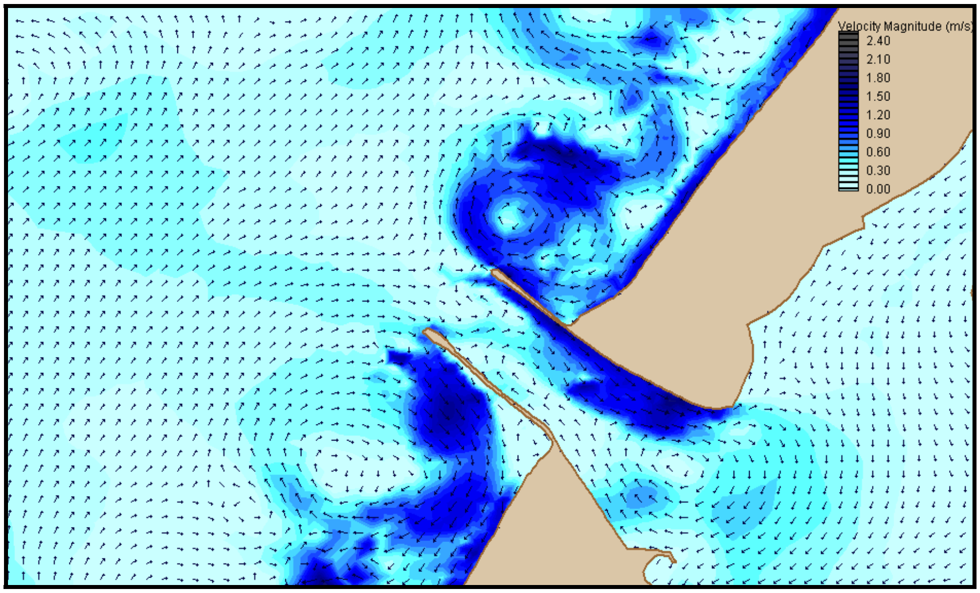

Figure 8.7. Current field at near HHW for model run 3Ct. Two circulating currents formed in the entrance channel in this case.

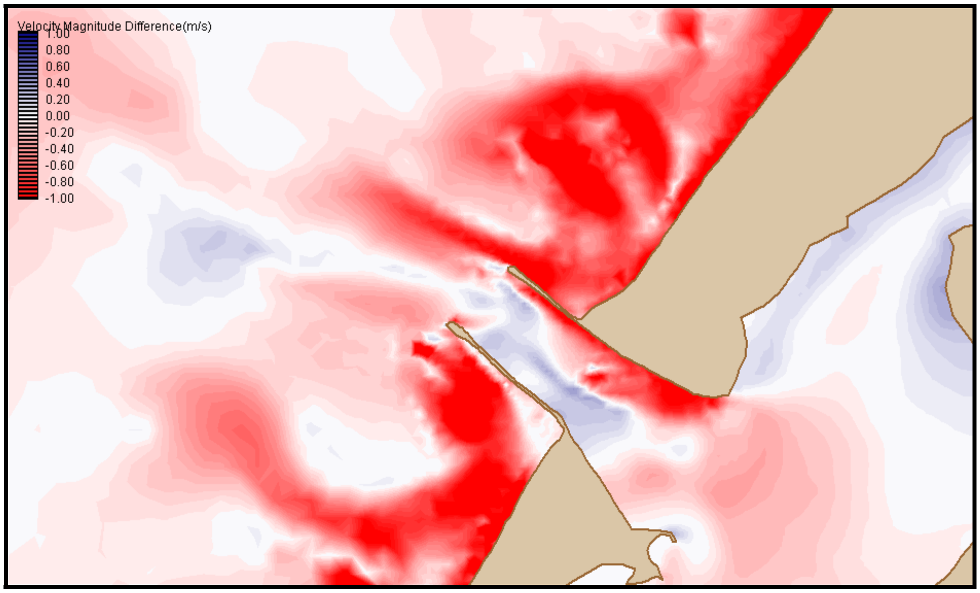

Figure 8.8. Difference in velocity magnitudes between 3Cu and 3Co model cases. Coupling moves much of the current from the middle of the channel to the inside edge of the north jetty. Vectors represent current velocities for the 3Co model case.

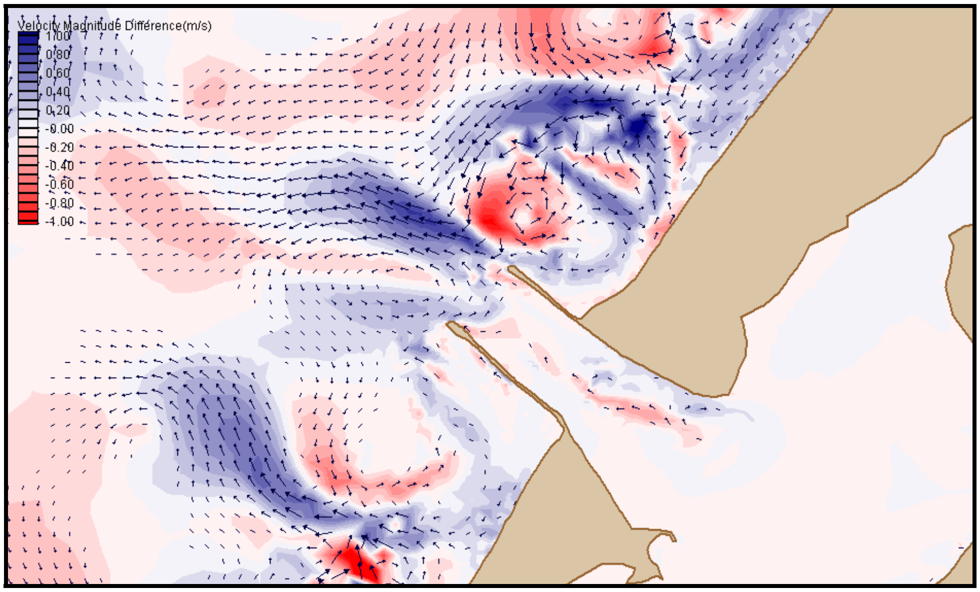

Figure 8.9. Difference in velocity magnitudes between model runs 3Co and 3Ct near HHW. Two-way model solution was subtracted from one-way model solution. Vectors shown are the difference vectors between cases.

8.2.1.2. <u>Wave Height Fields.</u>

In this section, we examine model predictions of significant wave height near HHW. Note that the STWAVE model was updated and archived once every hour of model time, so synchronization to tidal stage is accurate to within one half hour. Also uncoupled and one-way coupled model runs produced identical wave fields because neither approach allows the circulation to modify the wave field. Consequently we present only comparisons of one-way and two-way coupled model solutions. Wave height figures, processed using Matlab software, are presented with a 162° clockwise rotation of the STWAVE grid.

Figure 8.10 shows a comparison of the wave height fields for model runs 1Co and 1Ct. In both cases, wave heights peak near the area C. For the one-way solution, the maximum height was 2.29 m, while for the two-way solution the peak height was 2.27 m. The one-way coupled case showed greater increase in wave height over area A (0.11 m spatially averaged) and the channel shoal (0.26 m spatially averaged). The two-way coupled case showed shoaling offshore of area C and in area A. Note that spreading of wave energy in the entrance bay is much greater in the two-way coupled case. Differences in wave height for the entrance area remained less than 0.20 m for the two cases.

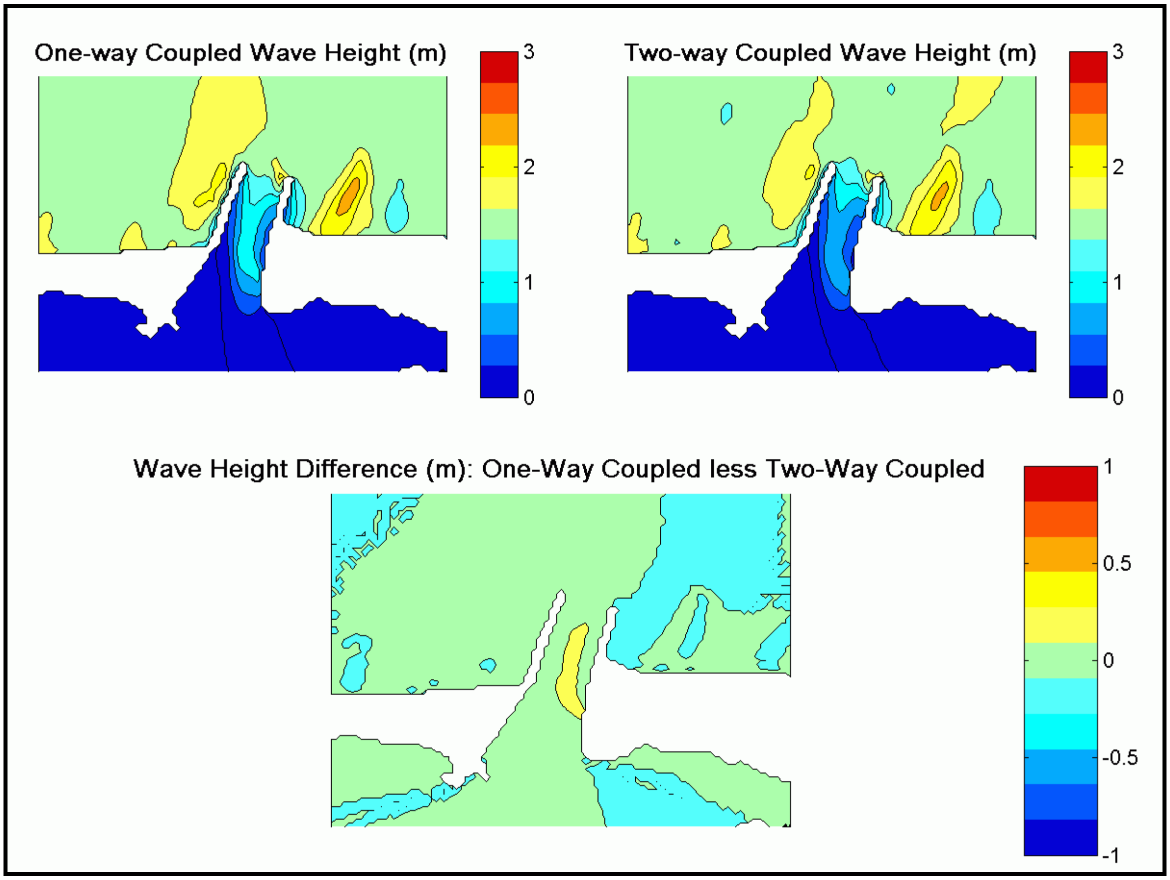

Figure 8.10. Comparison of wave height fields for model runs 1Co and 1Ct.

Figure 8.11 shows a comparison of model runs 3Co and 3Ct near HHW. For current conditions, refer to Figure 8.6 and Figure 8.7. One-way coupled waves are up to 0.25 m higher than the two-way coupled waves south of the tip of the south jetty and lower in the entrance channel by up to 1.13 m. Another significant difference between coupling cases is in area C, north of the entrance. In the 3Co case (Figure 8.6), a strong offshore current is shown immediately north of the north jetty. In the 3Ct case, the offshore current at the same place is weaker, but the waves show increased steepness and are 2.89 m higher in the 3Ct case than in the 3Co case. As in the 1Co and 1Ct wave height fields, the 3Ct case shows higher waves (0.43 m higher, on average) than the 3Co case throughout the Entrance Bay. In the navigation channel, near the channel shoal, the 3Ct case predicted larger wave heights than the 3Co case, 0.83 m on average, over an area 180 m wide and 530 m long.

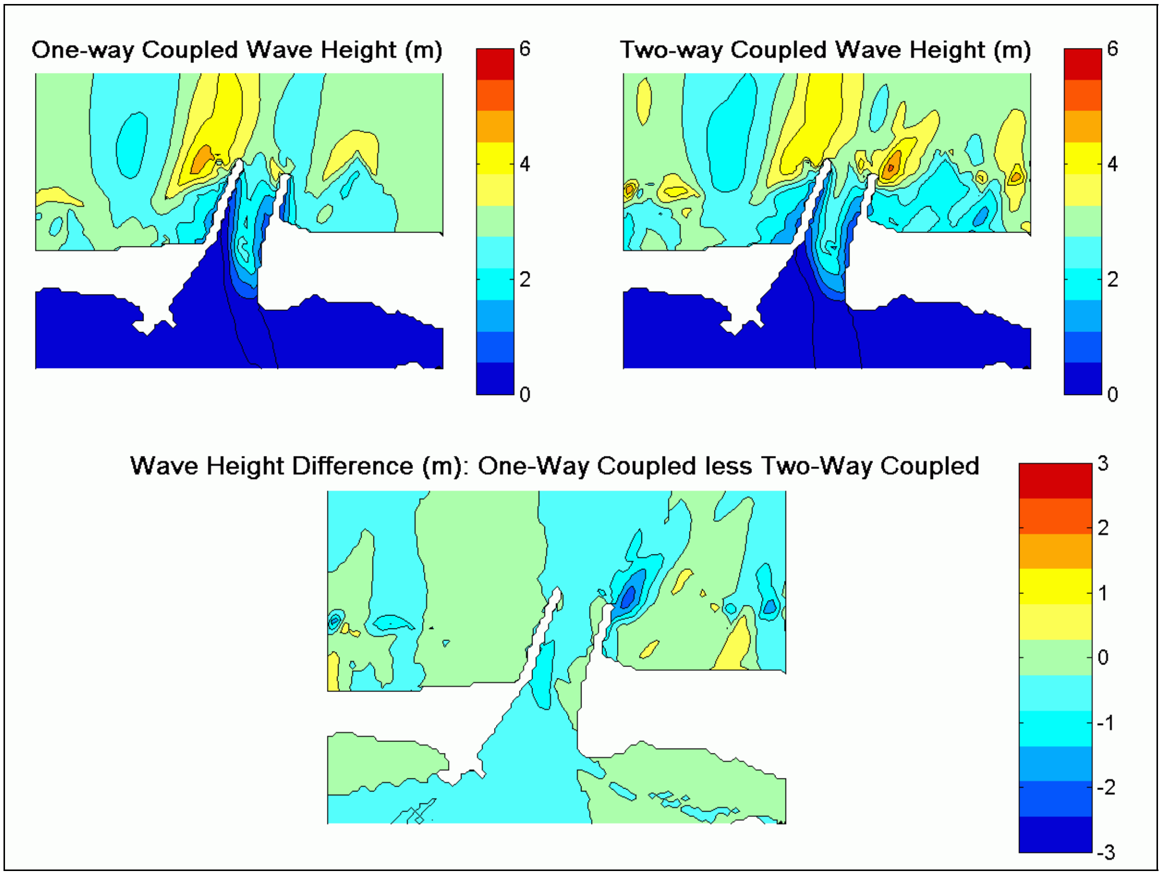

Figure 8.11. Comparison of wave height fields for model runs 3Co and 3Ct. Two-way coupled solutions average 0.43 m higher than one-way solutions over most of the entrance area.

To better quantify the comparison in the entrance, the spatial root-mean-square (rms) wave height differences between coupling cases for the entrance from the seaward edge of area B to the shoreward side of the turning basin were calculated. For the 1Co and 1Ct runs this values was 0.15 m, for the 2Co and 2Ct model runs the values was 0.51 m, and for the 3Co and 3Ct runs the value was 0.67 m.

8.2.1.3. Radiation Stress Gradient Fields.

In this section we examine model predictions of radiation stress gradients near HHW. Recall that uncoupled and one-way coupled radiation stress gradients are identical. Comparisons will feature only one-way and two-way coupled model solutions. Radiation stress gradient solutions were archived at the same time in the model as the wave height solutions, so that synchronization to tidal stages is accurate to one half hour. Note that a radiation stress gradient has the same units as a pressure gradient (kg/ms^2). Figures again show the STWAVE grid with a 162° clockwise rotation.

In every modeled case, the magnitude of the radiation stress gradient (MRSG) peaks over the grid cells closest to the shoreline. These peaks in MRSG result in predicted longshore currents of varying magnitude and direction depending on input wave conditions. Predicted longshore currents tended to be in excess of 4.3 m/s for the largest wave cases studied here. Such values are considered unrealistically high, but the focus of this study is on the vicinity of the entrance channel. Limited testing with the validation cases indicated that greater resolution for both model grids could yield more realistic results along the shore, but at the cost of substantially longer model run times.

Figure 8.12 shows a comparison of the MRSG for model runs 1Co and 1Ct near HHW. MRSG fields show much the same pattern for the two coupling modes. In this case, the two-way coupled model predicts larger MRSGs in the entrance channel, while the one-way coupled model produces larger values at the tip of the north jetty. Typically, the largest MRSG values, other than along the shoreline, occur over shoaling areas.

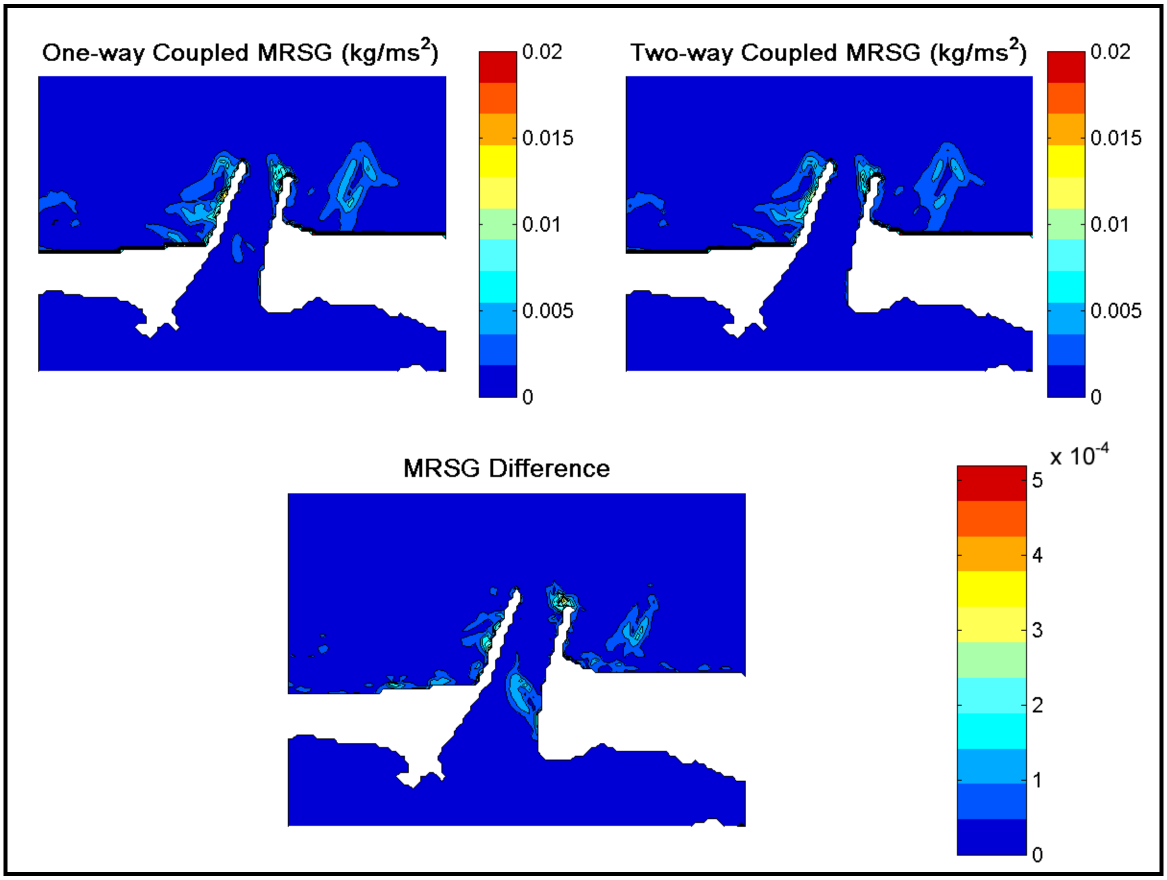

Figure 8.12. Comparison of the magnitude of radiation stress gradient fields (MRSG) generated by model runs 1Co (upper left panel) and 1Ct (upper right panel) near HHW. The lower panel represents the magnitude of the vector difference between the two radiation stress gradient fields.

Figure 8.13 shows a comparison of the MRSG fields for model runs 3Co and 3Ct. MRSG fields correspond well with wave height fields. In the 3Co case, the radiation stresses are strong in area A, corresponding to the large wave heights in the same area shown in

Figure 8.11. Other areas of shoaling in the wave height field show significant radiation stress gradient magnitudes also. The significance of the difference in radiation stress gradient magnitudes can be inferred from the difference in current fields for these cases. Note that the offshore jet just north of the north jetty appearing in Figure 8.6 is not present in Figure 8.7. Significant radiation stress gradients are predicted in that area by the two-way coupled model run, but not by the one-way coupled model run. Radiation stress gradients then, act to retard the offshore current in the two-way coupled case yielding the current fields as presented above. Careful comparison of Figure 8.9 and Figure 8.13 showed that raised current magnitudes correspond to greater radiation stress gradient magnitudes in every observed case near HHW.

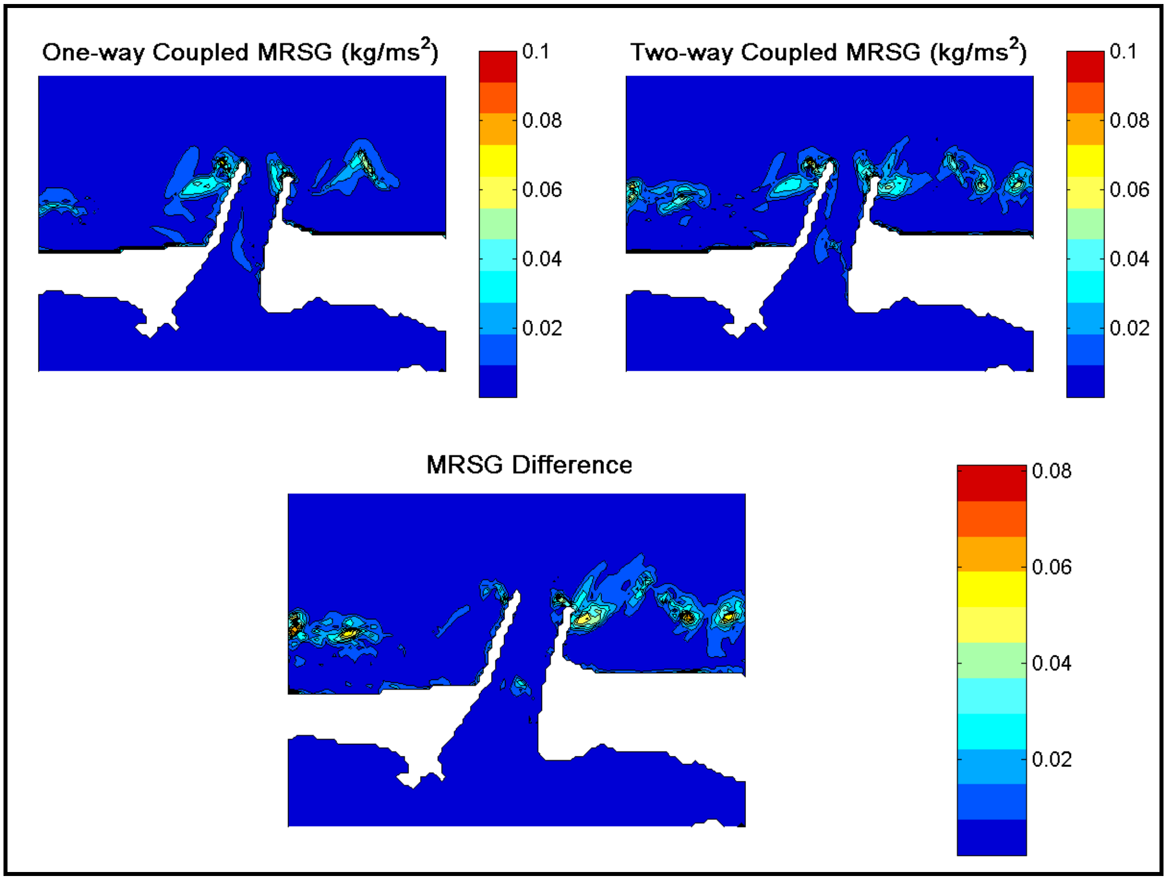

Figure 8.13. Comparison of MRSG fields for model runs 3Co and 3Ct near HHW. The difference plot is a magnitude difference and thus only quantifies dissimilarity at a given point.

Note that the 3Co and 3Ct model runs produced MRSGs four times as large as the 1Co and 1Ct runs over shoaling areas.

8.2.2. Model Dependence on Wave Spectra, Direction A (Oblique to the Entrance)

8.2.2.1. Current Fields.

Current fields for direction A cases were compared in the same way as cases for direction C near HHW. In general current fields for the same input wave height and coupling case differed significantly for different choices of input wave direction. It should also be noted that the 1Au and the 3Au cases yield identical results to the 1Cu and 3Cu cases, respectively. Compared to the uncoupled 1Au case, the velocity field predicted by the 1Ao model run shows differences in current rate and direction over nearly the whole entrance channel. Recall in the uncoupled model case, there was a slight ebbing current over the whole width of the entrance with peak currents in area B. For the 1Ao model case, current in the navigation channel is ebbing, but along the north side of the entrance and over the channel shoal, there is a flooding current, driven by radiation stresses.

For the 1Ao and the 1At cases, there were two characteristic current patterns near HHW. Over area A (see Figure 8.2), a counter-clockwise circulation cell was predicted. For the 1Ao case the diameter of the circulation cell is predicted to be 710 m, 160 m larger than in the 1At case. The second characteristic of both model current fields was a counter-clockwise circulation pattern within the entrance of the bay. In the navigation channel, there was slight ebbing current, less than 0.10 m/s. On the north side of the channel and over the channel shoal region, there was a flooding current of up to 0.7 m/s in the 1Ao case and 0.6 m/s in the 1At case.

Figure 8.14 shows the current field for the 1Ao model case. The circulation patterns discussed above are apparent in the figure. Another interesting aspect of the current field is the decrease in current velocity between the jetty tips. Here, the slightly ebbing current is retarded by wave energy. Note that the current is not retarded along the inside of the south jetty which is largely sheltered from waves.

Figure 8.15 shows the current field for the 1At model case. In this case, the currents show similar patterns as for the one-way coupled model. Primary differences are in the magnitude of the currents. In the navigation channel and in most of the entrance, differences in predicted current rates between these two model cases were minimal, always less than 0.14 m/s. In the plot of current magnitude difference (Figure 8.16), the disparity in circulation cell size is highlighted by 0.50 to 0.70 m/s differences in current velocity. Over the rest of the entrance area, little difference in current velocity can be seen.

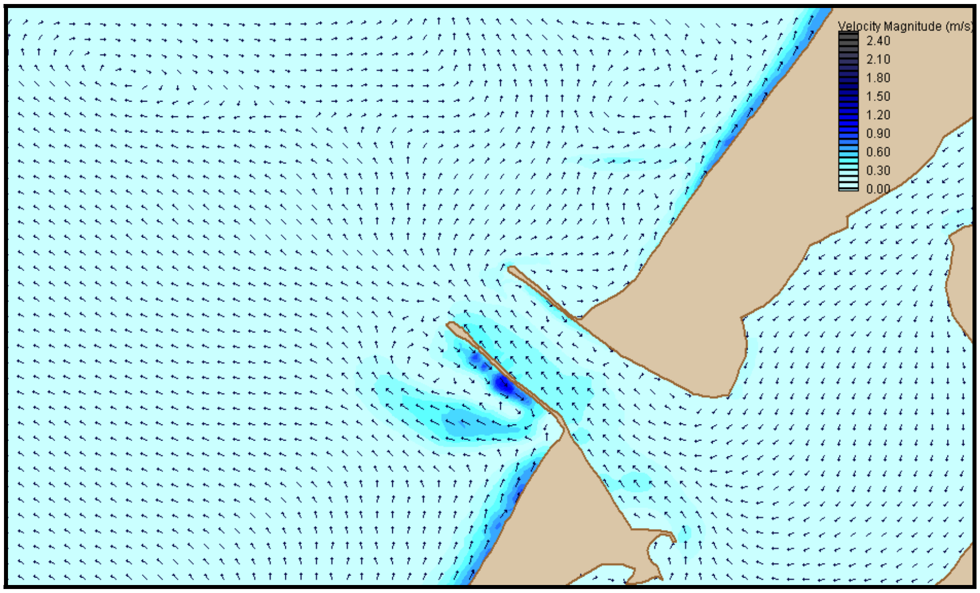

Figure 8.14. Current magnitude near HHW for model run 1Ao. Modeled ebbing current in navigation channel can be seen as the model data point occurs shortly after HHW. However, peak currents at the tip of the north jetty and over the channel shoal are directed into the bay.

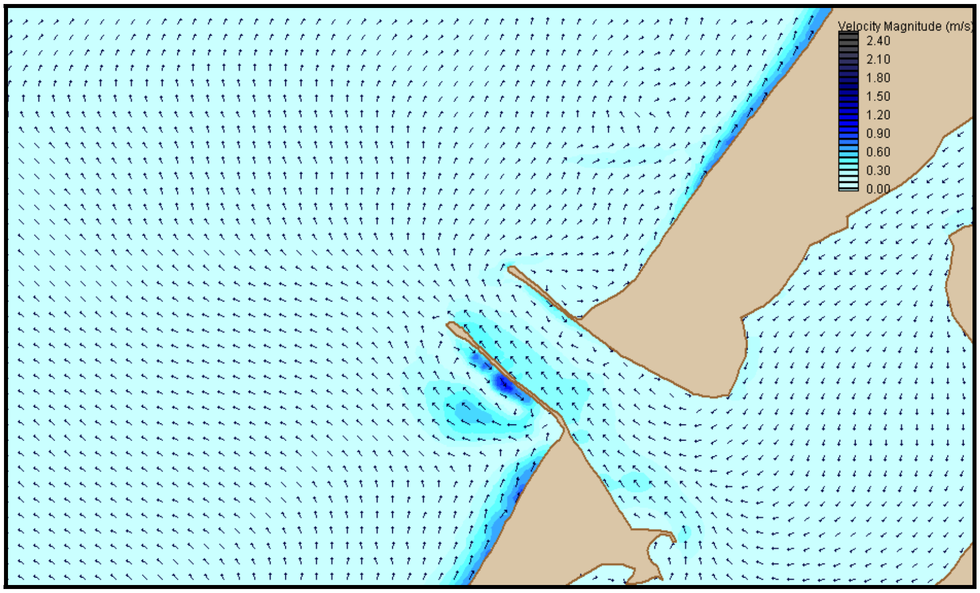

Figure 8.15. Current magnitude near HHW for model run 1At. Modeled ebbing current in navigation channel can be seen as the model data point occurs shortly after HHW. However, peak currents at the tip of the north jetty and over the channel shoal are directed into the bay.

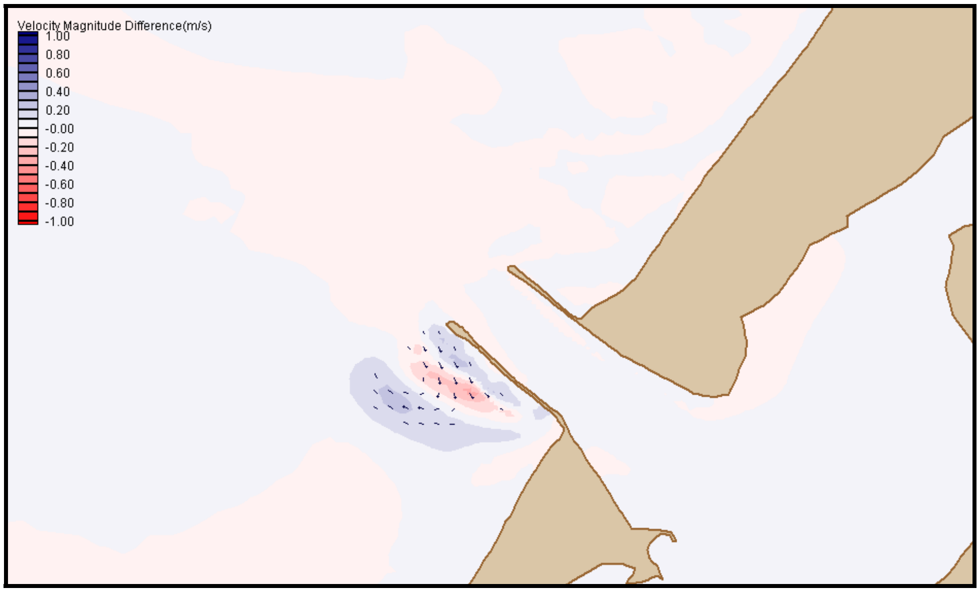

Figure 8.16. Plot of current magnitude difference between cases 1Ao and 1At near HHW. The main region of difference between model runs was shoreward of area A and related to the diameter of the circulation cell predicted there by both models. Vectors represent the vector difference in currents between each case.

For model cases 3Au, 3Ao, and 3At, differences in current magnitude and direction occurred in much the same locations as in the 1Au, 1Ao, and 1At cases. The two characteristic circulation patterns observed in the lower energy wave case occurred in the 3Ao and 3At cases, although there was some distortion in each case. For instance in both the 3Ao case and the 3At case, the counter-clockwise current near area A increased in size to 880 m and 700 m respectively. In the 3At case, the circulation was distorted, with the greatest current magnitudes occurring in an elongated oval, parallel to the south jetty (Figure 8.18). For the 3Ao case, the circulation pattern is much more regular and rounded (Figure 8.17). In each instance there is an ebbing current along the south jetty and a flooding current along the north jetty. Figure 8.19 shows the difference in current magnitudes between cases. In the two-way coupled model, greater current magnitude is seen over the channel shoal.

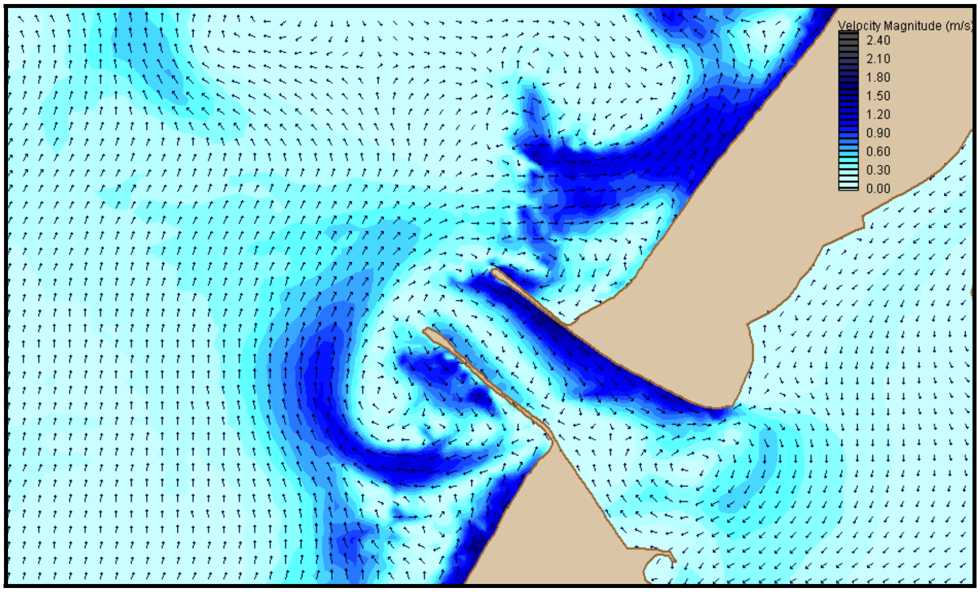

Figure 8.17. Current magnitude near HHW for model run 3Ao. Modeled ebbing current in navigation channel can be seen as the model data point occurs shortly after HHW. However, peak currents along the north jetty are directed into the bay.

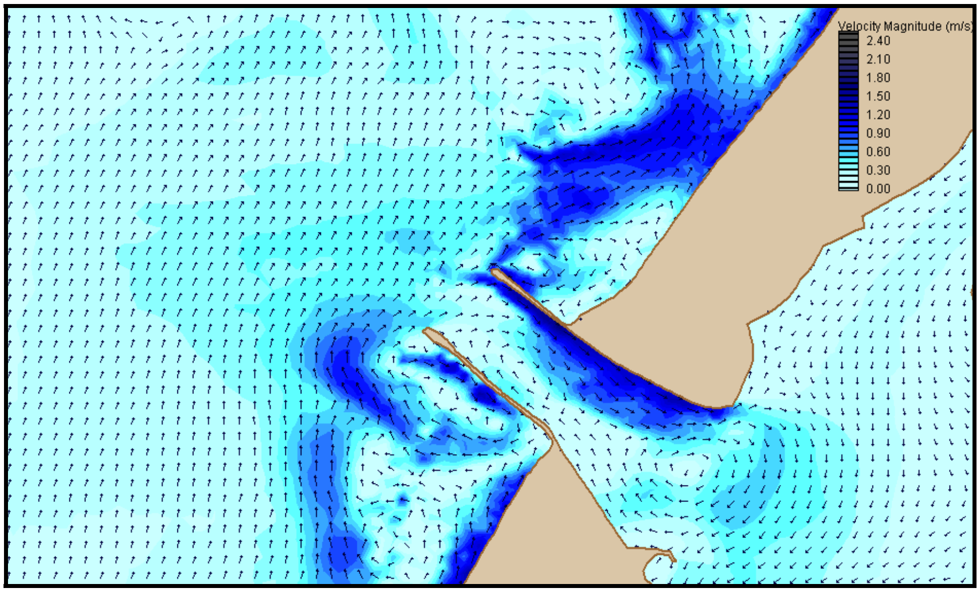

Figure 8.18. Current magnitude near HHW for model run 3At. Modeled ebbing current in navigation channel can be seen as the model data point occurs shortly after HHW. However, peak currents along the north jetty are directed into the bay.

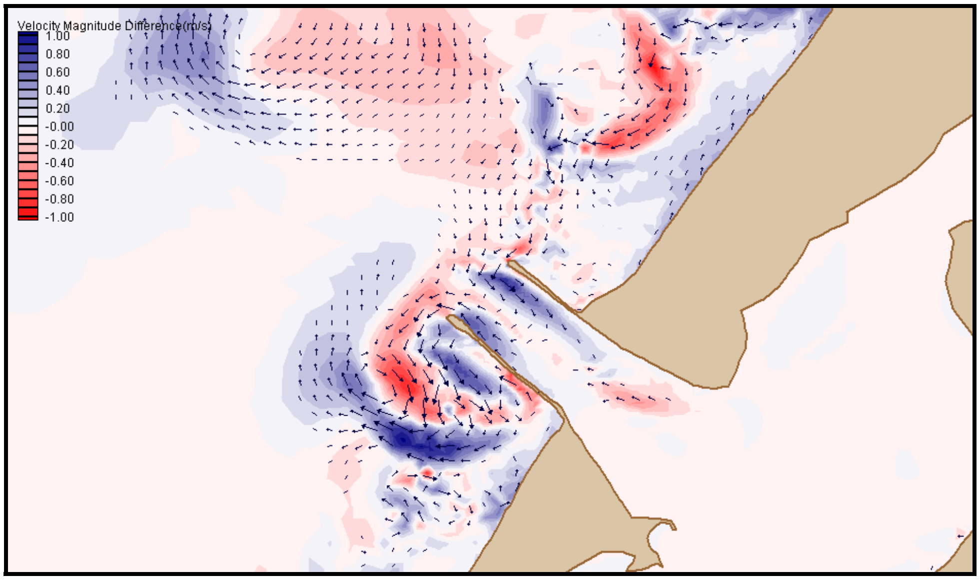

Figure 8.19. Plot of current magnitude difference between cases 3Ao and 3At near HHW. Offshore the models predict different current patterns and rates in areas A and C. In the entrance, the 3Ao model predicts higher current rates near the jetty tips (flooding at the north and ebbing at the south). Over the channel shoal, the 3At model predicts higher current speeds.

8.2.2.2. Wave Height Fields.

For the 1Ao, 1At, 3Ao and 3At cases, model coupling affects results in much the same way as it did for the 1Co, 1Ct, 3Co, and 3Ct cases. For the largest wave conditions, two-way coupled wave heights averaged 0.42 m higher than one-way coupled wave heights in the entrance channel. For wave parameters 1 and 2 (see Table 8.1), the two-way coupled solution predicted mean wave heights 0.27 and 0.11 m respectively above the one-way coupled solution. Figure 8.20 shows the wave height comparison between model cases 1Ao and 1At near HHW.

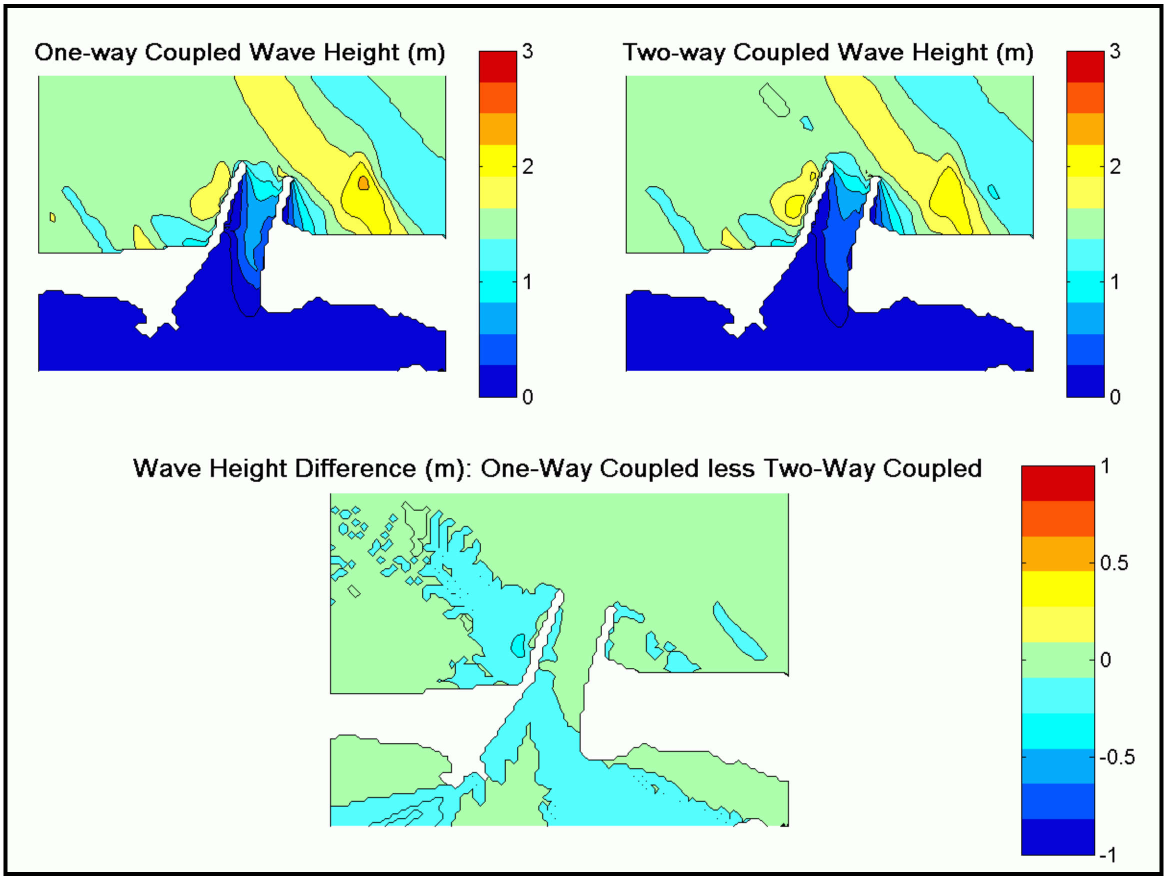

Figure 8.20. Comparison of wave height fields for model runs 1Ao and 1At near HHW. Note the waves in the two-way coupled model are up to 0.5 m higher in the Entrance Bay than in the one-way coupled model.

Figure 8.21 shows the model predicted wave heights for cases 3Ao and 3At near HHW. The difference between coupling cases is especially obvious in this case. Note that in the 3At case, wave heights in the navigation channel and entrance bay are up to 1.18 m higher than in the 3Ao case, consistent with observed differences between the 1Ao and 1At cases.

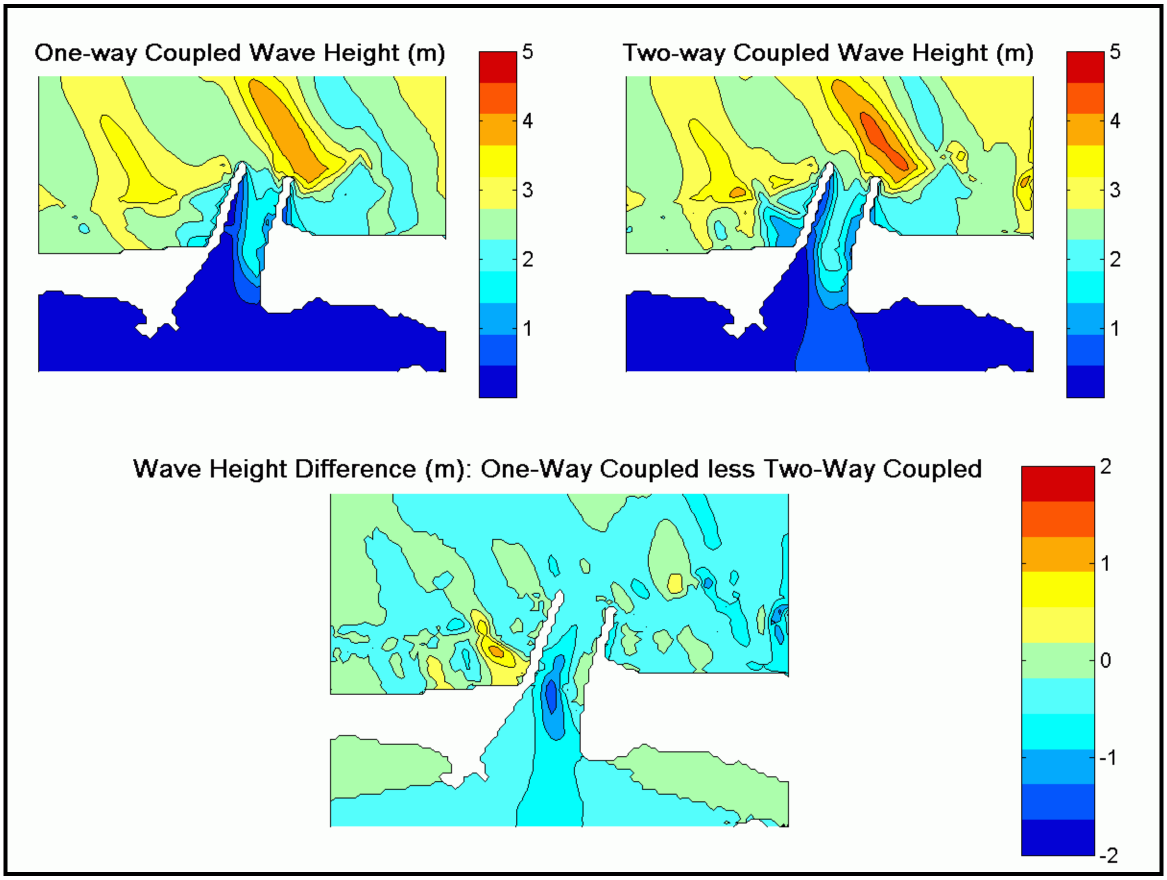

Figure 8.21. Comparison of wave height fields for model runs 3Ao and 3At. Two-way coupled solutions average 0.53 m higher than one-way solutions over most of the entrance area.

8.2.2.3. Radiation Stress Gradient Fields.

Differences in radiation stress gradient fields between coupling cases were minimal (less than 10% of predicted values) between the 3Ao and 3At cases and between 1Ao and 1At cases. In the channel and entrance bay, there was nearly no difference between coupling cases even for the largest waves. Figure 8.22 shows that only slight differences, typically 3 x 10^{-4} kg/ms^2, between radiation stress gradient magnitudes occur at the tip of the north jetty and along the outside edge of the south jetty. Higher waves predicted by the 1At model run throughout the entrance channel do not correspond to significantly larger radiation stress gradients.

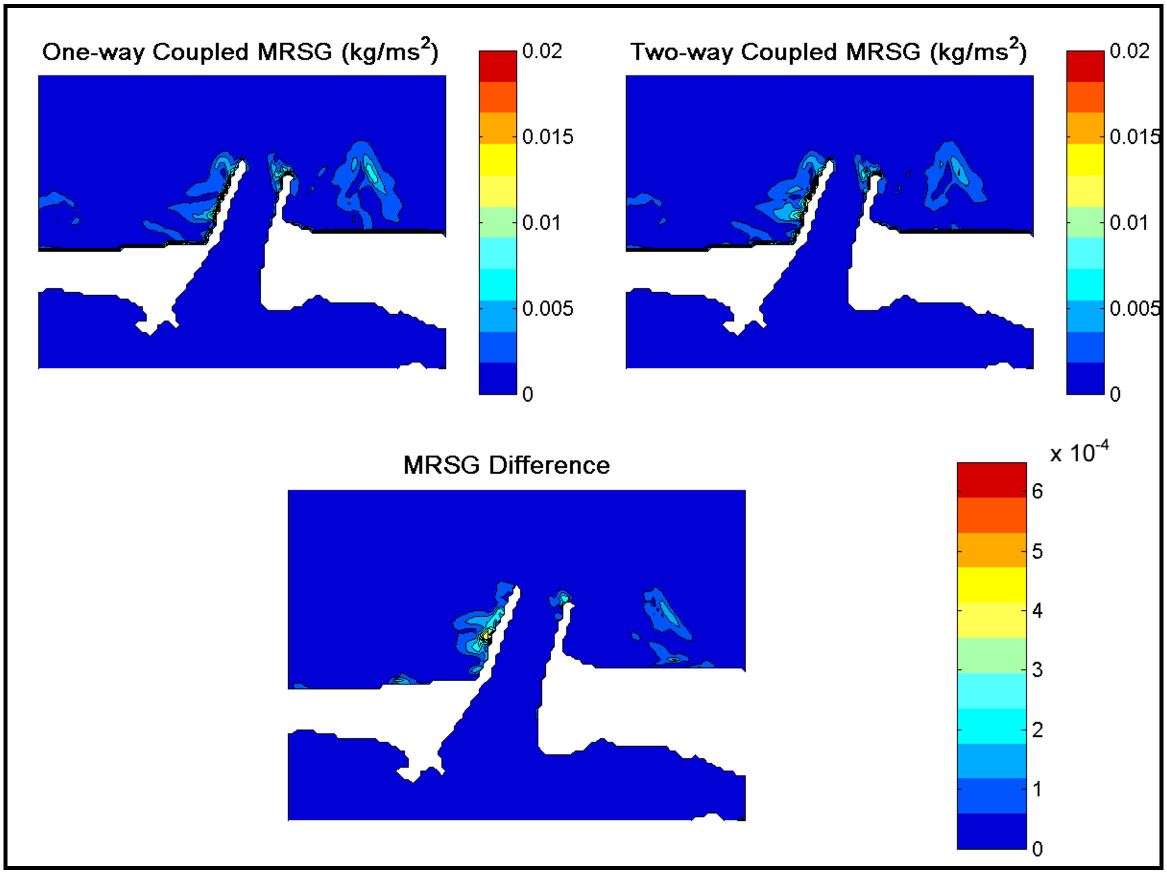

Figure 8.22. Comparison of the magnitude of radiation stress gradient fields generated by model runs 1Ao (upper left panel) and 1At (upper right panel) near HHW. The lower panel represents the magnitude of the vector difference between the two radiation stress gradient fields.

Figure 8.23 shows the radiation stress gradient magnitudes near HHW for model runs 3Ao and 3At. With the larger waves, the magnitude of the difference in radiation stress gradients was larger, but differences were concentrated at the channel shoal or to the north or south of the actual entrance.

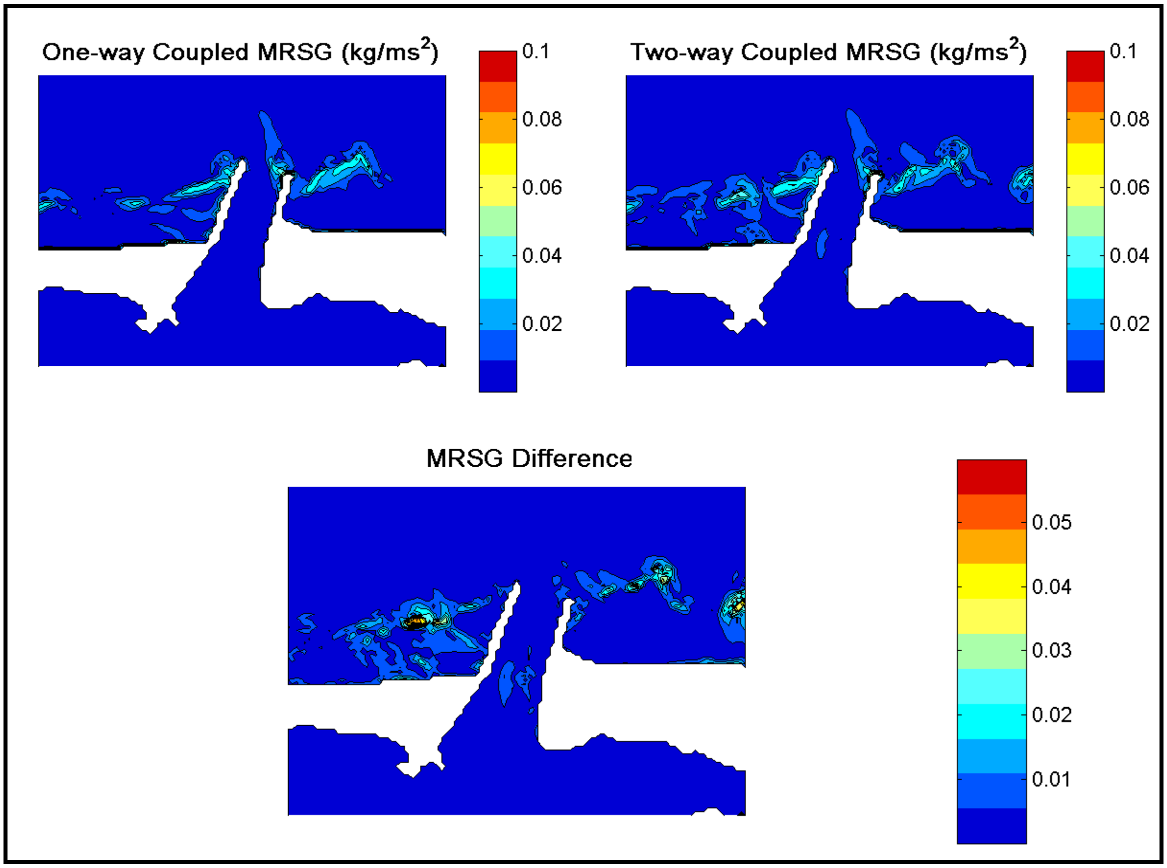

Figure 8.23. Comparison of MRSG fields for model runs 3Ao and 3At near HHW. The difference plot is a magnitude of the vector difference and thus only quantifies dissimilarity at a given point.

8.2.3. Model Dependence on Dominant Direction of Input Wave Spectra Near HHW

Clearly, wave energy input is significant to the behavior of model solutions. Since wave energy has both a magnitude and direction, it is important to quantify the effect on model solutions of differences in input wave direction. Consideration of the effect of model coupling on waves from different directions near slack tide should reveal the smallest possible differences between those coupling cases.

8.2.3.1. Direction Characteristics for Small Waves.

Although four different wave directions were modeled, to reduce complexity, three wave directions are compared for the smallest wave conditions (1A*, 1B*, and 1C*). For a visual comparison of actual wave direction, refer to Figure 8.1.

Two-way coupled solutions show more wave energy in the entrance channel than one-way solutions for input waves in the A and B directions. As can be seen from Figure 8.21, the two-way coupled model in the 1At case predicts wave heights up to 20% higher than the one-way coupled solution over the dredged portion of the channel and into the entrance bay. Other directions yielded similar results. For the 1Bo and 1Bt cases, mean height difference in the entrance channel was 0.18 m with a maximum difference of 0.32 m. Radiation stress gradient differences were nearly unnoticeable and predicted currents were again within 0.05 m/s between coupling cases. For the 1Co and 1Ct model cases, the one-way coupled model predicted larger waves than the two-way coupled model in the entrance channel and into the bay (Figure 8.10).

Differences in current speeds and radiation stress gradient magnitudes are not reflected in differences in wave height fields. For the small waves, there was less than a 5% difference in the current fields and insignificant differences in the radiation stress gradient magnitude fields.

8.2.3.2. Direction Characteristics for Larger, Longer Waves.

Comparisons of model output for different input wave directions were made for the large wave conditions in the same way as for the small wave conditions. With the larger, longer waves, direction of input becomes much more significant at HHW. Two-way model coupling appears to reduce the shadowing effect of the jetties observed in the one-way coupling cases, bending significant wave energy into the entrance.

For wave spectra generated with dominant direction C, there is a significant difference between one-way coupled and two-way coupled model output. For the one-way coupled case, as seen from the wave height fields, a majority of the wave energy is focused and broken on the shoal about 2/3 of the way down the entrance channel, producing waves in the entrance bay of 0.6 m and less (Figure 8.32 Figure 8.33). For the two-way coupled case, even at slack tide, the wave energy is dispersed more completely across the channel and into the entrance bay, producing wave heights in the entrance bay 0.4 to 0.8 m higher than the one-way case (

Figure 8.11). Directional spreading is also more significant in the two-way coupled case, with more wave energy directed towards the North Bay and South Bay than the one-way coupled case. Current fields between cases are also different as seen in Figure 8.8.

For wave spectra generated with dominant direction B, the difference between one-way and two-way coupled solutions for wave height and current velocity is less significant than that for the direction C cases. Although both versions of the model predicted lower overall wave heights in the entrance bay, wave height differences between one-way and two-way coupled solutions remained between 0.4 and 0.8 m in the entrance bay, with the two-way coupled solution consistently higher. Currents in the channel and entrance bay showed the development of a circulation cell between the jetties, unique to this wave direction. Differences in predicted velocity magnitude of up to 0.5 m/s were observed in the channel, related to the relative size of the predicted circulation cell. MRSG differences were minimal in the channel itself.

For wave spectra generated with dominant direction A, the greatest differences between coupled forms of the models in terms of current speeds are observed. Significant portions of the navigation channel show a 0.4 m/s difference in current magnitude with some areas showing up to 0.6 m/s differences. Current magnitude differences of up to 1.0 m/s were observed in non-navigational areas of the channel. Wave height distribution is also significantly different between coupled cases for this direction. In contrast to the other dominant wave directions, for direction A waves, the two-way coupled wave heights were 0.4 to 0.8 m higher than the one-way coupled model case for almost the whole area between the offshore bypassing bar and the back of the entrance bay. This result suggests that two-way coupling of the models increases in importance as wave direction is less aligned with the entrance channel and as wave energy (or perhaps wavelength) increases.

8.3. Comparison Near Peak Flood Tide

Flood tide at Humboldt Bay produces currents on the order of 1.0 m/s between the jetties. It was expected that differences between coupling forms of the model would be more significant in the presence of these moderate tidal currents. Contrary to initial expectations, differences in model output at flood tide were less significant than at slack tide in all cases except with large waves coming directly down the entrance. Predicted current fields, wave heights, and radiation stress gradients are compared to quantify the significance of input conditions on comparative coupled cases at this tidal stage.

8.3.1. Model Dependence on Wave Spectra, Direction C

8.3.1.1. Current Fields.

At flood tide, with waves directly in line with the entrance channel, little difference in current fields was observed for the uncoupled case and model cases 1Co and 1Ct (Figure 8.24, Figure 8.25, and Figure 8.26). For the uncoupled case as well as with the coupled cases, current rates averaged 1.1 to 1.3 m/s across the width of the entrance during peak flood. Also, in all cases the highest velocities occurred in the center of the entrance channel, particularly over the channel shoal. Primary differences between the uncoupled and the 1Co model cases were in area B and along the shore. Less visible from the figures, but clear from calculations, is the trend towards higher currents in the navigation channel for the coupled cases. Differences between the 1Co and 1Ct cases can be seen in Figure 8.27. In this case, the two-way coupled model predicted higher currents along the inside of the north jetty, while the one way coupled model predicted higher currents in the navigation channel. Overall the difference in current magnitude was limited to a peak value of 0.08 m/s within the entrance.

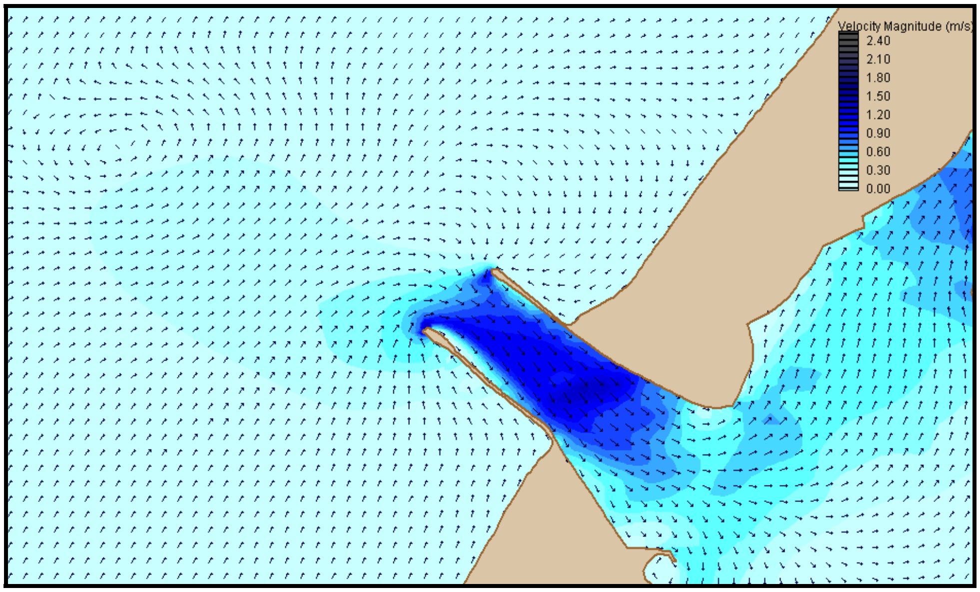

Figure 8.24. Velocity field at peak flood tide for model run 1Cu.

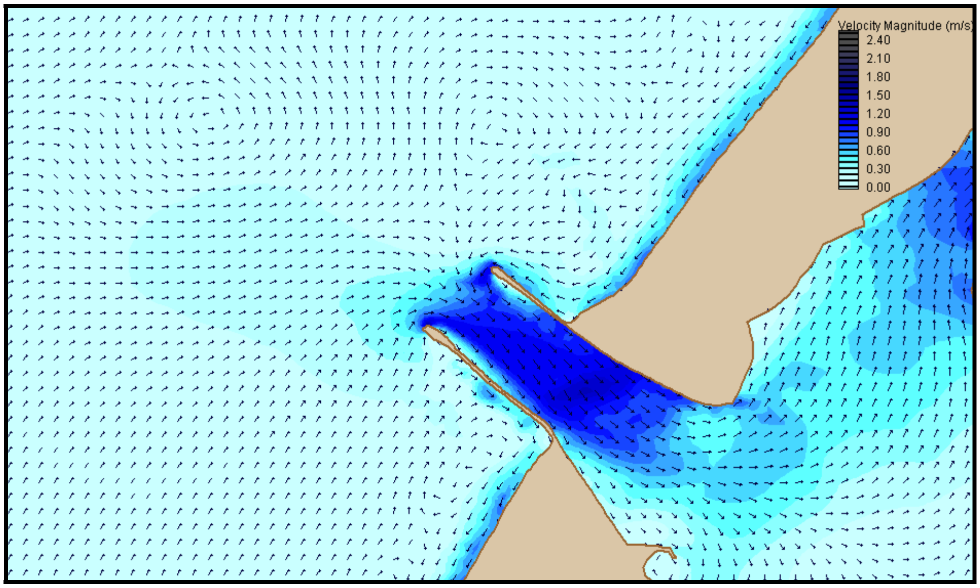

Figure 8.25. Velocity field near peak flood tide for model run 1Co. Currents along the shore and in the entrance showed much the same pattern as in the uncoupled and two-way coupled cases.

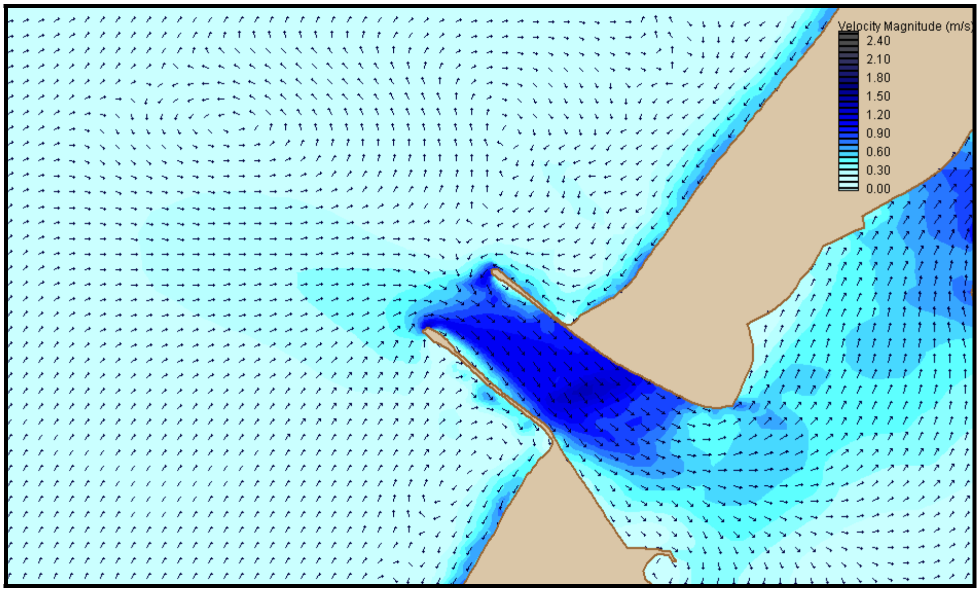

Figure 8.26. Velocity field near peak flood tide for model run 1Ct. One-way coupled currents were slightly higher over most of the domain than two-way coupled currents.

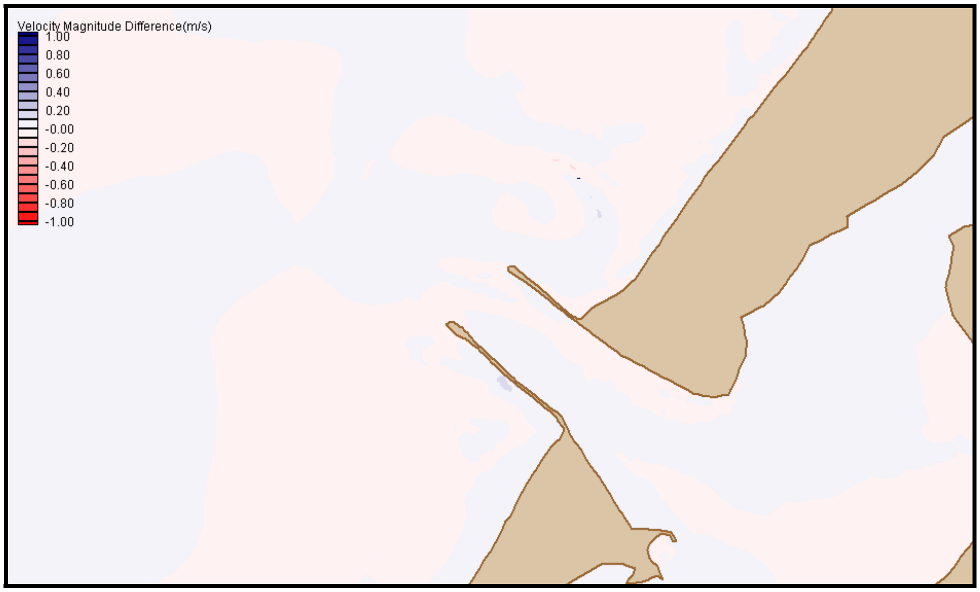

Figure 8.27. Near peak flood tide difference magnitude of current velocities for model runs 1Co and 1Ct. Two-way output was subtracted from one-way output.

For the 3Co model run, currents near peak flood tide were spread over 80% of the width of the entrance and averaged 2.2 m/s (Figure 8.28). Large circulating current fields both to the north and to the south of the entrance are predicted in both one and two-way coupled model runs but not in the uncoupled case or in the 1Co and 1Ct cases. In the 3Ct model run, higher currents funneled into the navigation channel near the channel shoal (Figure 8.29). Overall average current speed within the entrance of 2.1 m/s was 0.1 m/s less than in the 3Co case. The 3Cu model case showed higher currents over the shallower north side of the entrance channel than the 3Co case, while the 3Co case showed higher current rates in the navigation channel (Figure 8.30). In general, the 3Ct case showed higher currents in the navigation channel than the 3Co case, particularly near the channel shoal and into the turning basin. From Figure 8.31 it can be seen that current rates in shallower north side of the entrance and over the channel shoal were higher in the 3Co case than in the 3Ct case. Differences in current magnitude between one-way and two-way coupled cases in the navigation channel at this time averaged 0.54 m/s and were as large as 0.78 m/s in places. It should be noted that the large average difference in current velocity is due to the dissimilar distribution of current within the entrance between coupling cases.

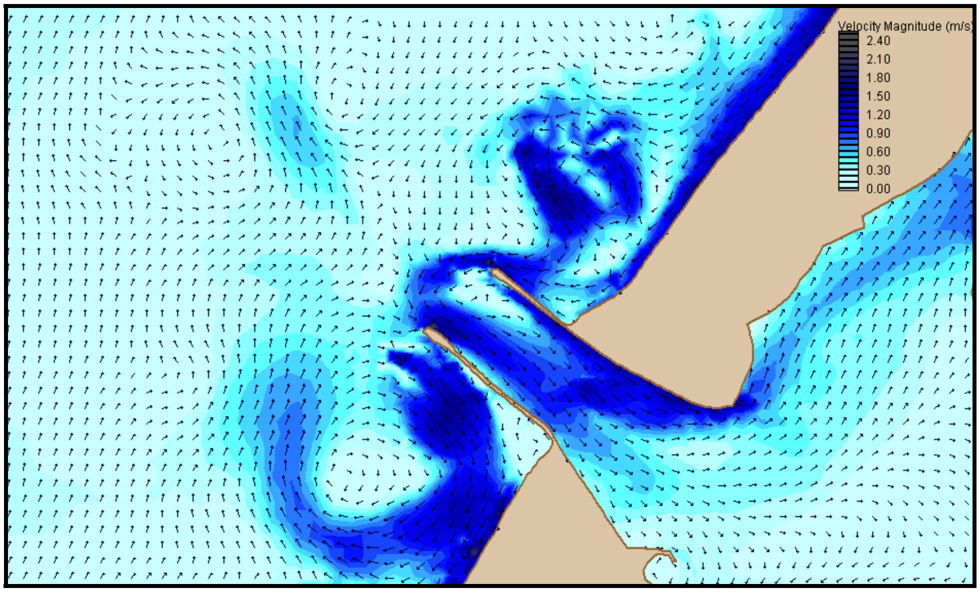

Figure 8.28. Typical velocity magnitude field for the 3Co model case near peak flood tide.

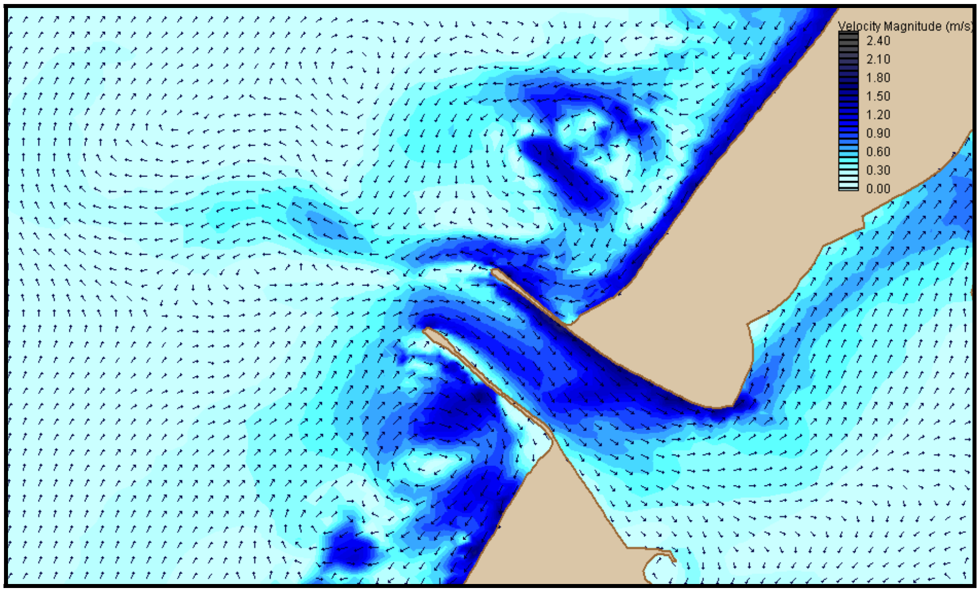

Figure 8.29. Typical velocity magnitude field for two-way coupled ADCIRC model at peak flood tide.

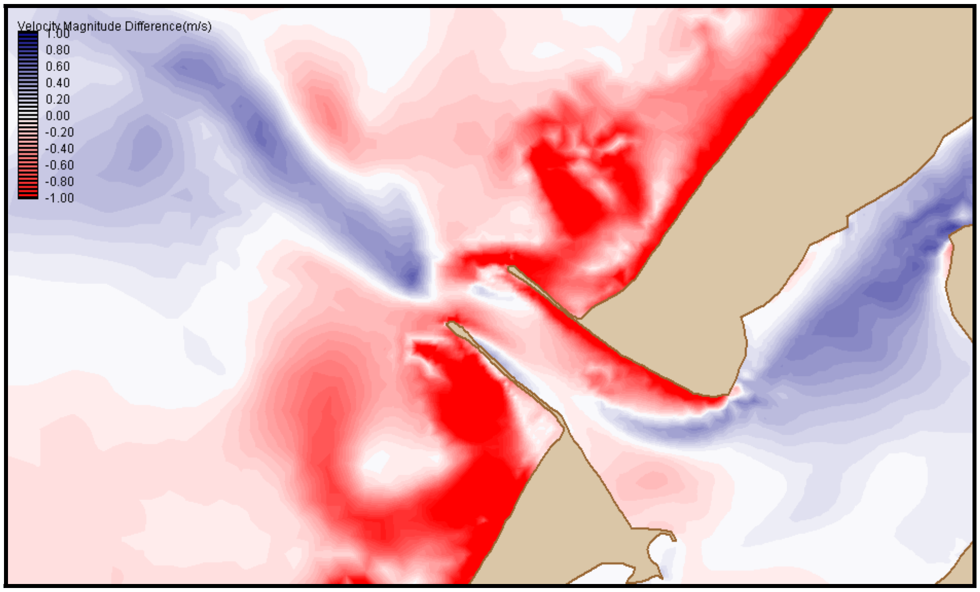

Figure 8.30 Difference in velocity magnitudes between model cases 3Cu and 3Co near peak flood tide. The 3Co magnitudes were subtracted from the 3Cu values.

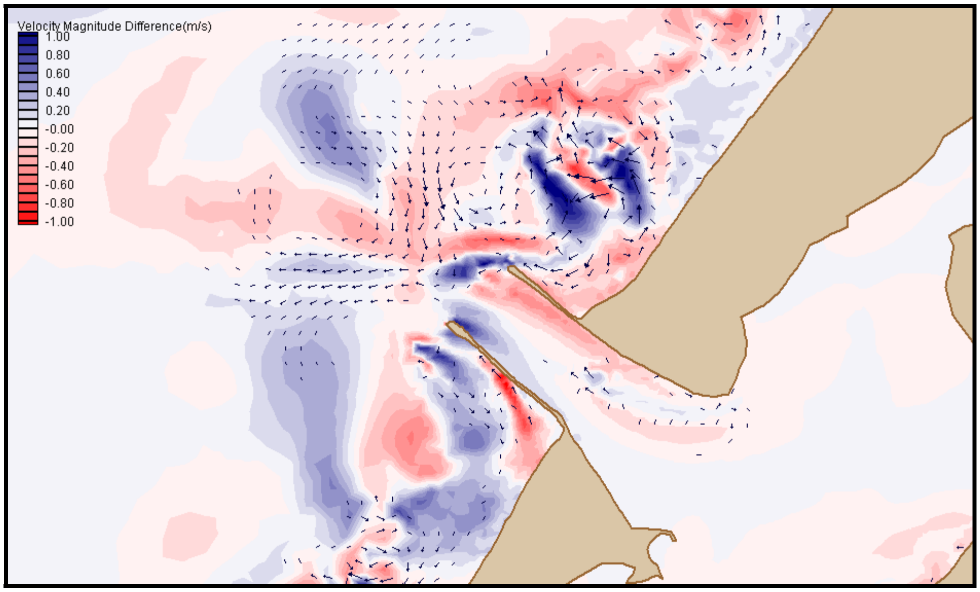

Figure 8.31. Difference in velocity magnitudes between the 3Co and 3Ct cases near peak flood tide. The two-way coupled magnitudes were subtracted from the one-way coupled values.

8.3.1.2. Wave Height Fields.

In the presence of a flooding tide, the two-way coupled model is expected to carry wave energy further into the bay than the one-way coupled case. In the HHW cases the two-way coupled model runs predicted larger waves in the entrance than one-way coupled model runs, even in very low current conditions.

As can be seen in Figure 8.32, the difference in predicted wave height between the 1Co and 1Ct model runs in the entrance bay is significant. Simply put, waves over the whole of the entrance average 0.37 m higher in the two-way coupled model case than in the one-way coupled model case. Also significant is the wave energy that is carried into the South Bay and towards the North Bay in the two-way coupled case. It should be noted that perception of the differences in wave height outside the entrance in Figure 8.32 is enhanced by the scale which was chosen to illustrate differences in the navigation channel.

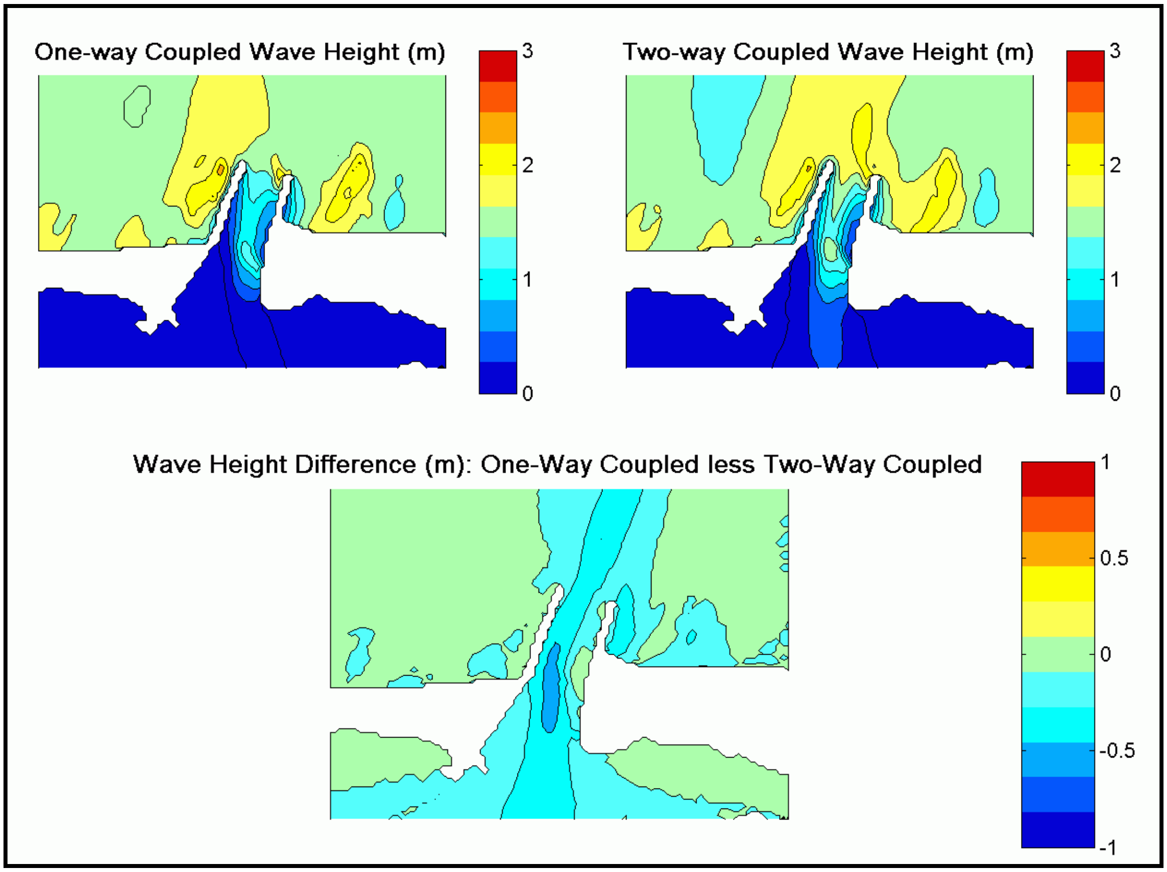

Figure 8.32. Comparison of wave height fields for model runs 1Co and 1Ct near peak flood tide. Note the waves in the two-way coupled model are up to 0.47 m higher in the Entrance Bay than in the one-way coupled model.

For higher energy input conditions, wave energy dissipation both within and outside the entrance played a significant role in shaping predicted wave height fields. In the 3Ct case at flood tide the current field is expected to reduce wave steepness and carry more wave energy into the entrance compared to the 3Co case. Wave height fields show that this is indeed the case. In Figure 8.33 the two-way coupled model case shows similar wave heights to the one-way coupled case up to the channel shoal at which point the two-way coupled solutions predicts significantly larger waves than the one-way coupled case for the whole entrance bay. The mean difference in wave height for the entrance bay is 0.54 m.

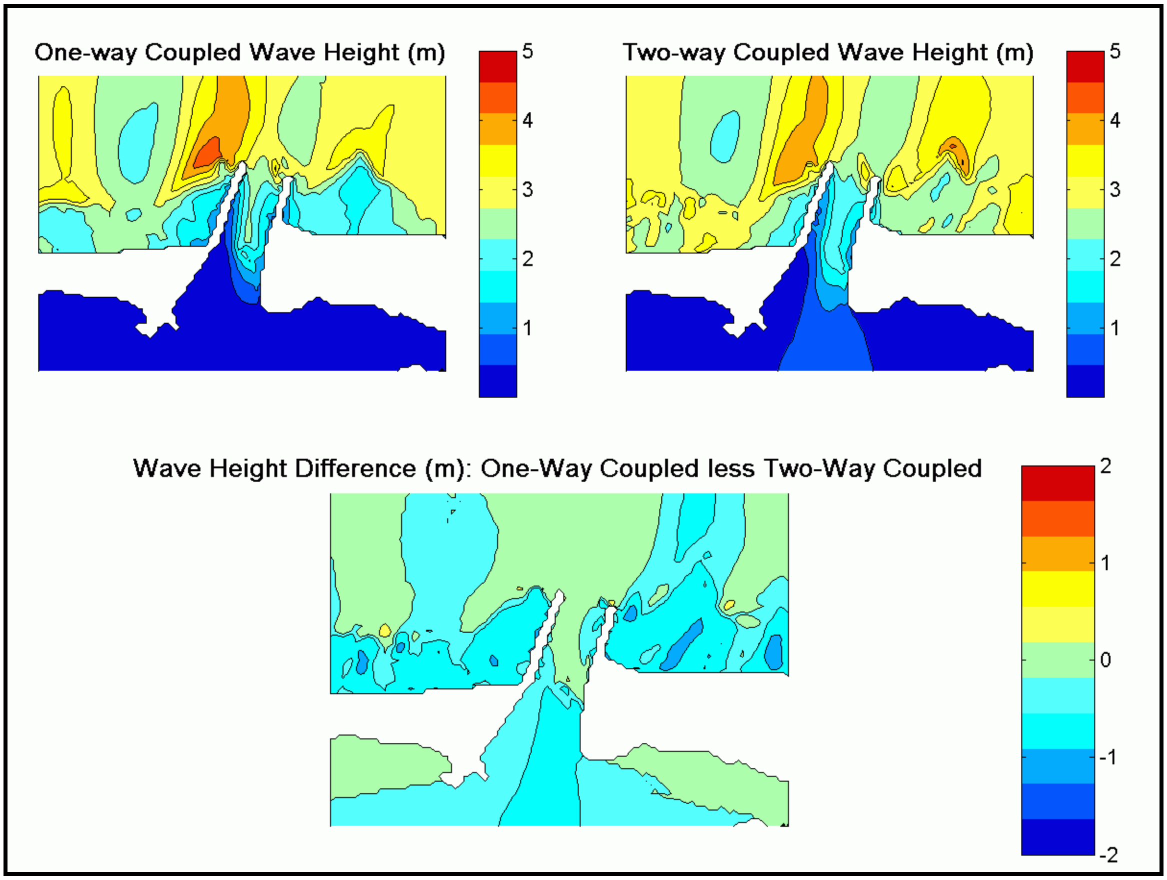

Figure 8.33. Comparison of wave height fields for model runs 3Co and 3Ct near peak flood tide. Two-way coupled solutions average 0.61 m higher than one-way solutions over the Entrance Bay.

8.3.1.3. Radiation Stress Gradient Fields.

Radiation stress gradient fields were also examined at flood tide. The magnitude of the radiation stress gradients for the largest study waves was fourteen times that of the smallest waves.

In the 1Co and 1Ct model cases, the effect of the flooding tide can be seen in that the radiation stress of the two-way coupled model over the channel shoal is much reduced from the one-way coupled case (Figure 8.34). It should be noted that the water level for each coupled version of the model are within 0.08 m of each other at this time in the entrance channel. Differences in MRSG are not limited to the channel shoal. Outside of the entrance the one-way coupled model predicted MRSGs up to 12% larger than the two-way coupled version.

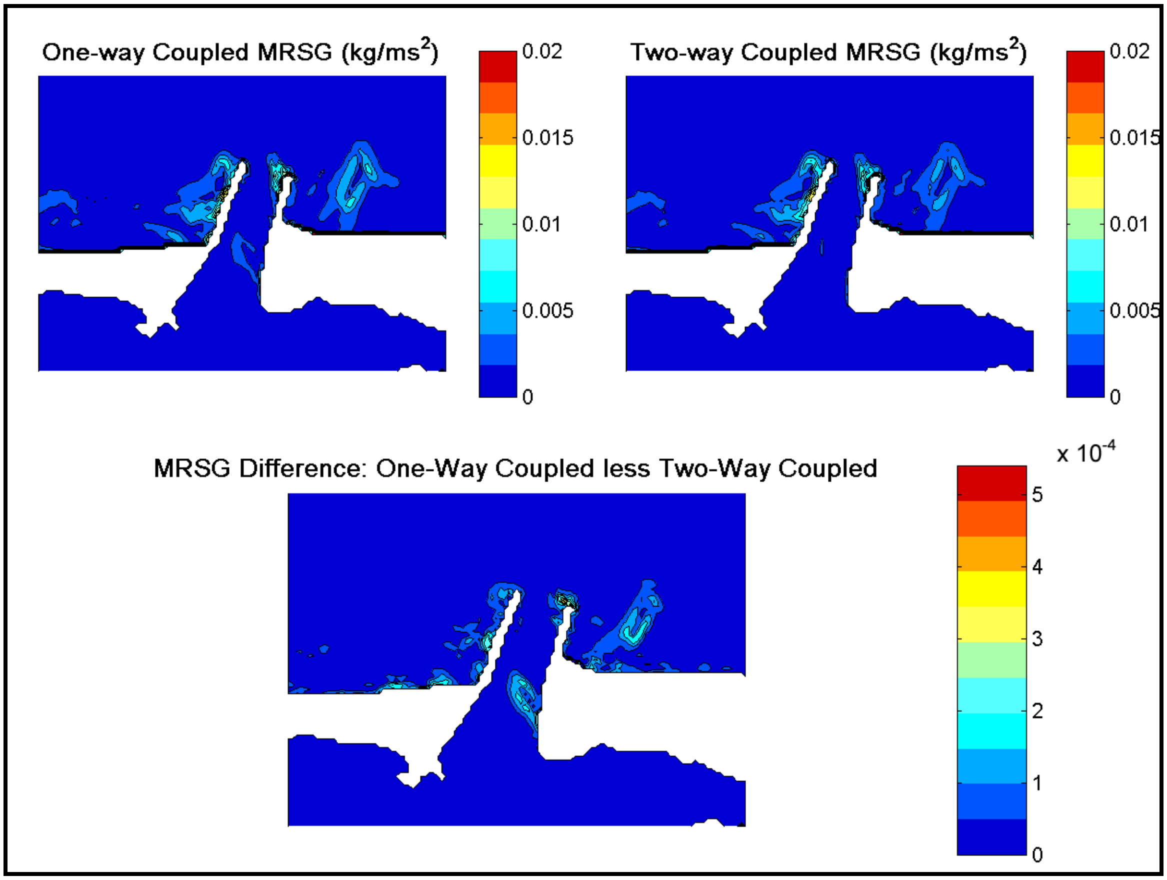

Figure 8.34. Comparison of the magnitude of radiation stress gradient fields generated by model runs 1Co (upper left panel) and 1Ct (upper right panel) near peak flood tide. The lower panel represents the magnitude of the vector difference between the two radiation stress gradient fields.

For the 3Co and 3Ct cases (Figure 8.35), the difference in MRSG over the channel shoal is still present along with a visible difference along the northern edge of the navigation channel. Outside of the entrance, the one-way coupled radiation stress gradient magnitudes were consistently larger than in the two-way coupled model runs. Interestingly, no increased MRSGs were observed from the wave energy dissipation that can be seen at the channel shoal in the wave height fields (Figure 8.33). It seems likely that the larger waves have broken before entering Humboldt Bay which would affect the amount of energy that could be transferred to the currents inside the entrance.

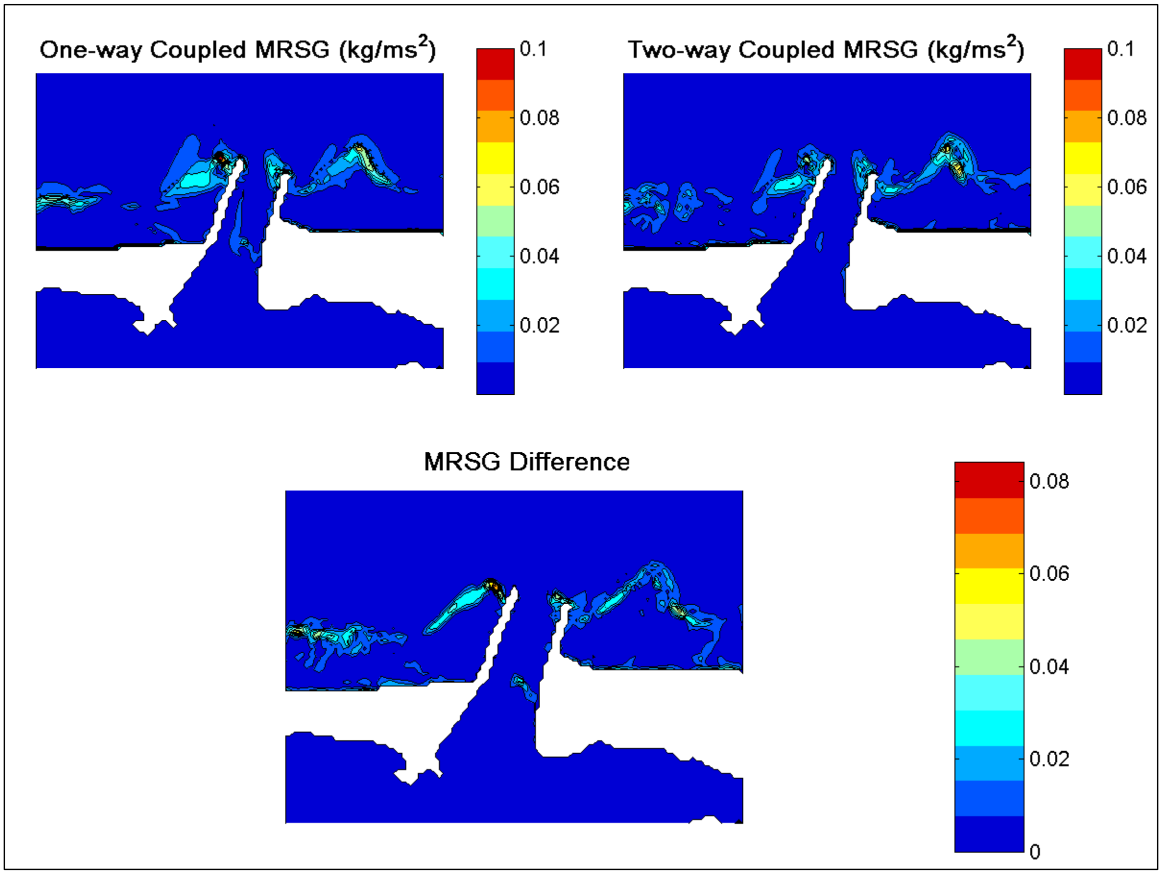

Figure 8.35. Comparison of the magnitude of radiation stress gradient fields generated by model runs 3Co (upper left panel) and 3Ct (upper right panel) near peak flood tide. The lower panel represents the magnitude of the vector difference between the two radiation stress gradient fields.

8.3.2. Model Dependence on Wave Spectra, Direction A

For direction A wave spectra, the difference between one-way and two-way model coupling is less significant than for direction C input wave spectra at flood tide. As in the case for direction C waves, differences between one-way and two-way coupled solutions can be tied to the ability of the two-way coupled model to turn wave energy into the bay much more efficiently than the one-way coupled model. Current fields show differences of up to 0.7 m/s in the navigation channel at flood with up to half of the channel area differing by 0.3 m/s in current velocity for the higher energy input wave spectra. Wave height differences are up to 0.4 m over large portions of the entrance bay. Radiation stress gradients are not significantly different for any of the wave cases.

8.3.2.1. Current Fields.

For direction A waves, the difference in current fields between coupled cases was limited for the lowest energy waves. Maximum differences in current magnitude for the small wave conditions at flood tide were less than 0.05 m/s. A visual comparison of Figure 8.36 and Figure 8.37 shows that currents in the one-way coupled case are slightly higher than the two-way coupled case over the channel shoal. A look at the difference field (Figure 8.38) shows that the main difference in current occurs outside of the entrance for this wave case. In both coupled cases, the waves drive the flooding current away from the south side of the entrance and the navigation channel. (Recall that the offshore waves are directed almost 53° south of the jetty orientation.)

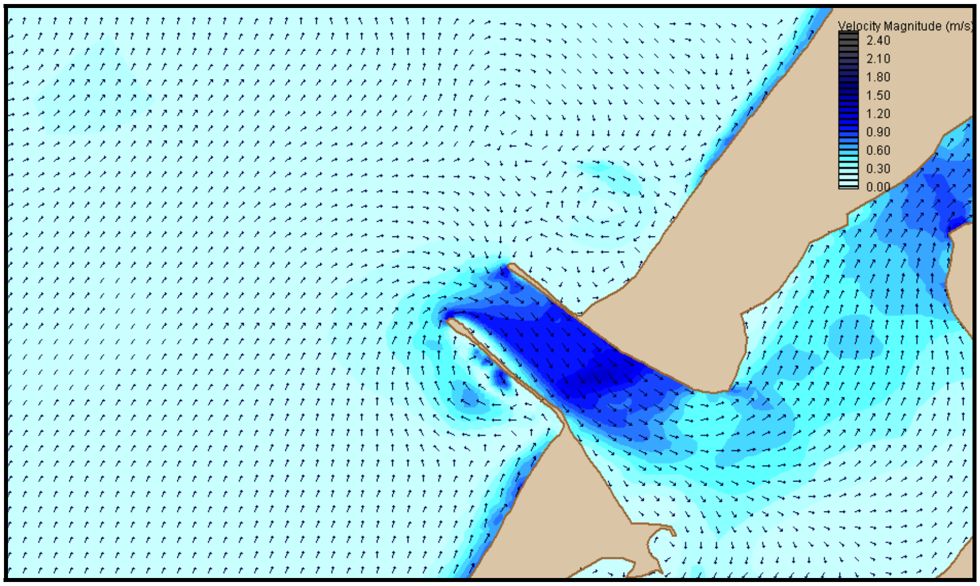

Figure 8.36. Typical velocity magnitude field for one-way coupled ADCIRC model near peak flood tide. Input wave spectra were from the 1Ao case.

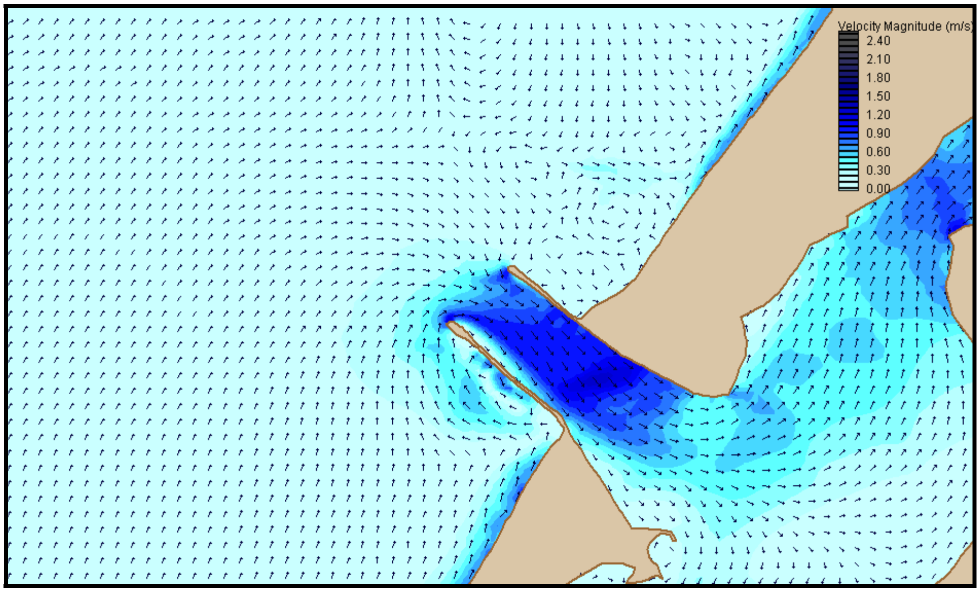

Figure 8.37. Typical velocity magnitude field for two-way coupled ADCIRC model near peak flood tide. Input wave spectra were from the 1At case.

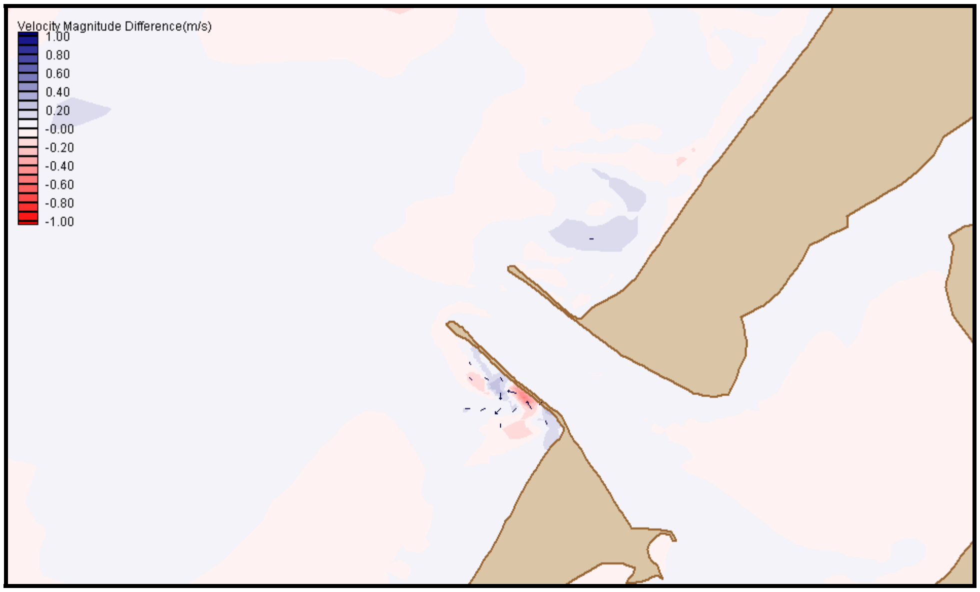

Figure 8.38. Difference in velocity magnitudes between 1Ao and 1At model cases near peak flood tide. The two-way coupled magnitudes were subtracted from the one-way coupled values.

For the larger waves of the 3Ao and 3At cases, the current fields at peak flood tide showed greater difference than in the smaller wave cases. In the 3Ao model run (Figure 8.39), strong currents along the inside of the north jetty and over the channel shoal reached up to 2.4 m/s. In this case though, flooding currents were spread over most of the width of the channel. In the 3At case (Figure 8.40), the strongest currents, reaching 2.5 m/s, were again along the inside of the north jetty and over the channel shoal. The primary difference between coupling cases in the entrance occurs in the navigation channel where the one-way coupled model predicts currents along the south jetty up to 0.41 m/s higher than the two way coupled model (Figure 8.41). Currents in the north part of the channel are larger in the two-way coupled case, but only by an average of 0.10 m/s. Current patterns outside of the entrance are similar in each case. Large differences in current magnitude at specific places outside the entrance are mostly due to the scale of the predicted circulation cells there.

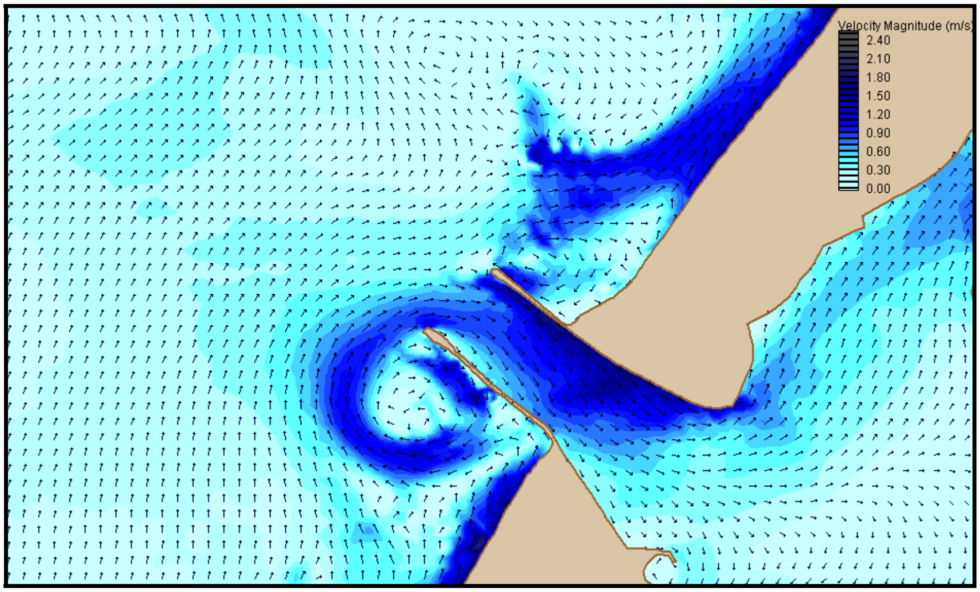

Figure 8.39. Velocity magnitude at near high tide for model run 3Ao. Modeled ebbing current can be seen as the model data point falls shortly after HHW. Peak currents are over the channel shoal.

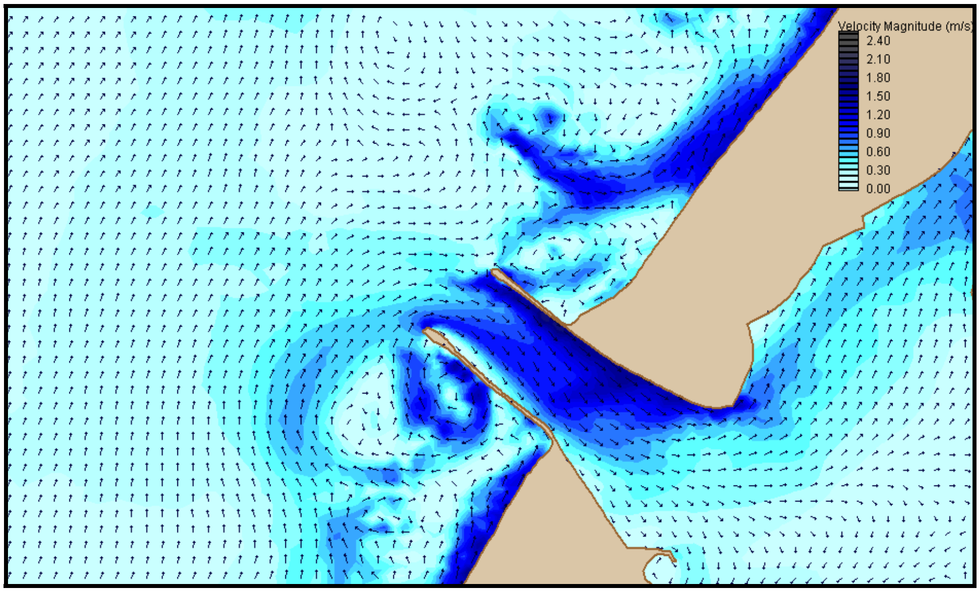

Figure 8.40. Velocity magnitude at near high tide for model run 3At. Modeled ebbing current can be seen as the model data point falls shortly after HHW. Peak currents are over the channel shoal.

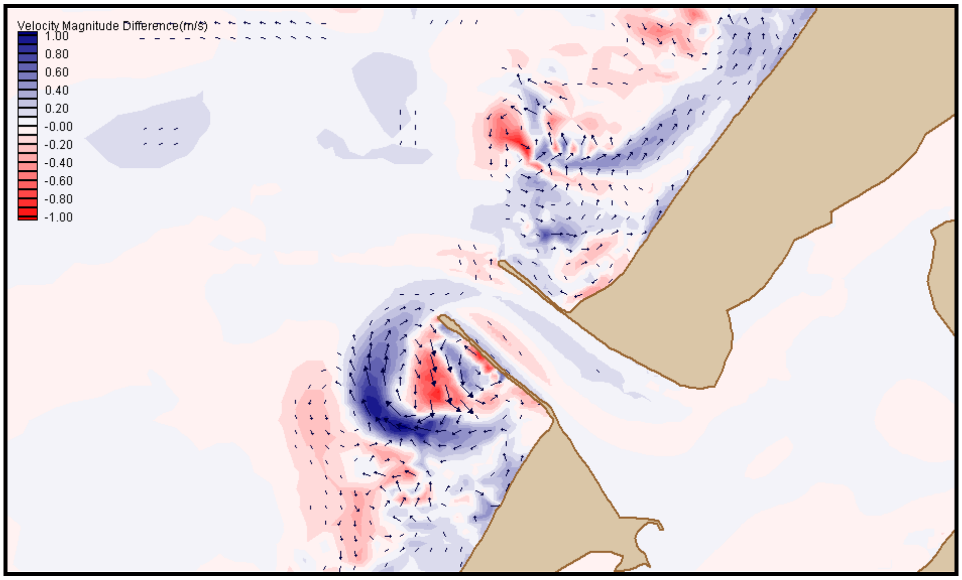

Figure 8.41. Difference in velocity magnitudes between the 3Ao and 3At cases near peak flood tide. The two-way coupled magnitudes were subtracted from the one-way coupled values.

8.3.2.2. Wave Height Fields.

Wave height differences between coupling cases for direction A waves were relatively small in all but the largest wave conditions. For 1Ao and 1At cases, a maximum height difference of 0.23 m was observed near flood tide. Wave height fields for this wave case are very similar to the results for the 1Co and 1Ct wave cases. As can be seen in

Figure 8.42, over the navigation channel and into the Entrance Bay, the two-way model case predicts waves on average 0.18 meters higher than the one-way case. Although these values are small, the two-way coupled model consistently predicts higher wave heights in the entrance channel and entrance bay than the one-way coupled case.

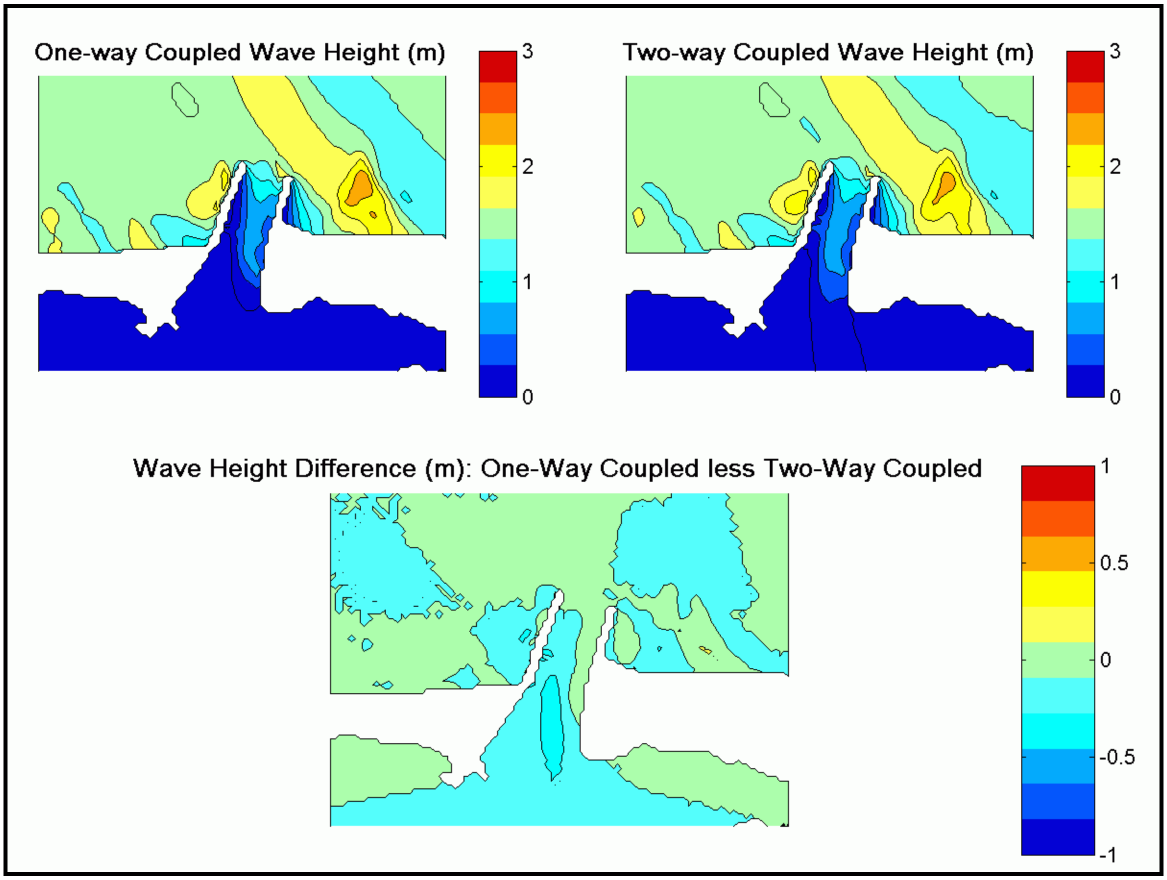

Figure 8.42. Comparison of wave height fields for model runs 1Ao and 1At near peak flood tide. Note the waves in the two-way coupled model are up to 0.23 m higher in the Entrance Bay than in the one-way coupled model.

For the 3Ao and 3At cases, predicted wave height fields near peak flood tide showed much the same pattern that the 1Ao and 1At cases did. As can be seen from Figure 8.43, the main difference in wave height fields between the larger and smaller wave cases is in the scale. Over the whole entrance channel and Entrance Bay, the two-way coupled model predicts 0.53 m larger waves on average than the one-way coupled model.

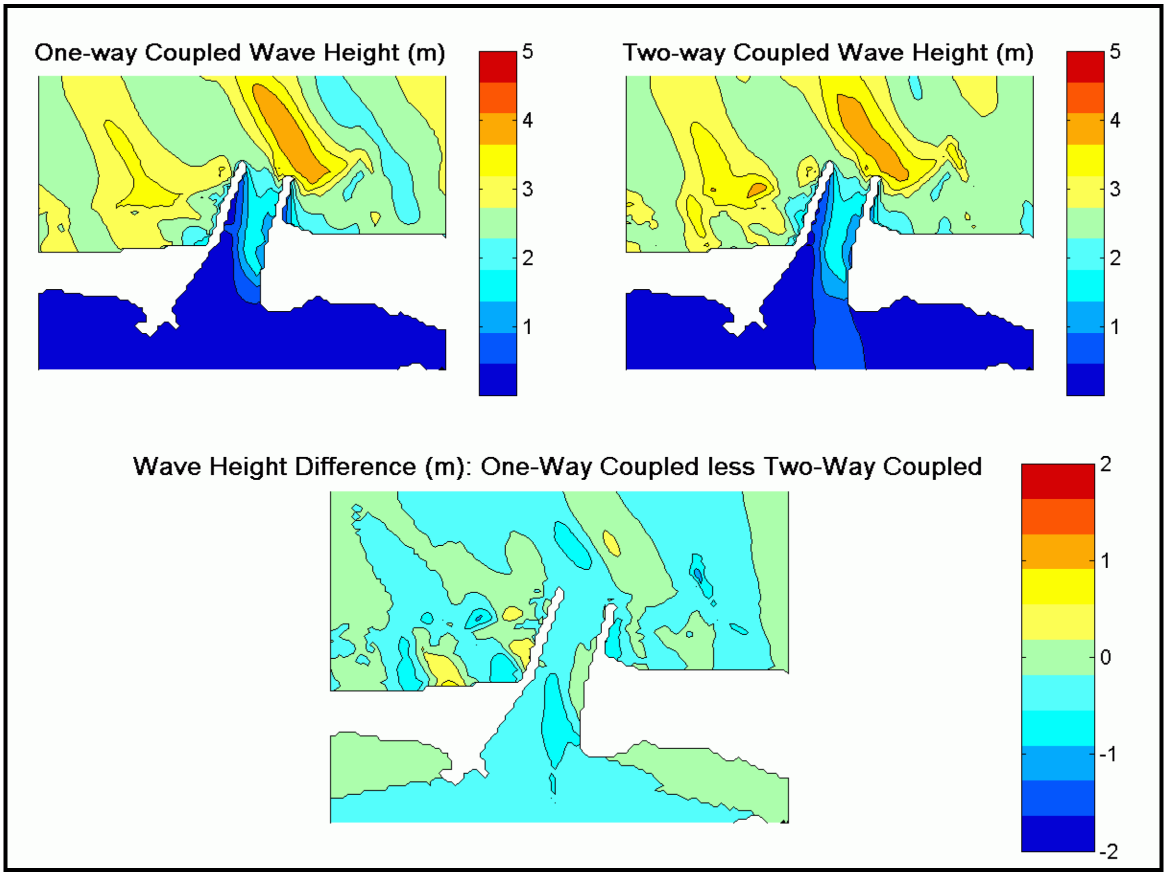

Figure 8.43. Comparison of wave height fields for model runs 3Ao and 3At near peak flood tide. Two-way coupled solutions average 0.48 m higher than one-way solutions over the Entrance Bay.

8.3.2.3. Radiation Stress Gradient Fields.

Differences in the MRSG fields between coupling cases for direction A spectra were less than those for direction C spectra. For the 1Ao and 1At cases, the model runs predict very little radiation stress gradient in the entrance and thus very little difference between coupling cases. For the 1At case, the MRSGs are slightly elevated over the channel shoal as compared to the MRSGs from the 1Ao case (Figure 8.44). The difference was less than 10% of predicted values over the channel shoal and less than 5% over the rest of the entrance.

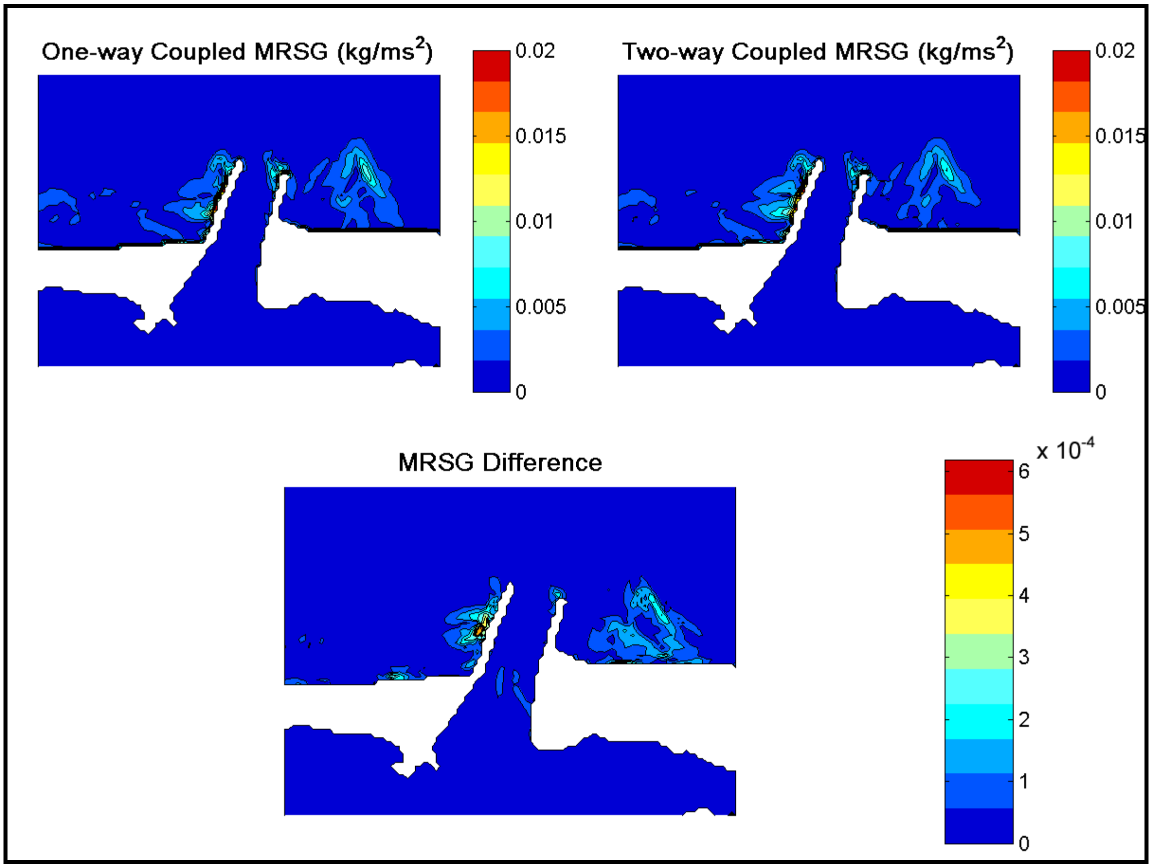

Figure 8.44. Comparison of the magnitude of radiation stress gradient fields generated by model runs 1Ao (upper left panel) and 1At (upper right panel) near peak flood tide (+ 0.13 m water level). The lower panel represents the magnitude of the vector difference between the two radiation stress gradient fields.

For the larger waves, the 3Ao and 3At cases (Figure 8.45), differences between coupling cases in the MRSG fields were even less significant than for the 1Ao and 1At model runs. Magnitudes for higher energy wave solutions were nearly six times greater through the entrance and more than ten times greater in area B (Figure 8.2) than in the lower energy wave cases. However, relative differences between coupling cases in the entrance were about 4% of calculated values.

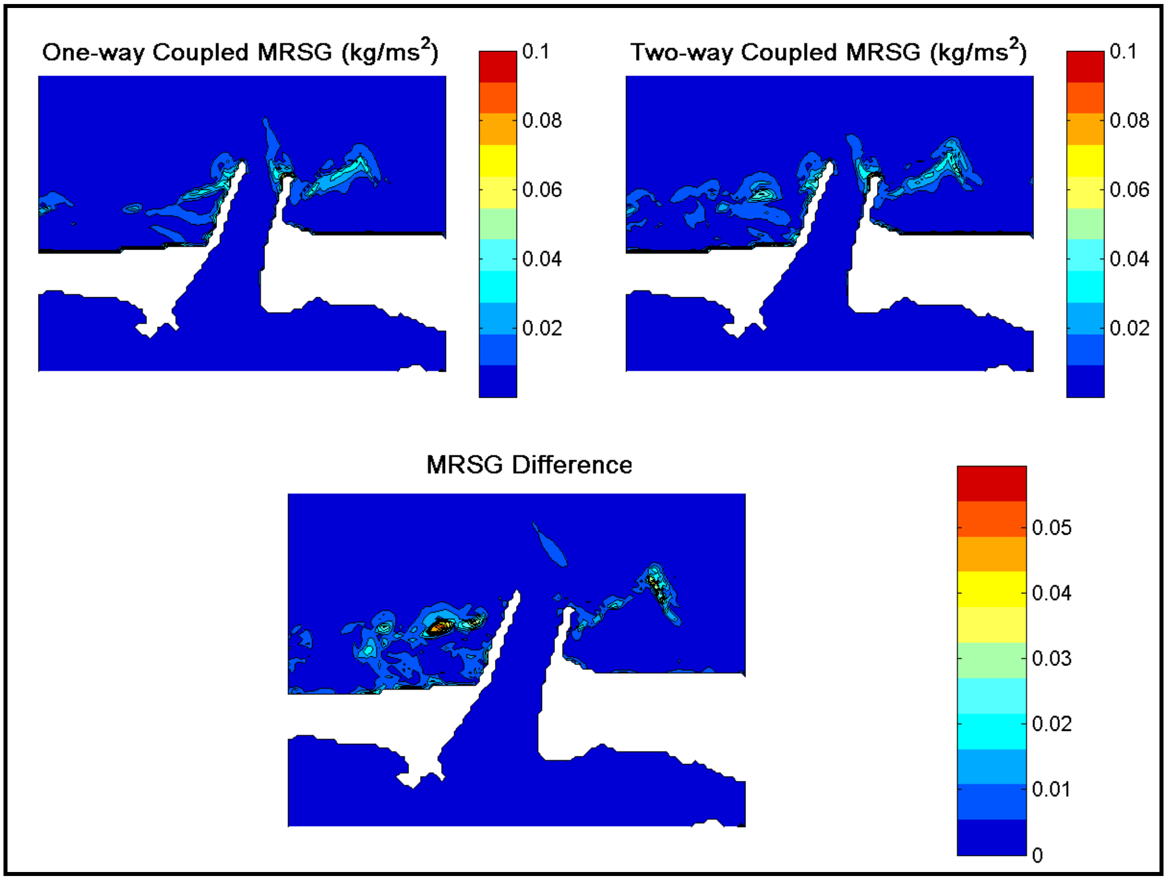

Figure 8.45. Comparison of the magnitude of radiation stress gradient fields generated by model runs 3Ao (upper left panel) and 3At (upper right panel) near peak flood tide. The lower panel represents the magnitude of the vector difference between the two radiation stress gradient fields.

8.3.3. Model Dependence on Dominant Direction of Input Wave Spectra Near Peak Flood Tide

As at slack tide, it is important to quantify the effect of wave direction on both one-way and two-way coupled model output. It was expected that the wave direction would be more significant at flood tide than that at slack tide.

8.3.3.1. Direction Characteristics for Small Waves.

As expected the significance of wave direction on model results between coupling increases in the presence of flooding currents. For current magnitude fields, wave heights, and radiation stress gradient magnitudes, two-way coupled solutions show greater sensitivity to changes in wave direction than one-way coupled solutions.

Differences in flooding currents at the entrance for the one-way coupled solutions differed by as much as 0.3 m/s between wave directions for the 1Ao and 1Co cases. For the two-way coupled cases (1At and 1Ct) the maximum difference in current velocity between wave directions increased to 0.5 m/s at flood tide.

For the one-way coupled model case, the wave heights in the navigation channel differ by 0.63 m on average between 1Ao and 1Co cases. Between cases 1Bo and 1Co, the difference averages 0.36 m over the same area. Mean difference in wave height between 1At and 1Ct solutions was 0.71 m. Between 1Bt and 1Ct wave solutions, the mean difference was 0.33 m.

For the small wave cases, MRSG values in the entrance are almost unaffected by wave direction for one-way coupled model runs. For the two-way coupled model runs, there is a small difference in the entrance between the 1Ct case and the 1At case. This difference is small, on the order of 10% of maximum gradient magnitude in the entrance.

8.3.3.2. Direction Characteristics for Larger, Longer Waves.

For the higher energy, longer wavelength input spectra, the impact of different wave directions on model output at flood tide is clearly seen in differing current velocity fields and wave heights. Currents fields differ by an average of 0.84 m/s between directions in the one-way coupled model. In the two-way coupled model, differences in currents from the 1Ct and 1At wave cases averaged 1.03 m/s in the entrance. The relatively large difference in current rates is based more on displacement of the current patterns. For both coupled forms of the model, the direction C spectra concentrated currents down the navigation channel, with some higher currents over shoals. For direction A and direction B cases, model solutions at flood tide for one-way and two-way coupling were much more similar than for direction C; the peak currents for the A and B cases occurred in the northern half of the channel as well as over the significant shoals.

Wave height distribution in the entrance varied as a function of wave direction for high energy input spectra in much the same way as current magnitudes do. Between the 3Ao and 3Co model runs height differences of up to 0.67 m in the navigation channel were observed, with an average difference in the entrance channel of 0.28 m. For the 3At and 3Ct model runs the mean difference was 0.34 m with a maximum difference of 0.81 m in the entrance channel.

Radiation stress gradient magnitudes in the entrance varied by direction for the high-energy input spectra. Differences in model calculations were primarily focused at the channel shoal.

8.4. Comparison Near Peak Ebb Tide

8.4.1. Model Dependence on Wave Spectra, Direction C

8.4.1.1. Current Fields.

Without coupling, the ebb jet at Humboldt fills much of the space between the jetties, narrowing as it approaches the jetty tips (Figure 8.46). Offshore the model predicts the ebb jet to remain relatively narrow and to sweep from south to north over the course of the ebb cycle. A large, low velocity circulation cell appears in the middle of the ebb cycle and spins off to the northwest as slack tide approaches. Current velocities reach 1.8 m/s over most of the width of the entrance. Peak velocities of 2.3 m/s were obtained.

For the smallest waves, cases 1Co and 1Ct, the current fields are deformed significantly near peak ebb. Both coupled cases show a slight southward deflection of the ebb jet over the Humboldt Bar as well as a narrowing of the current stream in the entrance channel. Also both coupled cases show a net current into the channel along the north jetty. The 1Co case (Figure 8.47) showed a maximum current speed of 2.2 m/s in the entrance channel with mean current rate over the navigation channel 1.5 m/s. The 1Ct case (Figure 8.48) showed a maximum current rate of 2.1 m/s in the entrance with a 1.5 m/s mean current speed in the navigation channel. Comparison of the 1Co and 1Ct cases (Figure 8.49) shows that the one-way coupled case deflects the current stream southward just offshore of the entrance as compared to the two-way coupled case. In addition, the 1Co case generated stronger currents (0.3 m/s) than the 1Ct case along the north jetty and over the channel shoal.

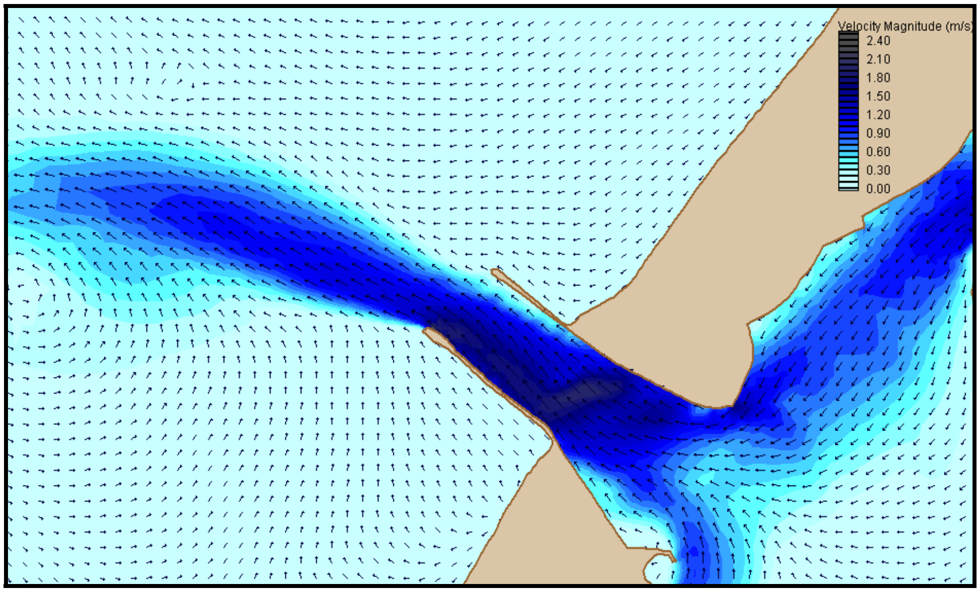

Figure 8.46. Velocity field for nears peak ebb tide from model case 1Cu. This shows the ebb jet near the middle of its predicted sweep from southeast to northwest over the course of an ebb tide.

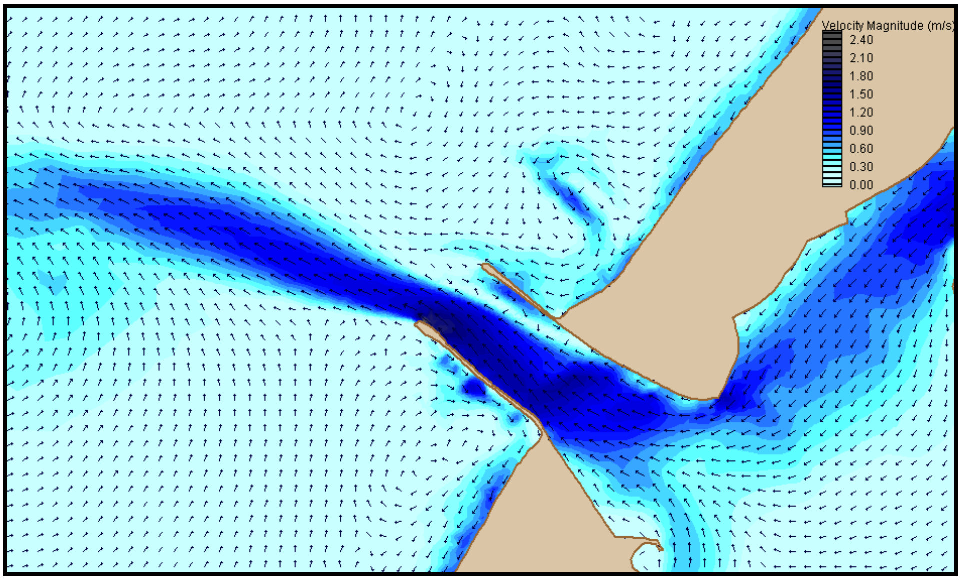

Figure 8.47. Velocity field for the 1Co model run near peak ebb tide.

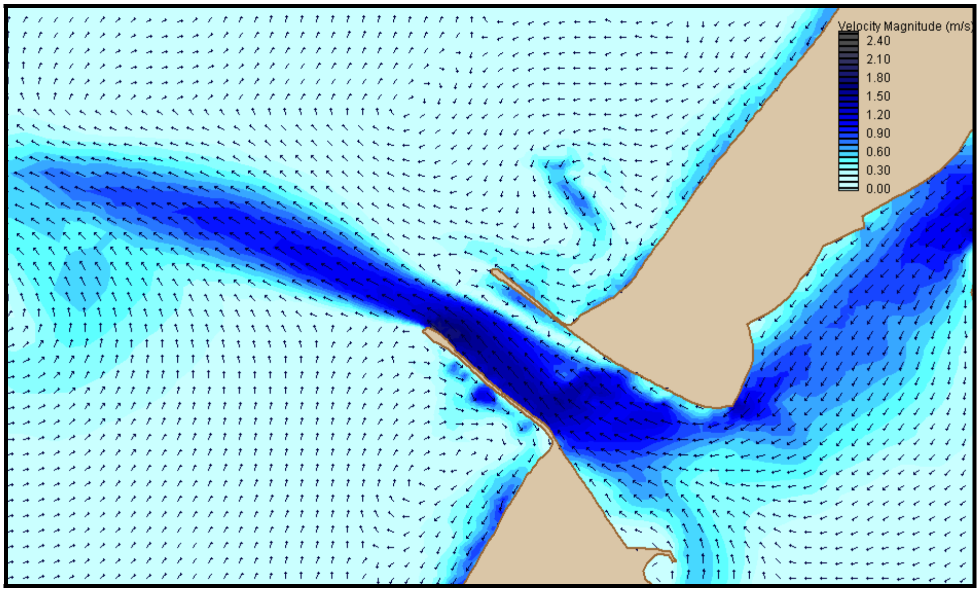

Figure 8.48. Velocity field for the 1Ct model run near peak ebb tide.

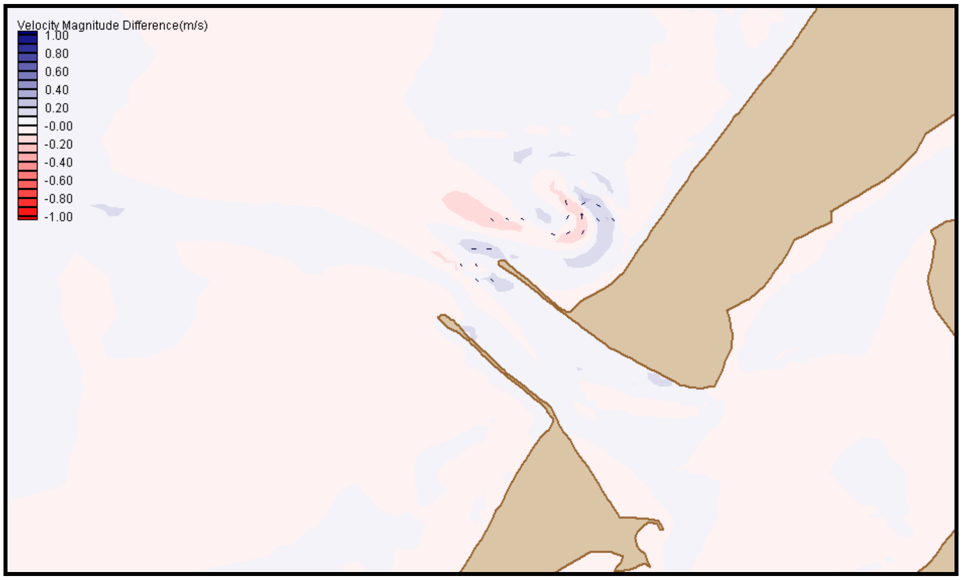

Figure 8.49. Difference in velocity magnitudes between 1Co and 1Ct model cases near peak ebb tide. The two-way coupled magnitudes were subtracted from the one-way values.

When the larger, longer wave spectra were used, the effect of coupling case on current field became much more evident. For the 3Co model run (Figure 8.50), the basic shape of the current fields remained the same as for the 1Co case, but currents in the navigation channel exceeded 4.1 m/s. Mean velocity magnitude in the navigation channel was 2.1 m/s and currents into the bay along the north jetty were as high as 2.4 m/s. Compared with the uncoupled model output, offshore currents in the 3Co case reached higher speeds and were confined to a 300 m wide channel along the south jetty. The difference field (Figure 8.52) for 3Cu and 3Co cases shows a southward deflection of the ebb jet in the one-way coupled case. In the 3Ct model (Figure 8.51), currents differed from the one-way model output over the entire entrance area. In the navigation channel the 3Ct model predicted peak currents of 2.2 m/s with a spatially averaged current of 1.6 m/s. Also in the two-way coupled case, the main current stream out of the channel was diverted north 170 m of the main current stream predicted in the one-way case. Also, in the 3Co case, extremely high currents are predicted at the inside tip of the south jetty, while in the 3Ct case these currents are not apparent. From the current magnitude difference field (Figure 8.53), it is clear that over the whole navigation channel and over the channel shoal, the one-way solution predicts significantly higher currents than the two-way coupled solution. Interestingly, the two-way coupled solution shows a stronger shoreward current along the inside of the north jetty than the one-way coupled solution.

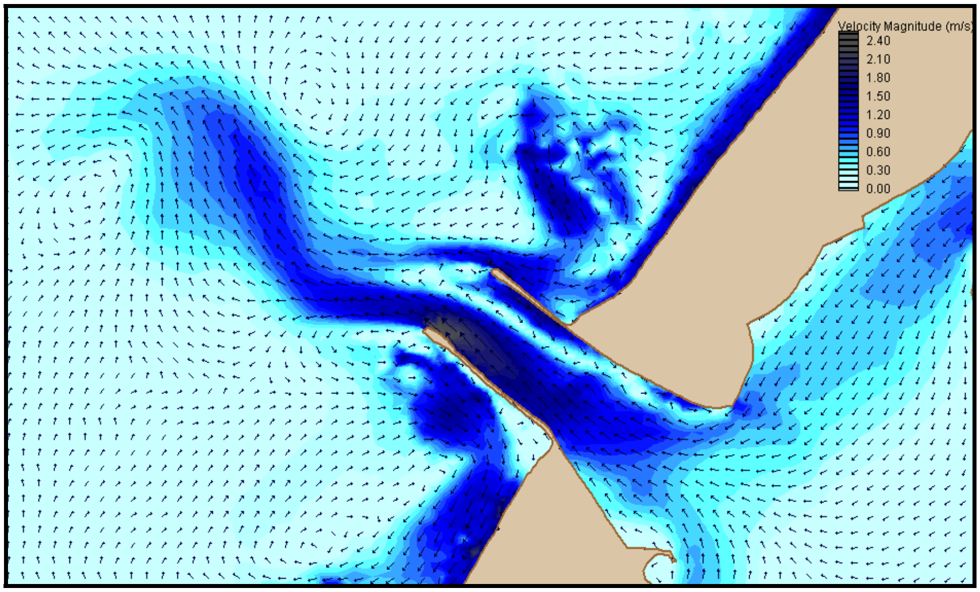

Figure 8.50. Typical velocity magnitude field for the 3Co model run near peak ebb tide.

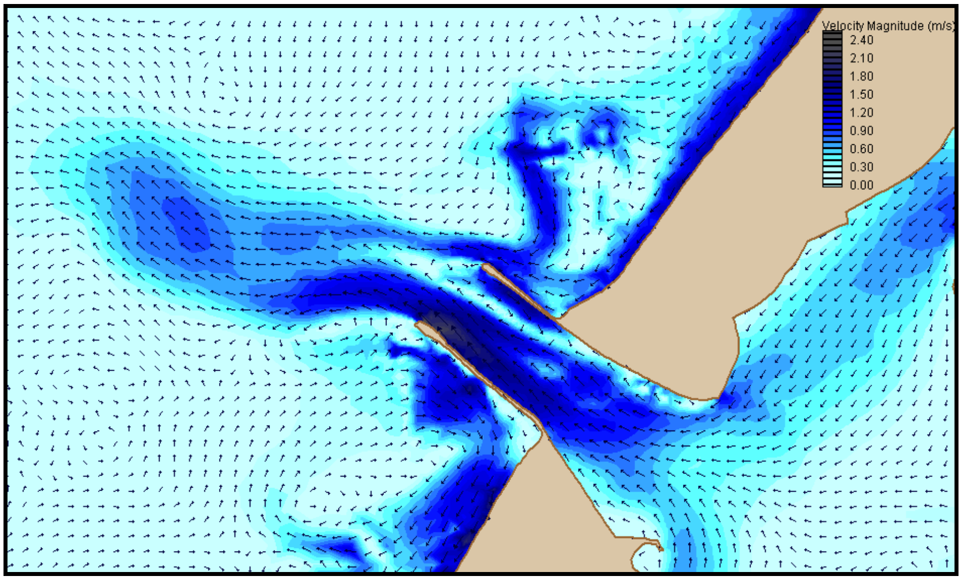

Figure 8.51. Typical velocity magnitude field for the 3Co model run near peak ebb tide.

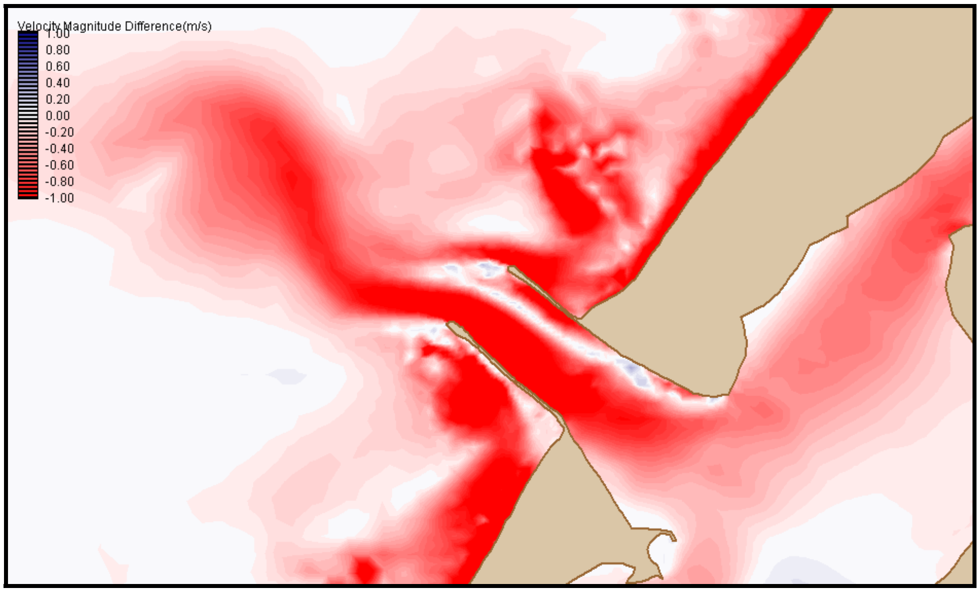

Figure 8.52. Difference in velocity magnitudes between uncoupled and one-way coupled model cases near peak ebb tide. The one-way coupled magnitudes were subtracted from the uncoupled values.

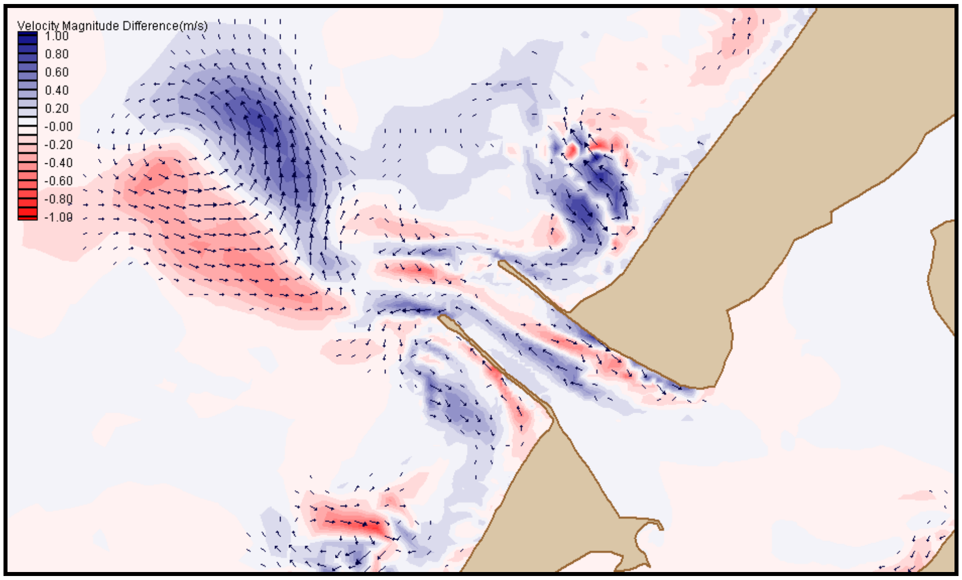

Figure 8.53. Difference in velocity magnitudes between 3Co and 3Ct model cases near peak ebb tide.

8.4.1.2. Wave Height Fields.

During ebb tide, wave energy is redistributed around the entrance at Humboldt for all wave cases. Wave heights in particular are affected more near peak ebb tide than any other tidal stage. The choice of coupling mode proved to be most significant for these ebb currents than for near slack and near maximum flood conditions.

For the lowest waves, cases 1Co and 1Ct (Figure 8.54), the mean difference in wave height in the channel was 0.5 m. Over the channel shoal, the two-way coupled case predicts waves up to 1.1 m higher than the one-way coupled case. Over the whole Entrance Bay, the two-way coupled solutions were at least 0.25 m larger than the one-way coupled solutions. Over the Humboldt Bar, the 1Ct case was up to 0.9 m higher than the 1Co case.

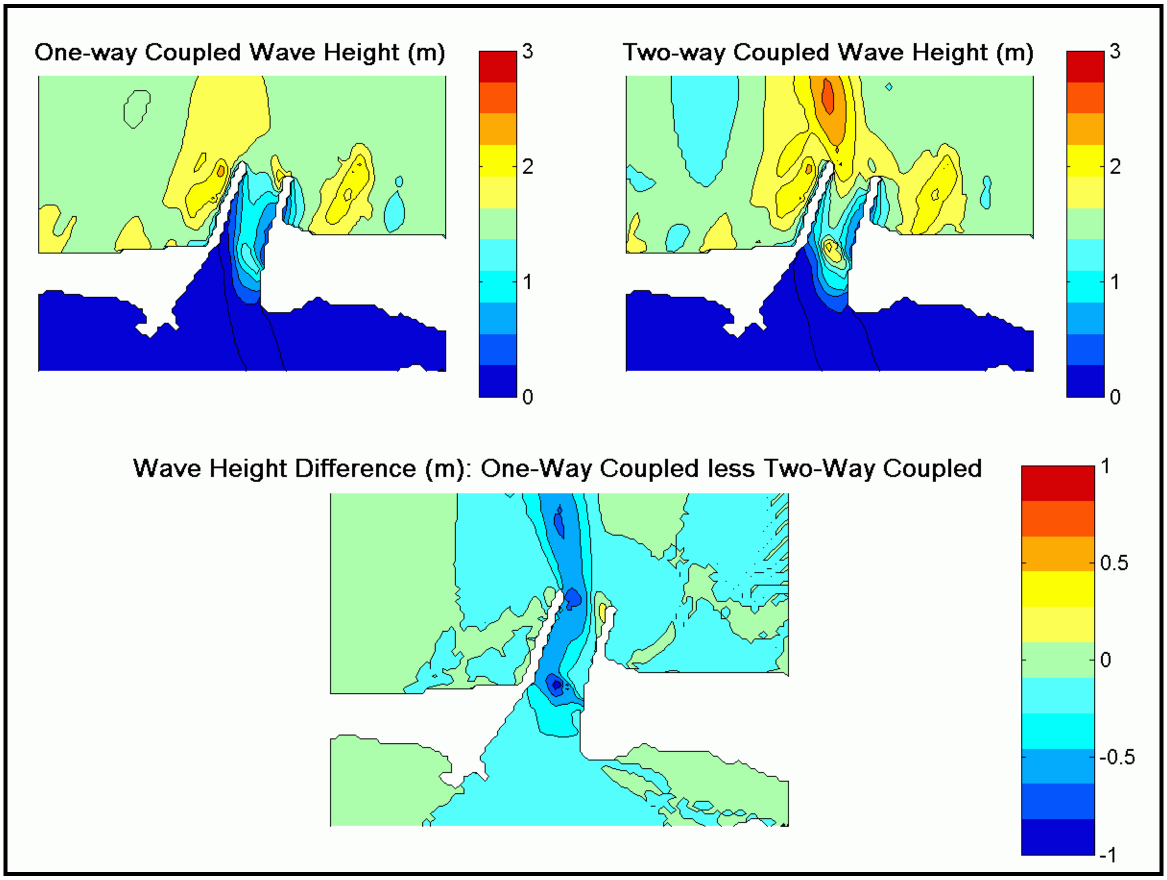

Figure 8.54. Comparison of wave height fields for model runs 1Co and 1Ct. Two-way coupled solutions were up to 1.1 m higher over the channel shoal and up to 0.9 m higher in the navigation channel than one-way coupled solutions.

For the 3Co and 3Ct cases, the difference in wave height fields near peak ebb tide was even more dramatic. Figure 8.55 shows differences of up to 2.8 ms in wave height near peak ebb tide between the coupling cases. On average, over the navigation channel the two-way coupled case showed waves that were 2.1 m higher than the one-way coupled case. The 3Ct solution also showed increased wave heights over the Humboldt Bar relative to the 3Co case. Waves in the Entrance Bay averaged 1.0 m higher in the two-way solution over the one-way solution. Unlike lower energy cases, differences in predicted wave height at the channel shoal were not as large as in the navigation channel.

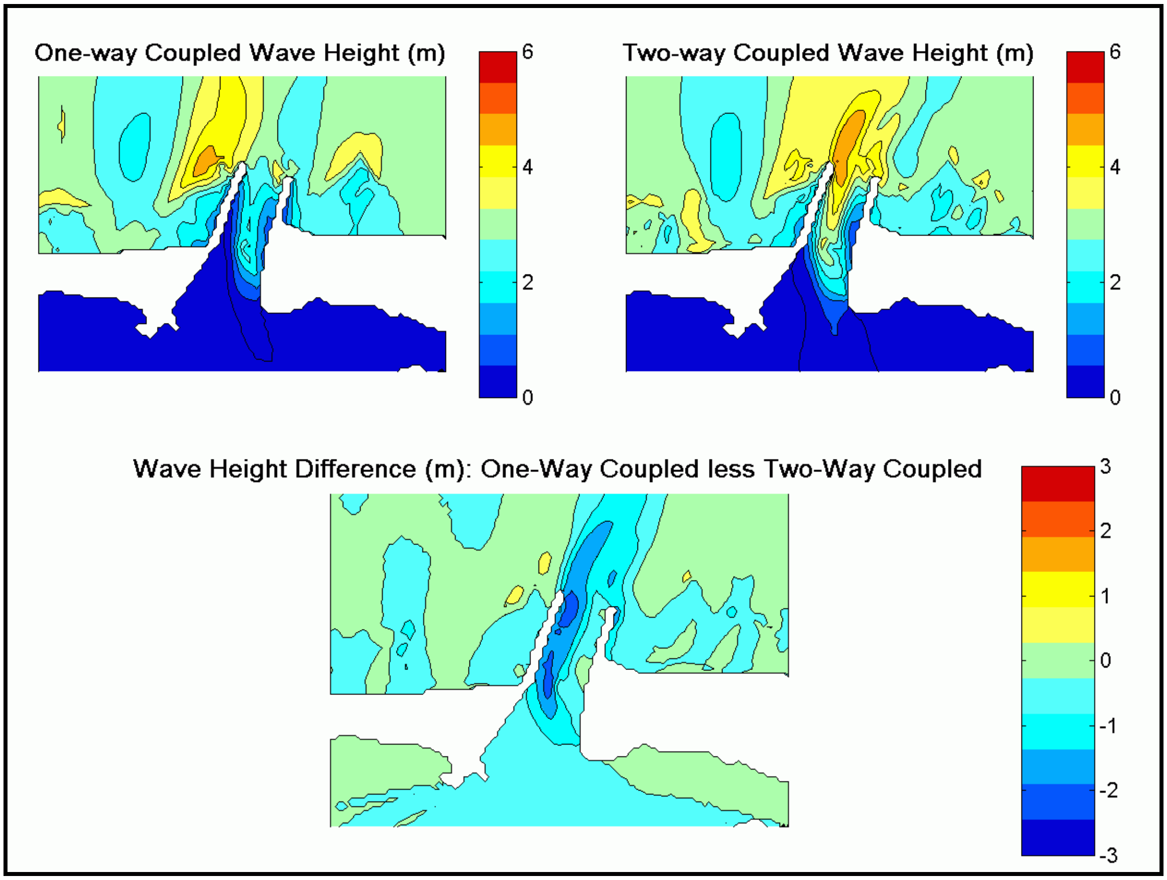

Figure 8.55. Comparison of wave height fields for model runs 3Co and 3Ct. Two-way coupled solutions were up to 2.8 m higher than one-way solutions in the navigation channel.

8.4.1.3. Radiation Stress Gradient Fields.

Radiation stress gradient fields confirm the presence of wave energy in the entrance that is already noticeable from wave height fields. Significant differences between coupled forms of the model are seen for the highest energy cases. For lower energy waves, cases 1Co and 1Ct, radiations stress gradient magnitudes differ most over the channel shoal. Note that the largest difference in wave height for these two cases occurred over the channel shoal also (Figure 8.54). Difference in MRSG for the lower energy wave cases peaked at 3.5 x 10^{-4} kg/ms^2 there.

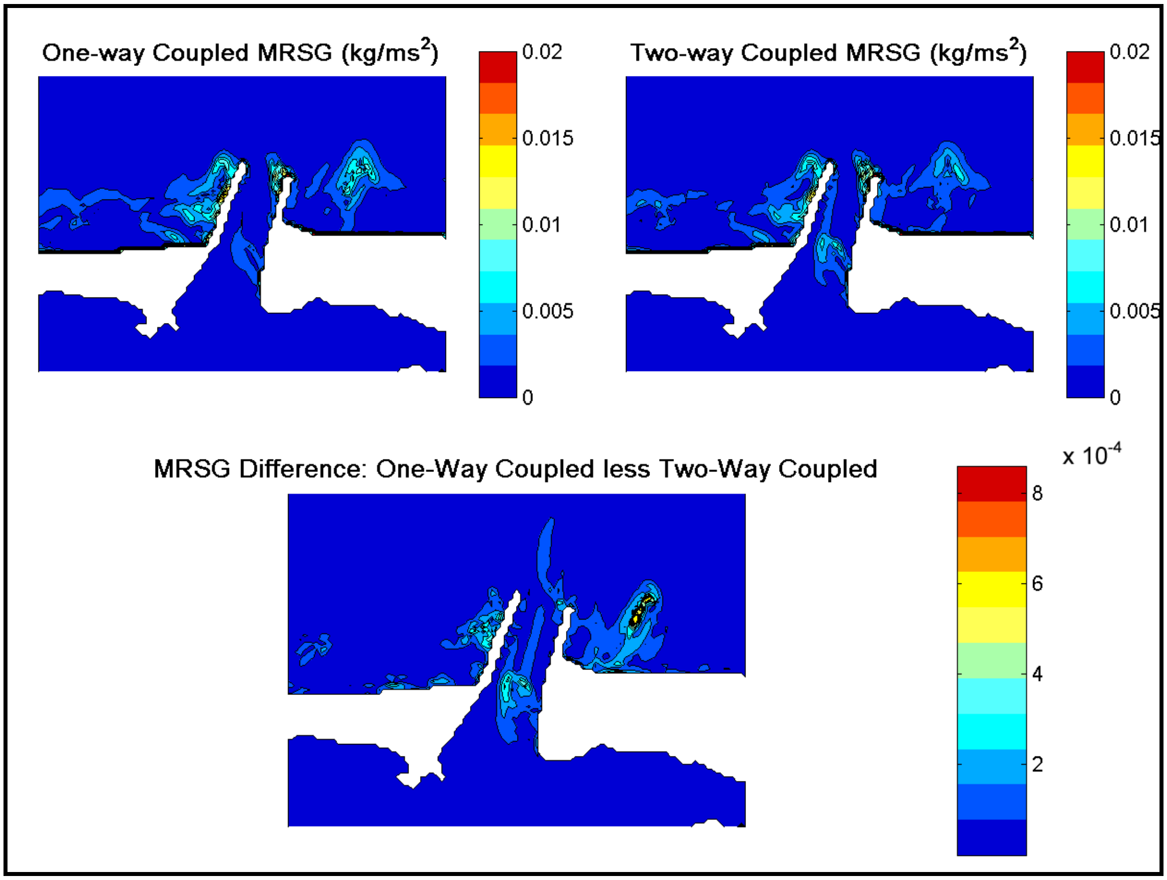

Figure 8.56. Comparison of the magnitude of radiation stress gradient fields generated by model runs 1Co (upper left panel) and 1Ct (upper right panel) near peak ebb tide. The lower panel represents the magnitude of the vector difference between the two radiation stress gradient fields.

The 3Co and 3Ct radiation stress gradient magnitude fields differ in the entrance, especially on the north side of the navigation channel (Figure 8.57). In the navigation channel, the two-way coupled model shows significant radiation stress gradients from the tips of the jetties to the channel shoal. These stresses relate to the deflection of the ebb jet to the north in the 3Ct case as seen in Figure 8.51.

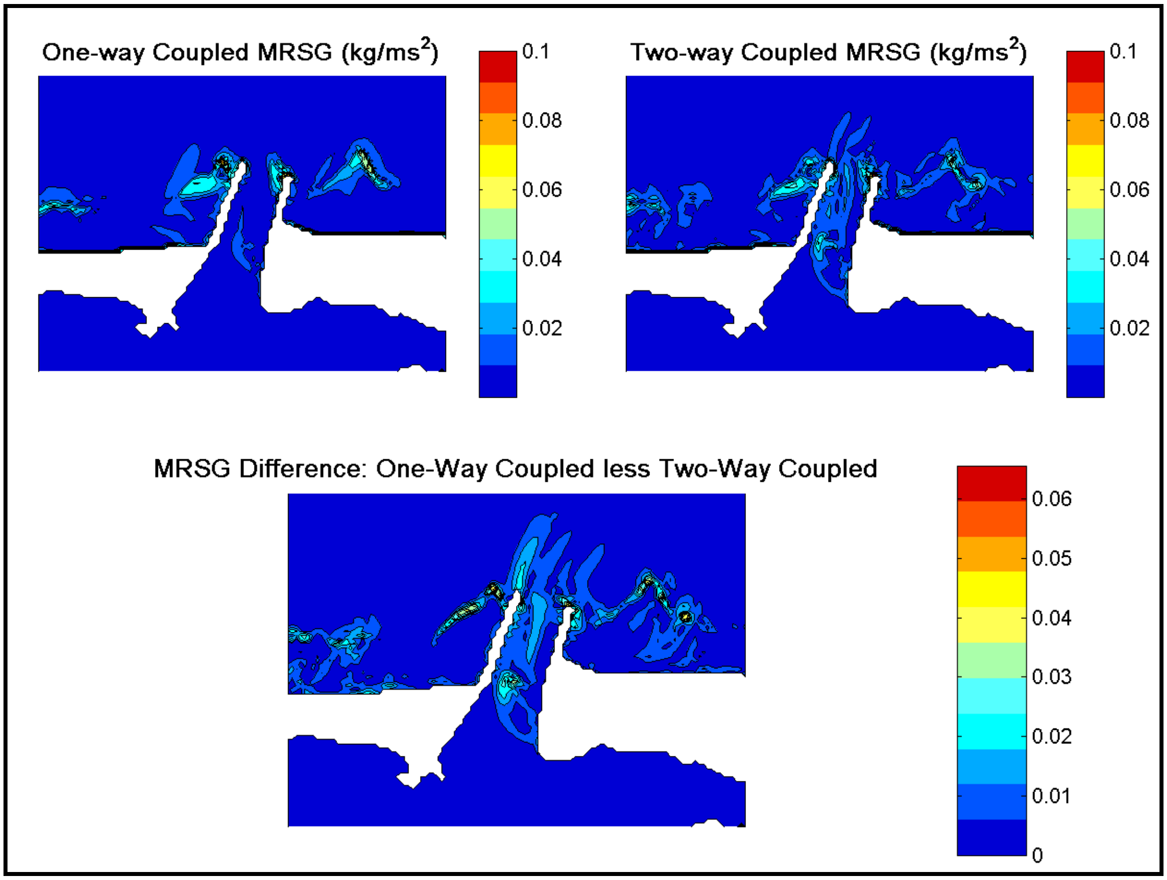

Figure 8.57. Comparison of the magnitude of radiation stress gradient fields generated by model runs 3Co (upper left panel) and 3Ct (upper right panel) near peak ebb tide. The lower panel represents the magnitude of the vector difference between the two radiation stress gradient fields.

8.4.2. <u>Model Dependence on Wave Spectra, Direction A</u>

8.4.2.1. <u>Current Fields.</u>

Near peak ebb tide, small waves from direction A affect currents in much the same way that small waves from direction C did. Current fields 1Co and 1Ao (Figure 8.47 and Figure 8.58) share all key current features and differences from the uncoupled case (Figure 8.46). In both 1Co and 1Ao cases, there is a narrowing of the ebb jet between the jetty tips when compared to the uncoupled case. Both share a small net onshore current along the inside of the north jetty where the uncoupled case shows a net offshore current. The highest currents (2.2 m/s) occur in the navigation channel where currents average 1.4 m/s. The 1At case (Figure 8.59) shares all of the features of the 1Ao case, but the current rates are slightly more. Maximum current rate (2.3 m/s) occurred in the navigation channel where the mean current rate was 1.4 m/s. In the two-way coupled case, the ebb jet was deflected northward offshore of the entrance more than in the one-way coupled case (Figure 8.60). One-way coupled solutions showed a slightly wider (~50 m) current stream in the channel.

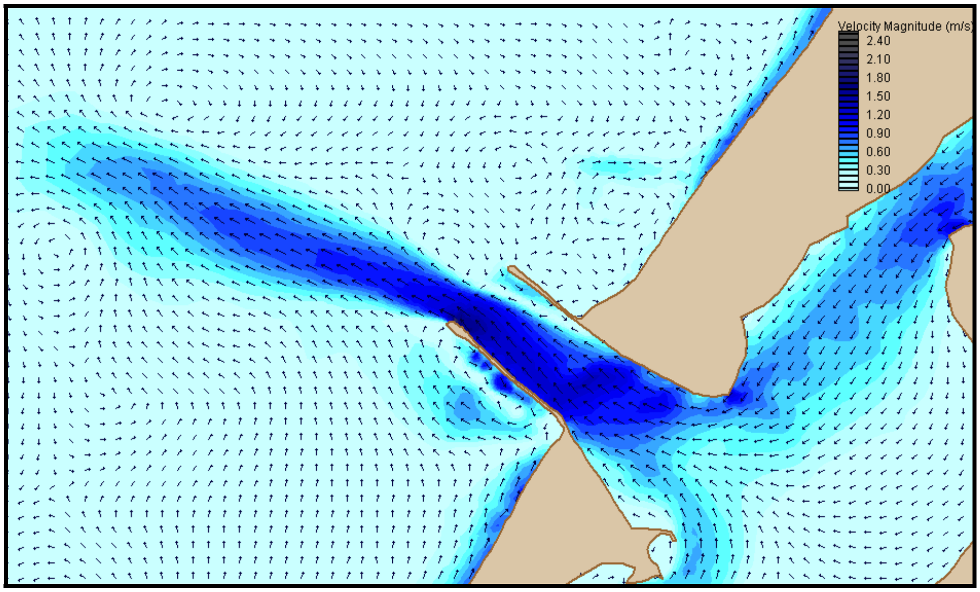

Figure 8.58. Typical velocity magnitude field for the 1Ao model run near peak ebb tide.

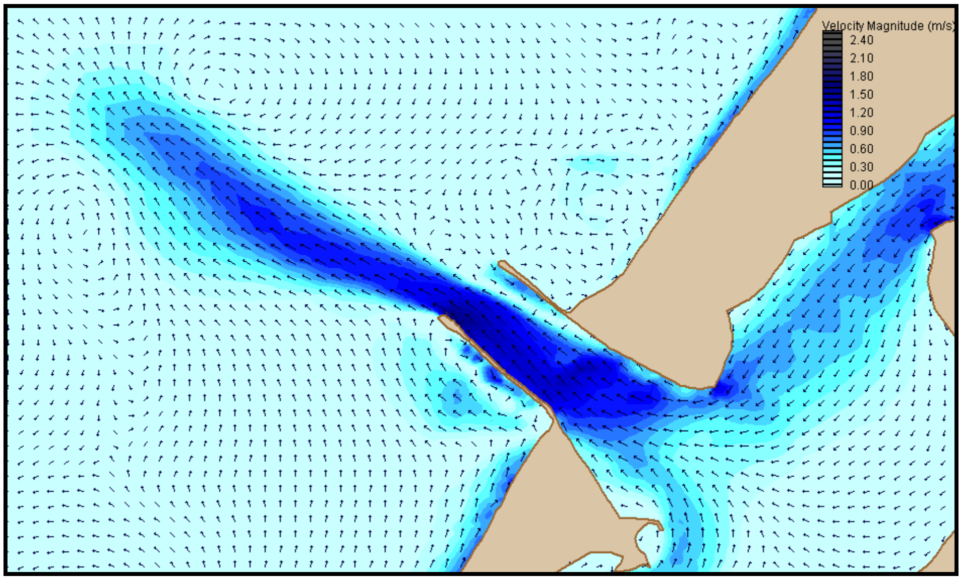

Figure 8.59. Typical velocity magnitude field for the 1At model run near peak ebb tide.

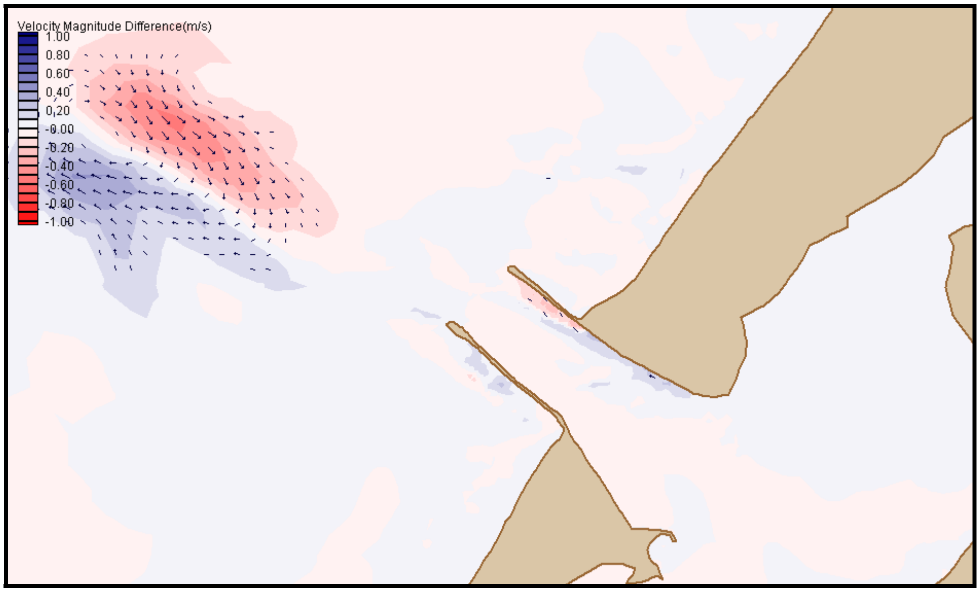

Figure 8.60. Difference in velocity magnitudes between 1Ao and 1At model cases near peak ebb tide. The two-way coupled magnitudes were subtracted from the one-way values.

Unlike in the small wave case, current fields for the high-energy input spectra (cases 3Ao and 3At) show similarity in current distribution only to each other. For the

3Co model run (Figure 8.61), ebbing currents are concentrated in the navigation channel and peak there at 2.1 m/s. Mean ebb current in the navigation channel is 1.8 m/s in this case. Along the inside of the north jetty, currents are directed into the bay and reach 1.9 m/s. Offshore the ebb jet is deflected northward over the Humboldt Bar when compared to the uncoupled case. For the 3At model case (

Figure 8.62) current patterns are much the same within the entrance, although slightly higher in the navigation channel (2.3 m/s peak and 1.9 m/s mean). Onshore currents along the inside of the north jetty in the two-way coupled case are typically 0.1 m/s less than in the one way case. Current in the 3At case over the channel shoal is also less than in the 3Ao case. The largest differences between the one-way and two-way coupled cases were seen outside the entrance, over the Humboldt Bar (Figure 8.63). In the two-way coupled case, the ebb jet is turned sharply northward at the western edge of the Humboldt Bar, while in the one-way coupled case, the deflection is much less.

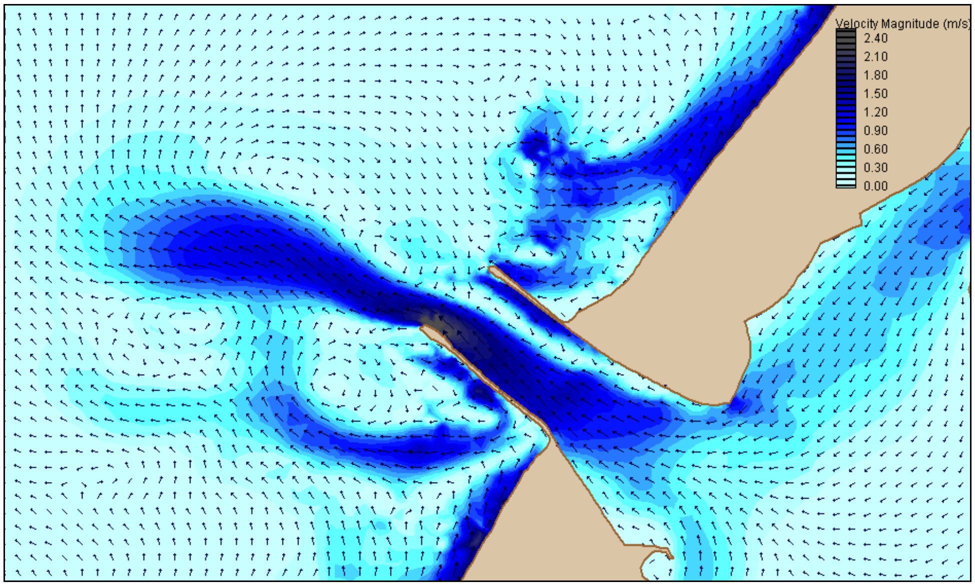

Figure 8.61. Typical velocity magnitude field for the 3Ao model run near peak ebb tide.

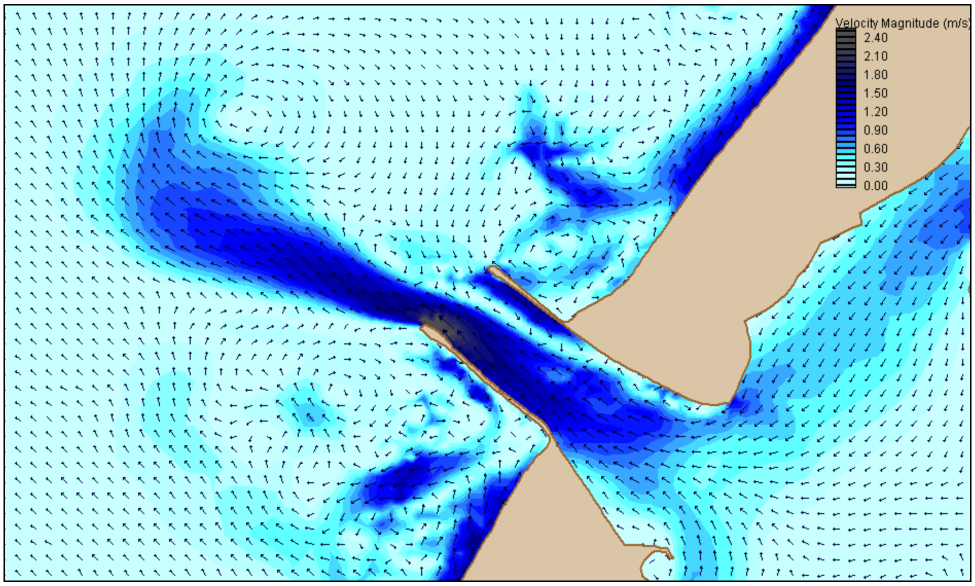

Figure 8.62 Typical velocity magnitude field for the 3At model run near peak ebb tide.

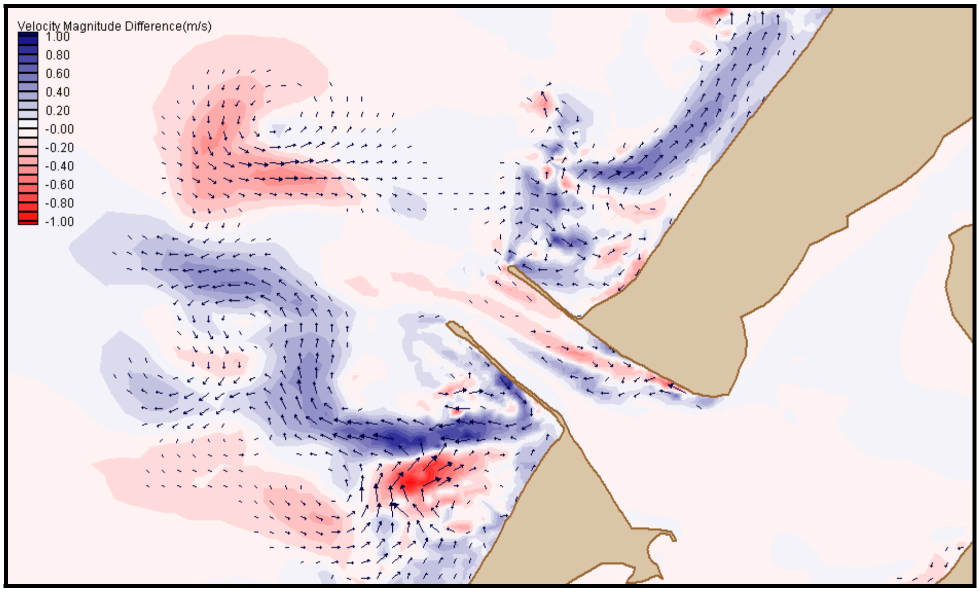

Figure 8.63. Difference in velocity magnitudes between 3Ao and 3At model cases near peak ebb tide. The two-way coupled magnitudes were subtracted from the one-way values.

8.4.2.2. Wave Height Fields.

Wave height fields for direction A waves near ebb tide show the same results as those from direction C waves. All three wave conditions showed significant differences in wave height between one-way coupled and two-way coupled solutions. In every case, the two-way coupled model predicted significantly higher waves in the navigation channel, over the channel shoal, and in the Entrance Bay than the one-way model. For the 1Ao and 1At cases (Figure 8.64), difference in wave height in the navigation channel averaged 0.35 m with a peak of 0.6 m over the channel shoal. For the 3Ao and 3At cases (Figure 8.65), the peak difference in wave height in the navigation channel was 1.7 m and over the channel shoal the peak difference in wave height was 1.9 m. Another feature of the two-way solution for the higher energy wave spectra is an increase in wave height over the Humboldt Bar that is absent from the one-way case.

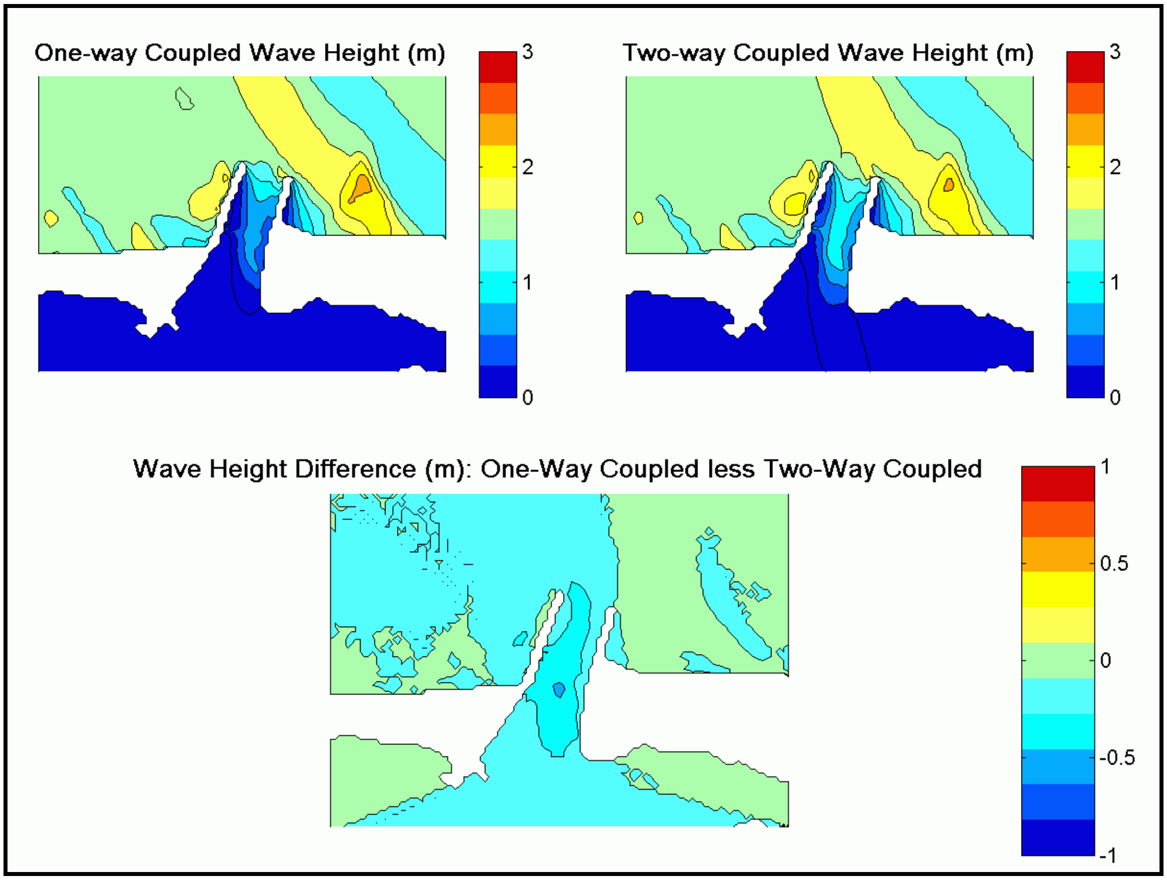

Figure 8.64. Comparison of wave height fields for model runs 1Ao and 1At. Two-way coupled solutions were up to 0.6 m higher over the channel shoal and up to 0.5 m higher in the navigation channel than one-way coupled solutions.

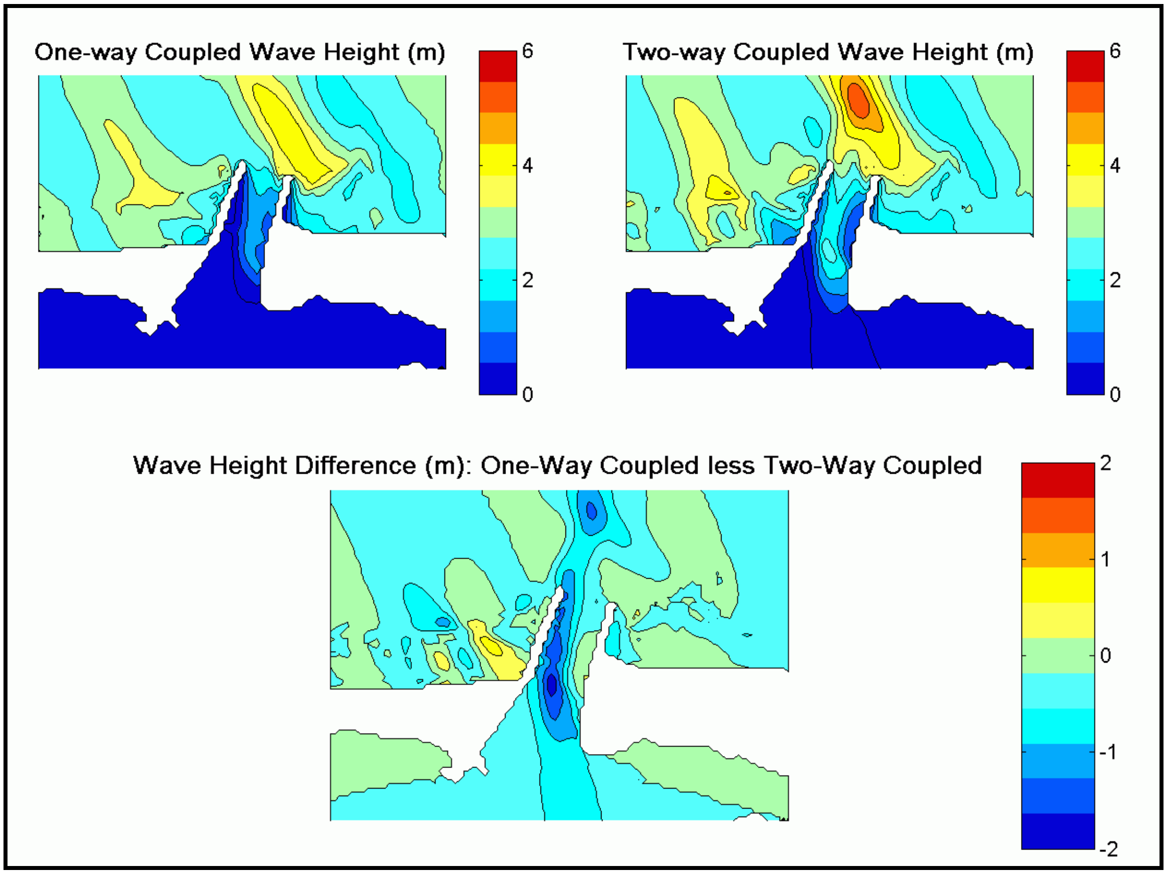

Figure 8.65. Comparison of wave height fields for model runs 3Ao and 3At. Two-way coupled solutions were up to 1.9 m higher over the channel shoal and up to 1.7 m higher in the navigation channel than one-way coupled solutions.

8.4.2.3. Radiation Stress Gradient Fields.

Radiation stress gradients for direction A waves near ebb tide showed the greatest sensitivity to coupling mode over the channel shoal for every input energy case. For the 1Ao and 1At cases (Figure 8.66), the MRSG values were similar over the whole entrance, differing only over the channel shoal and at the tip of the north jetty. Differences at each place were less in magnitude than those in the direction C cases, peaking at 1.9×10^{-4} kg/ms^2. Interestingly, there were no appreciable differences in calculated MRSG in the navigation channel as seen in the 1Co and 1Ct cases (Figure 8.56). For the 3Ao and 3At cases (Figure 8.67), there are differences in calculated radiation stress gradient magnitudes in the navigation channel, over the channel shoal, near the tip of the north jetty, and over the Humboldt Bar. Except at the tip of the north jetty, the two-way coupled model predicts higher radiation stress gradient magnitudes. The difference in MRSG between cases follows much the same pattern as the differences in predicted wave height (Figure 8.65). Note that the two-way coupled model shows higher radiation stress gradient magnitudes and larger waves at the same places over the Humboldt Bar, in the navigation channel, and over the channel shoal. Over the Humboldt Bar the increased radiation stresses are also related to the sharp northward bend in the ebb jet (

Figure 8.62). Again the magnitude of the radiation stress gradients was four times greater on average for the high-energy case over the lower energy case.

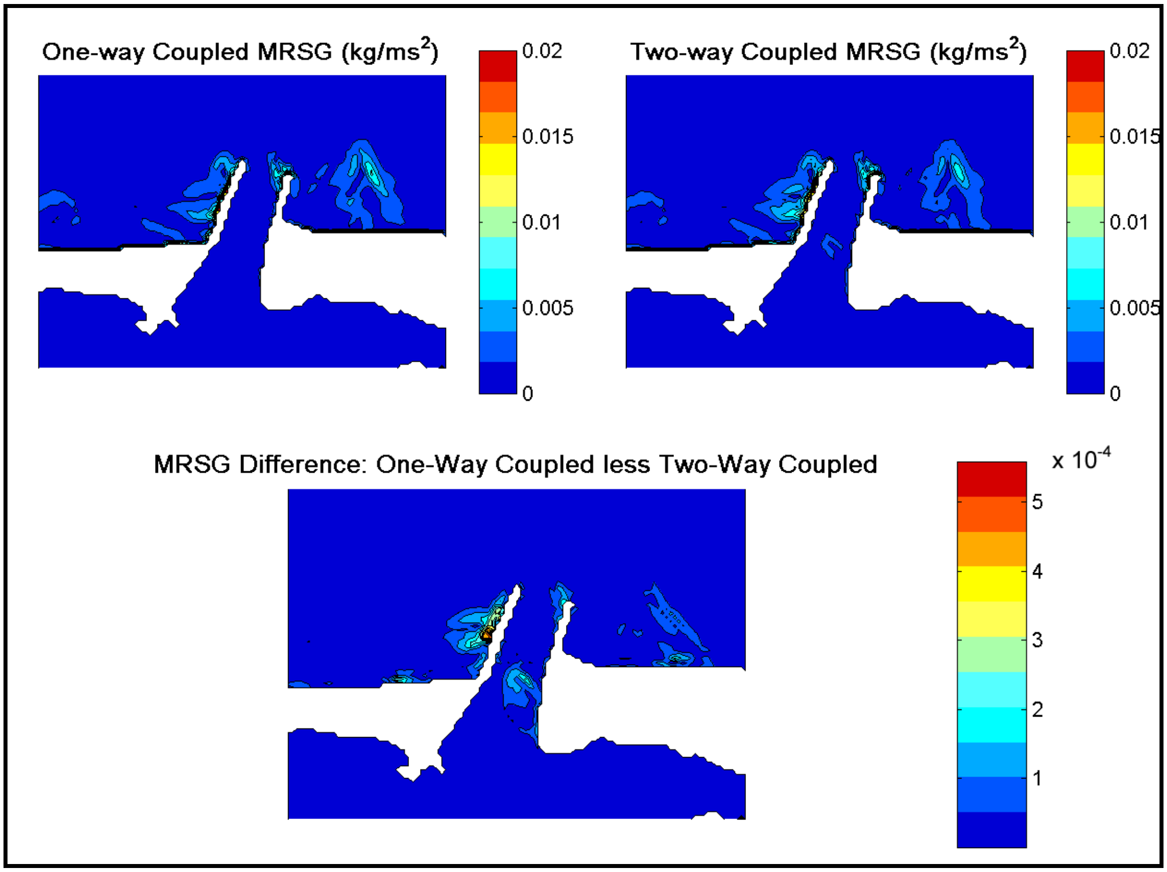

Figure 8.66. Comparison of the magnitude of radiation stress gradient fields generated by model runs 1Ao (upper left panel) and 1At (upper right panel) near peak ebb tide. The lower panel represents the magnitude of the vector difference between the two radiation stress gradient fields.

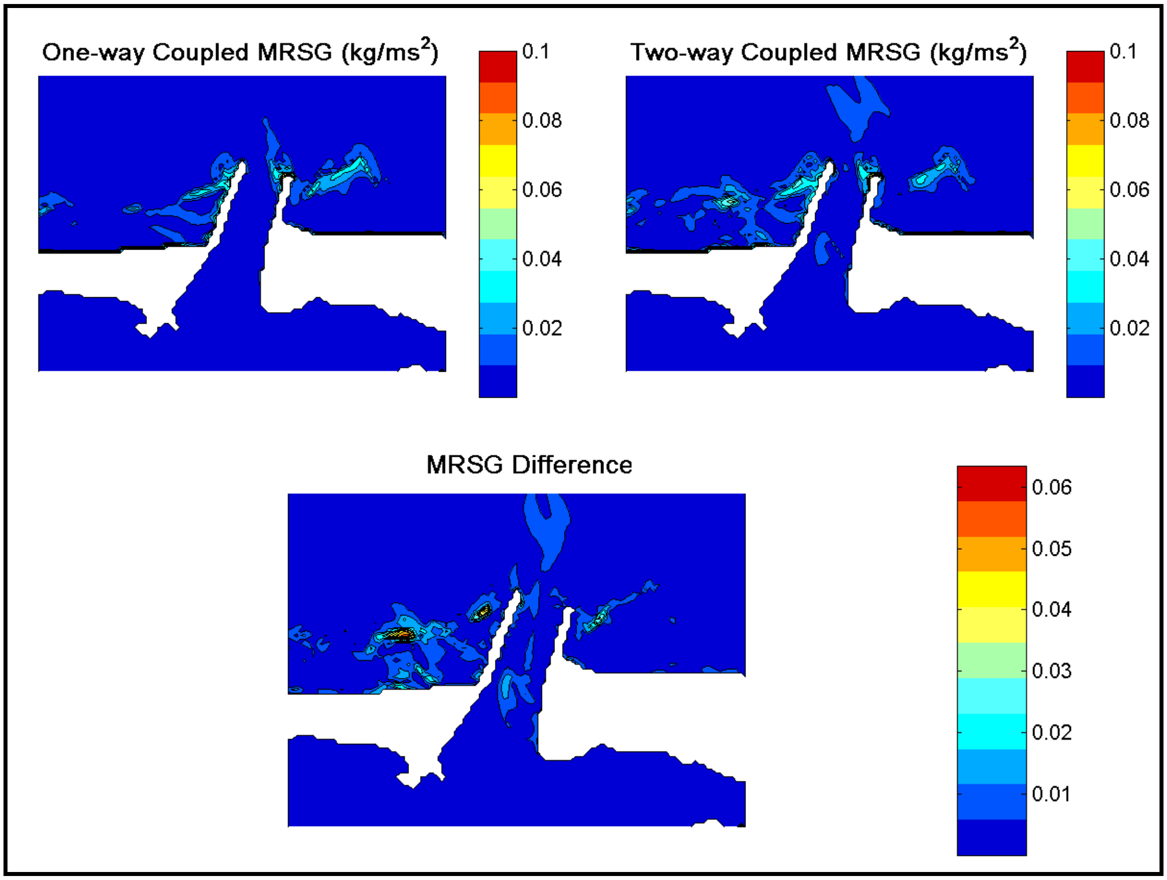

Figure 8.67. Comparison of the magnitude of radiation stress gradient fields generated by model runs 3Ao (upper left panel) and 3At (upper right panel) near peak ebb tide. The lower panel represents the magnitude of the vector difference between the two radiation stress gradient fields.

8.4.3. Model Dependence on Dominant Direction of Input Wave Spectra Near Peak Ebb Tide

It was expected that the one-way and two-way coupled model solutions would be most sensitive to wave direction at peak ebb tide. A very clear effect of wave direction was observed on the direction and size of the ebb jet. For the two-way coupled case, the effect was muted by wave-current interaction, whereas, in the one-way coupled model case, the unchanging wave field generated larger currents in certain key locations.

8.4.3.1. Direction Characteristics for Small Waves.

For the lowest energy input spectra cases, waves were not big enough to drastically change the current fields at peak ebb tide in either coupled case. As was the case for flood tide, the two-way coupled model showed a greater sensitivity to changes in wave direction in comparison to the one-way coupled model.

Current fields showed a mean difference within the entrance of 0.05 and 0.1 m/s between cases 1Co and 1Bo and cases 1Co and 1Ao respectively. Two-way coupled differences were 0.1 (1Bt vs. 1Ct) and 0.1 m/s (1Ct vs. 1At) for the same area.

Differences in predicted wave heights for each input spectra highlight the complex nature of the wave-current interaction at Humboldt. For both coupled model cases, more wave energy enters the bay as the dominant direction of the input spectra is changed from direction A to direction C. Predicted wave height increases by an average of 0.5 m over the entrance between 1Ao and 1Co wave cases. From the 1At to 1Ct cases the increase in wave height over the whole entrance averaged 0.4 m.

8.4.3.2. Direction Characteristics for Large Waves.

In much the same way as with flooding tides, high-energy waves highlight differences in coupled model behavior near peak ebb tide. Differences in current velocity and wave height distribution based on wave direction were more pronounced at ebb tide in the one-way coupled version of the model than in the two-way coupled version.

Current fields showed that the one-way coupled model predicted current velocities that differ by an average of 0.3 m/s (peak difference was 2.4 m/s) between cases 3Co and 3Ao in the navigation channel. For the two-way coupled model, differences between navigation channel currents predicted for 3Ct and 3At wave cases were less than 1.3 m/s and less than 0.7 m/s respectively.

Wave height sensitivity to wave direction was also measured for each coupling case. For the 3Ao case, the solution averages 0.7 m (rms) less than the 3Co case over the navigation channel. For the two-way coupled model, wave heights in the navigation channel increase by 1.6 m as the input wave direction changes from direction A to direction C. Overall wave heights are greater for the two-way coupled solutions than for the one-way coupled solutions in every case.

8.5. Comparison Along Transects

Given the potential complexity associated with the non-linear interaction between waves and tides, we also chose to compare time series from different models at fixed locations. In particular, time series data were examined at specific nodes along three distinct cross-channel transects (Figure 8.68). Wave height and current velocities were extracted at these points for each of the cases presented above. One and two-way coupled model solutions and differences are plotted as time series for the five nodes nearest the navigation channel for each transect.

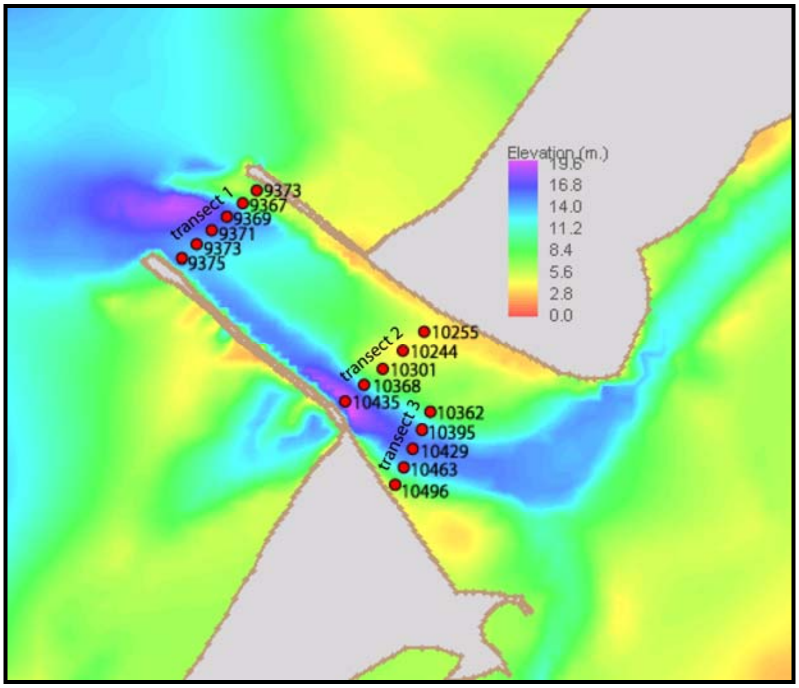

Figure 8.68. Transect nodes along with associated ADCIRC node numbers.

8.5.1. <u>Current Comparison Along Transects</u>

Under the highest energy wave spectra, differences in wave heights and currents were observed at transect nodes for all tide stages. Further differences are brought to light with the time series plots. At both transect 1 and transect 2, for a fixed offshore wave direction, current differences were greater between coupling cases for the first 12 hours of observation or so and much less different beyond that (e.g., Figure 8.69 and Figure 8.70). In addition, there were substantial phase differences in the first part of the day but they disappear in the second half. In order to determine whether or not these results were a consequence of the coupled models still approaching a stable solution, model runs 3Co and 3Ct were extended out an additional day. The same results were observed: larger model differences earlier in the day and smaller differences later in the day. The variations were attributed to the mixed tides at Humboldt Bay. In these model runs, HHW and LLW were observed in the early part of the day, with LHW and HLW occurring later.

At transect 1, for cases 3Co and 3Ct, the peak difference in velocity was 2.43 m/s with a mean rms difference across all nodes of 0.67 m/s. For transect 2 (Figure 8.69), the peak difference was 2.11 m/s and the mean rms difference was 0.63 m/s. Over the second half of the observation day, the peak difference between velocities along transect 1 was reduced to 0.21 m/s and the peak difference at transect 2 (Figure 8.70) was reduced to 0.24 m/s. Mean rms differences for the last twelve hours were also reduced to 0.09 m/s and 0.11 m/s for transect 1 and transect 2 respectively. Further back in the entrance, at transect 3 (Figure 8.71 and Figure 8.72), the peak velocity difference was 0.09 m/s with the mean rms difference of 0.04 m/s.

Differences in velocities predicted in cases 3Ao and 3At were larger than for the 3Co / 3Ct comparisons. Direction A waves showed the same phase lag issues that the direction C waves did for the first twelve hours of observation at transect 1 and transect 2 nodes. For transect 1 the peak difference in velocity was 2.35 m/s with a mean rms difference of 0.73 m/s. For transect 2 nodes, the peak difference was 2.22 m/s with a mean rms difference of 0.71 m/s. For the second half of the observation period the peak values were reduced to 0.45 m/s and 0.37 m/s for transect 1 and transect 2. Mean rms differences were reduced to 0.23 m/s and 0.19 m/s respectively also. For transect 3, the peak velocity difference was 0.46 m/s with a mean rms difference of 0.10 m/s.

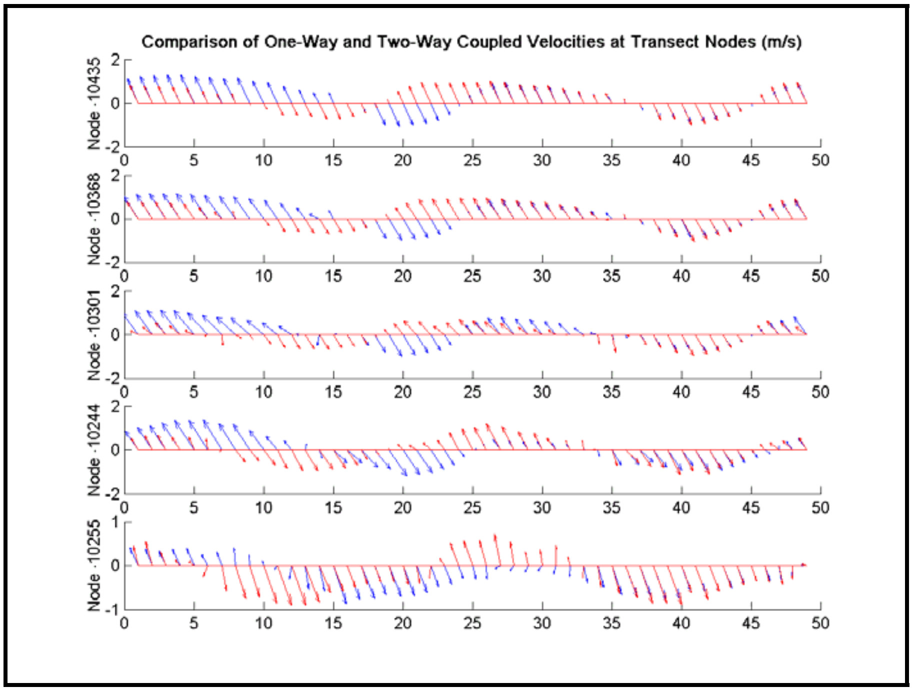

Figure 8.69. Transect 2: Comparison of semi-hourly vector velocities between 3Co (blue) and 3Ct (red) vector velocities along transect nodes. Numbers along the x-axis denote semi-hourly time steps. The y-axis scale is in m/s.

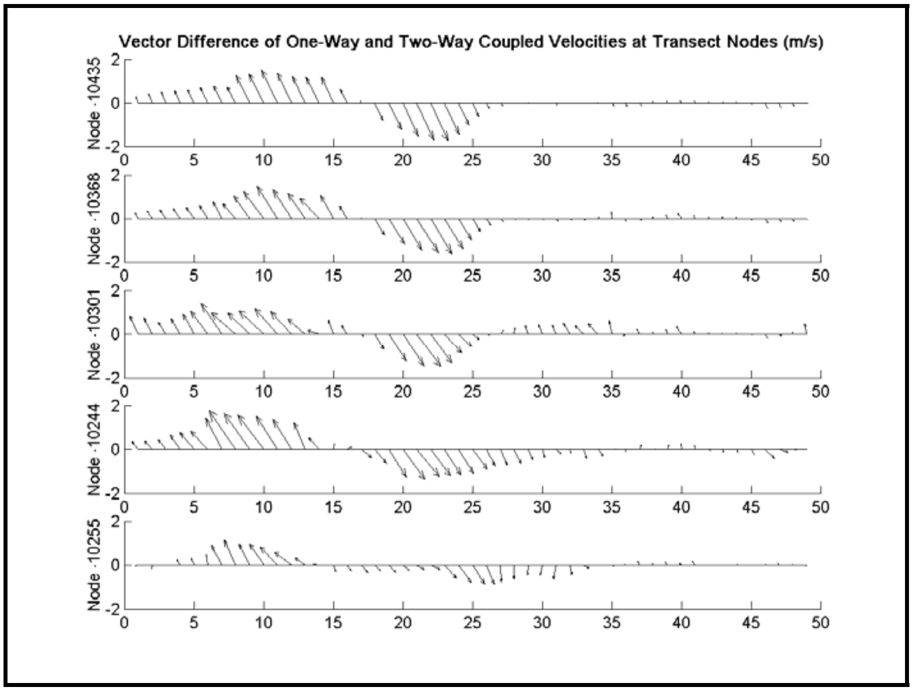

Figure 8.70. Transect 2: Semi-hourly vector difference between one-way and two-way coupled model velocities as shown in Figure 8.69. Note the largest differences occur early in the observation period relative to later. Numbers along the x-axis denote semi-hourly time steps. The y-axis scale is in m/s.

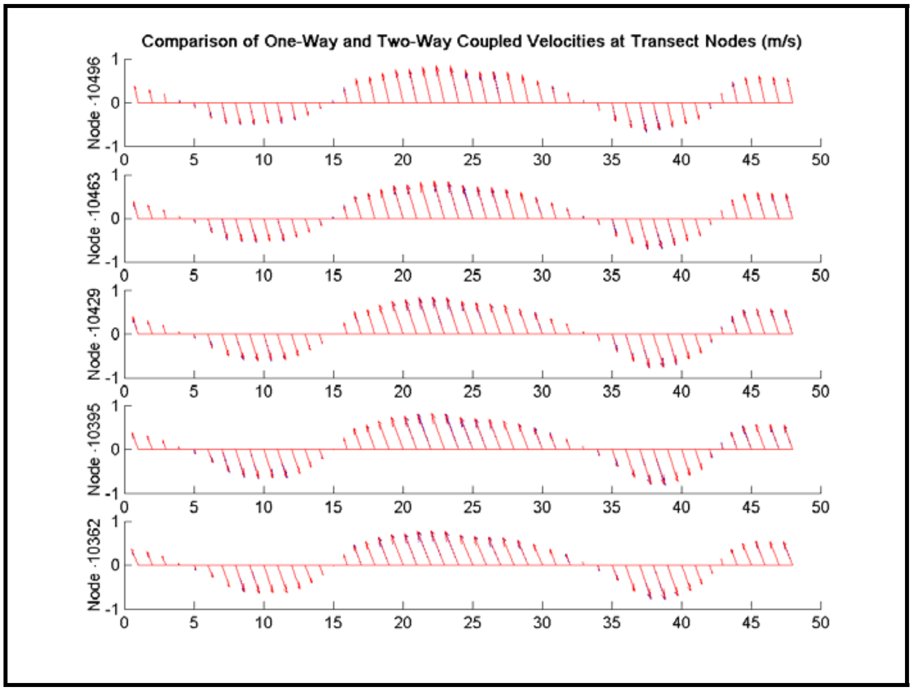

Figure 8.71. Transect 3: Comparison of semi-hourly vector velocities between 3Co (blue) and 3Ct (red) vector velocities along transect nodes. Numbers along the x-axis denote semi-hourly time steps. The y-axis scale is in m/s.

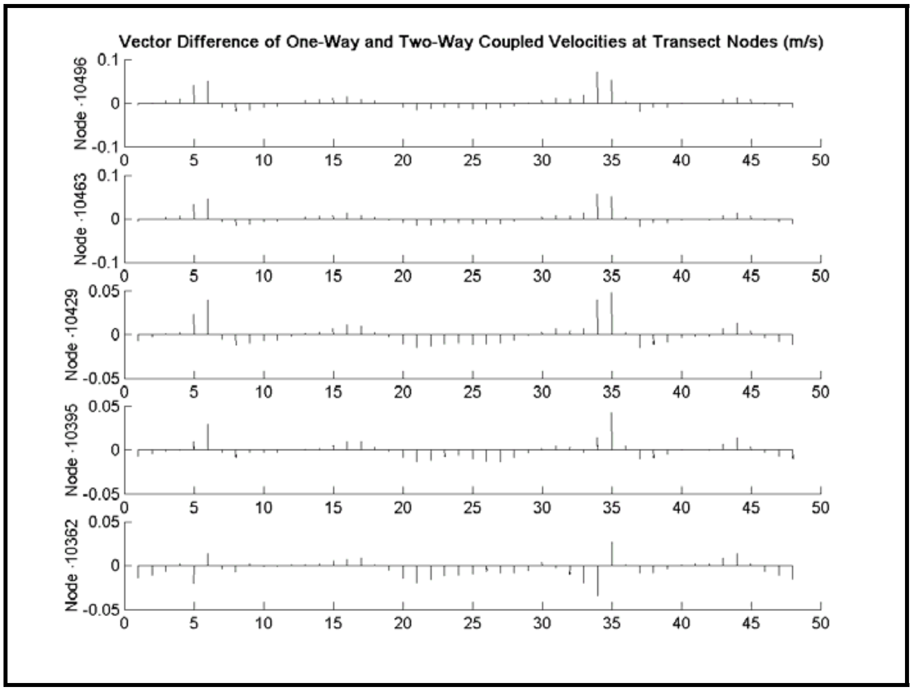

Figure 8.72. Transect 3: Semi-hourly vector difference for vectors shown in Figure 8.71. Note the spikes at 5 and 35, near high tide. Numbers along the x-axis denote semi-hourly time steps. The y-axis scale is in m/s.

Unlike the highest energy wave cases, the moderate energy wave cases did not show a significant phase lag between one-way and two-way coupled solutions. At transect 1 and transect 2, currents for the 2Co and 2Ct cases are nearly in phase. Differences between one-way and two-way solutions manifest themselves as spatial variance rather than as a temporal shift. A good example is shown in Figure 8.73 between nodes 10301 and 10244. When one-way coupled velocities are greater at node 10301, two-way coupled velocities are greater at node 10244 by about the same magnitude and direction. In fact the differences between one-way and two-way coupled solutions for the 2Co and 2Ct wave cases occurred primarily on the north side of the channel in the shoal area. For transect 3, which consists of tightly spaced nodes confined to the navigation channel, the differences in current velocity between one-way and two-way coupled solutions were reduced compared with results from transect 2. Note that currents differ primarily at ebb tide with one-way coupled velocities greater than two-way coupled velocities by 0.17 to 0.20 m/s at every node in the navigation channel.

For moderate (case 2) waves from direction C, the peak difference at transect 1 between one-way and two-way coupled solutions was 1.10 m/s and occurred late in the morning ebb tide. Mean rms difference over the day was 0.41 m/s. Along transect 2 (Figure 8.73 and Figure 8.74), the peak difference between one-way and two-way runs occurred late in the morning ebb tide and was 0.93 m/s. Mean rms difference was 0.31 m/s. Along transect 3 (Figure 8.75 and Figure 8.76), the peak difference was 0.19 m/s with a mean rms difference of 0.07 m/s.

For direction A waves with moderate (case 2) wave spectra, the results were very similar. Peak differences in velocity occurred late in ebb tide and were 9 to 12% larger than in the direction C case. Mean rms differences were much the same as in the direction C case.

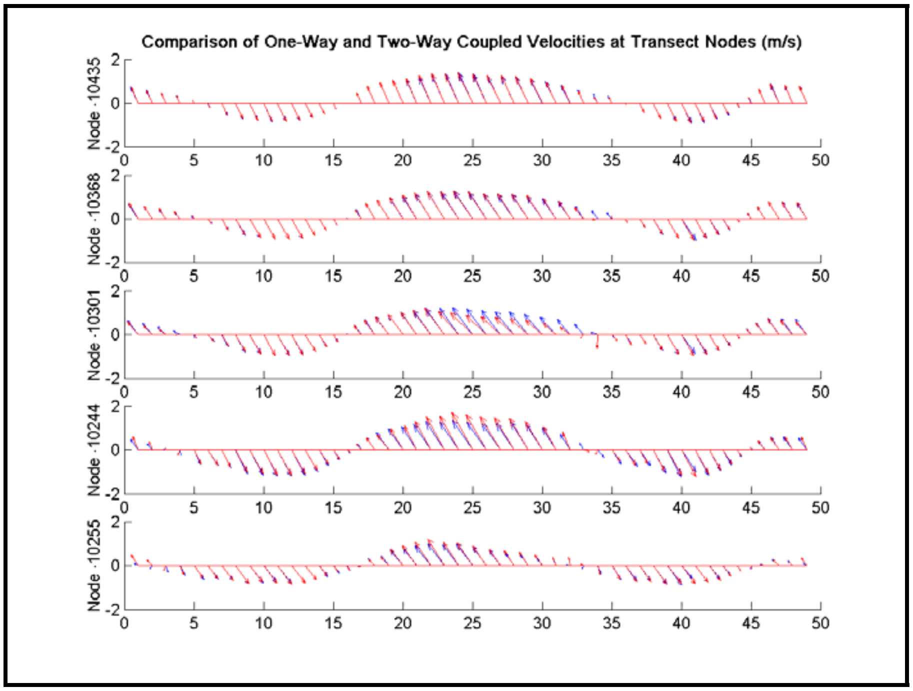

Figure 8.73. Transect 2: Comparison of semi-hourly vector velocities between 2Co (blue) and 2Ct (red) vector velocities along transect nodes. Numbers along the x-axis denote semi-hourly time steps. The y-axis scale is in m/s.

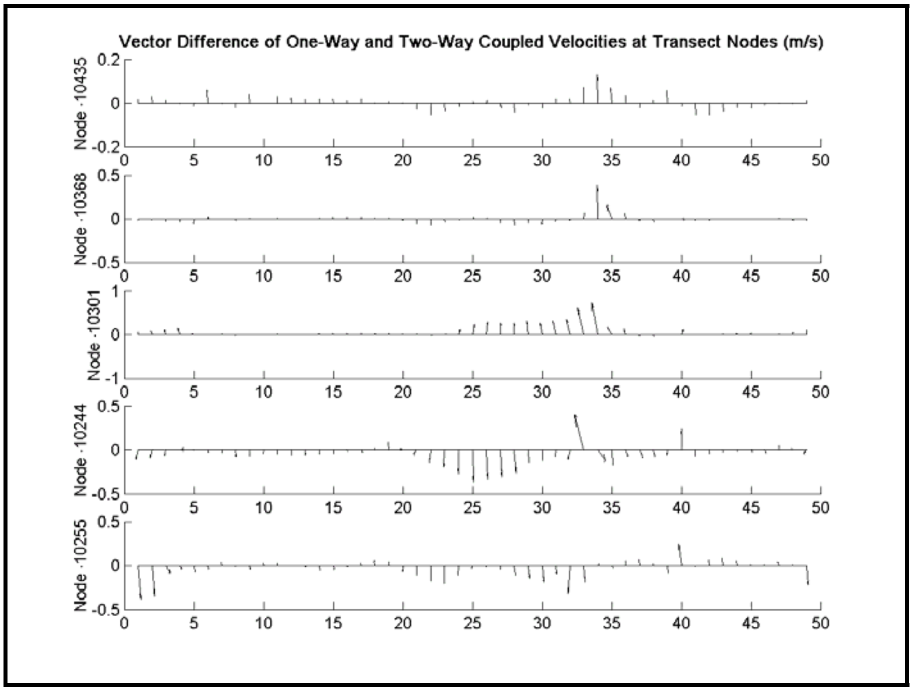

Figure 8.74. Transect 2: Semi-hourly vector difference for vectors shown in Figure 8.73. Differences in this case occur primarily at ebb tide. Numbers along the x-axis denote semi-hourly time steps. The y-axis scale is in m/s.

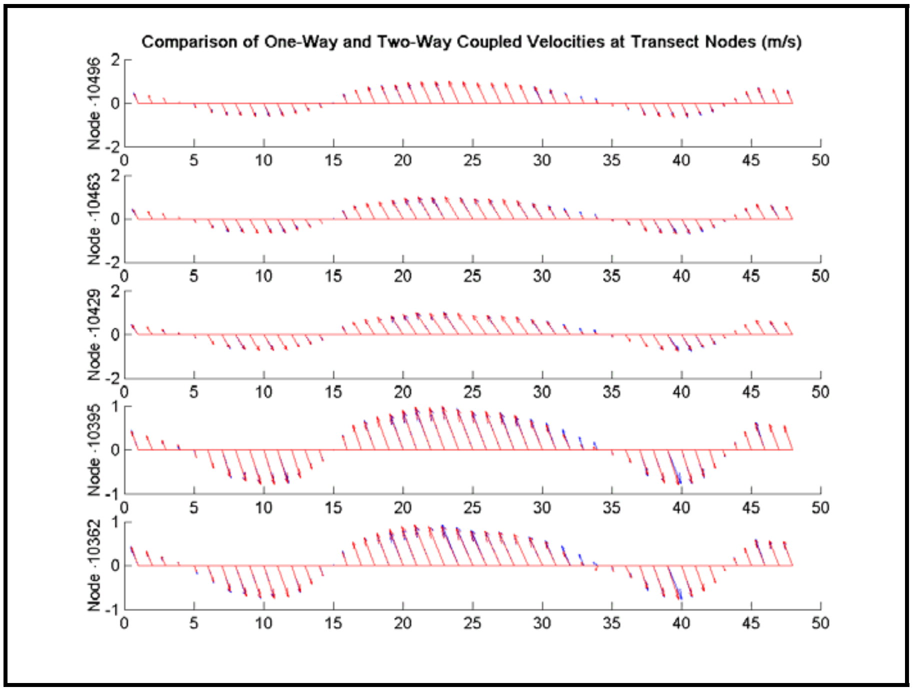

Figure 8.75. Transect 3: Comparison of semi-hourly vector velocities between 2Co (blue) and 2Ct (red) vector velocities along transect nodes. Numbers along the x-axis denote semi-hourly time steps. The y-axis scale is in m/s.

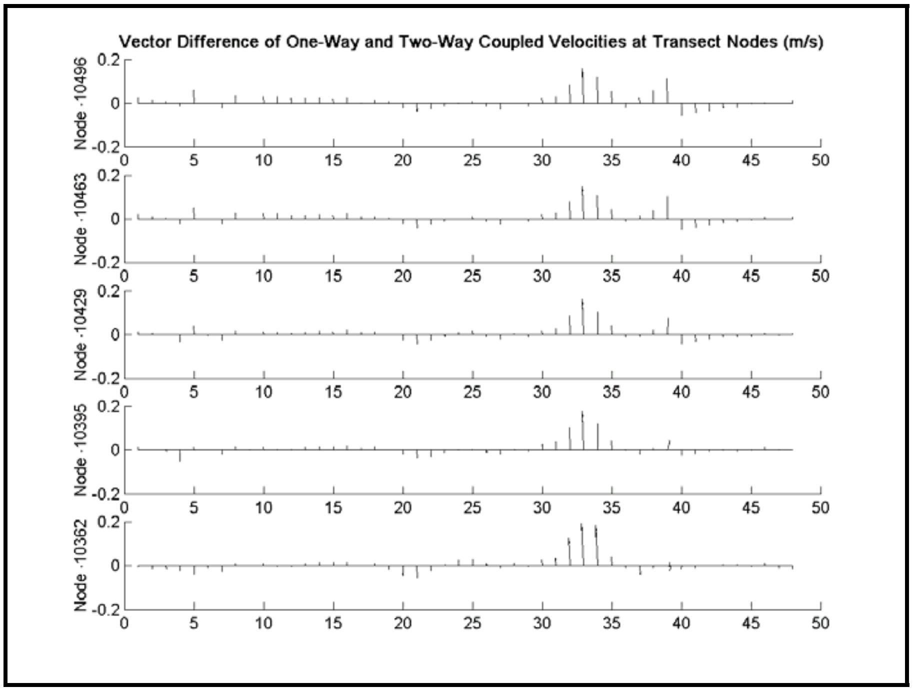

Figure 8.76. Transect 3: Semi-hourly vector difference for vectors shown in Figure 8.75. Differences in this case occur primarily at ebb tide. Numbers along the x-axis denote semi-hourly time steps. The y-axis scale is in m/s.

For 1Co and 1Ct wave cases, differences in current velocity at transect nodes were not as significant as in the 2Co and 2Ct cases. Primarily the differences that did occur were in the northern fifth of the entrance where the smaller waves shoal. In the navigation channel there were no significant differences in current velocity. Maximum observed difference between one-way and two-way coupled solutions was 0.19 m/s in the navigation channel and 0.21 m/s in the shoaling areas. Mean rms differences were between 0.08 m/s and 0.12 m/s for all wave directions. Differences could often be explained by spatial variation rather than phase distortion.

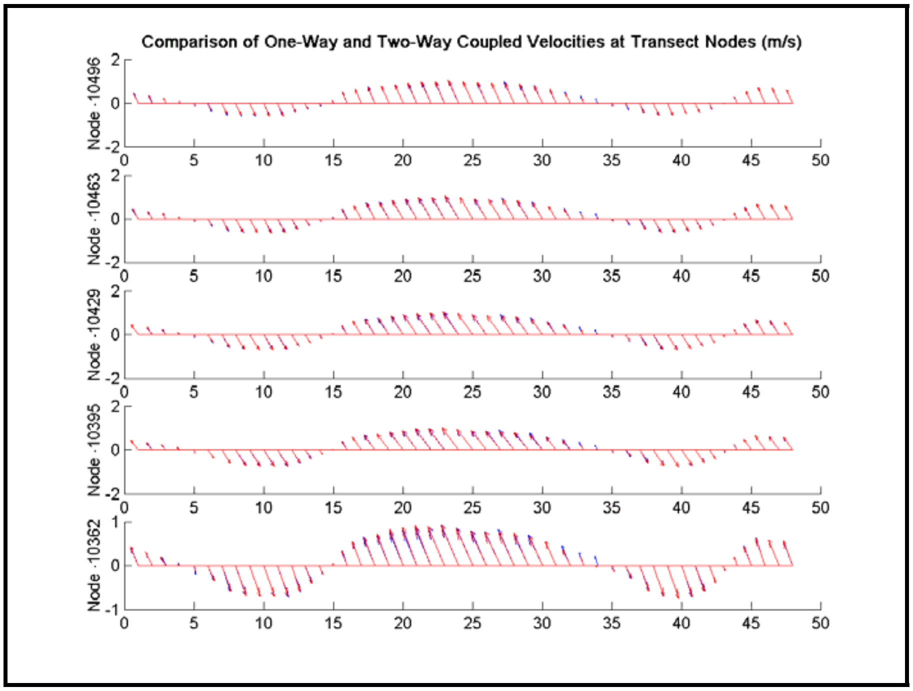

Figure 8.77. Transect 3: Comparison of semi-hourly vector velocities between 1Co (blue) and 1Ct (red) vector velocities along transect nodes. Numbers along the x-axis denote semi-hourly time steps. The y-axis scale is in m/s.

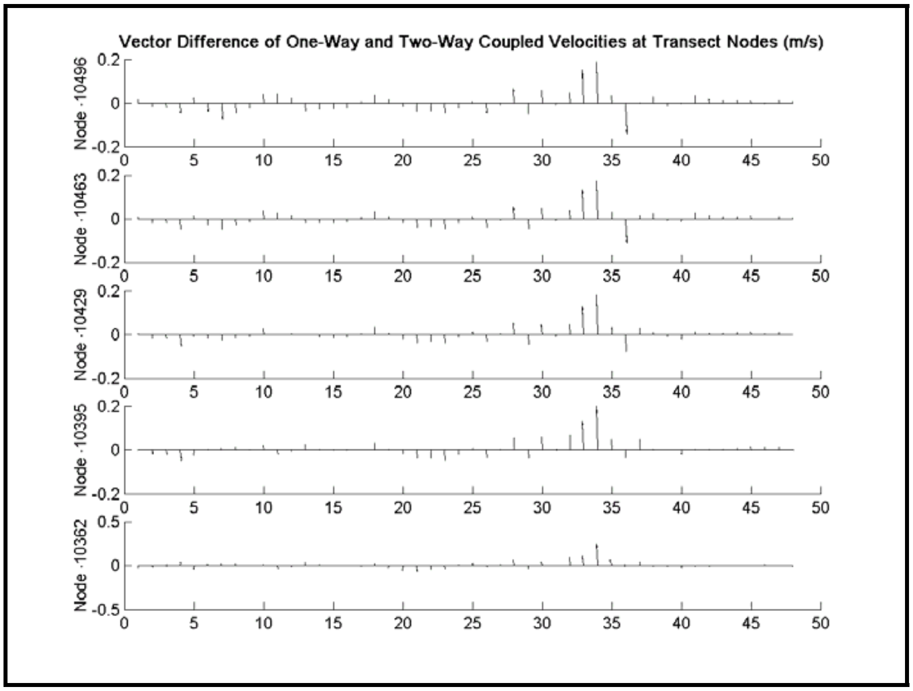

Figure 8.78. Transect 3: Semi-hourly vector difference for vectors shown in Figure 8.77. Differences in this case occur primarily at ebb tide. Numbers along the x-axis denote semi-hourly time steps. The y-axis scale is in m/s.

8.5.2. Wave Height Comparison Along Transects

Wave heights are much more sensitive to the choice of one-way or two-way coupling than current velocity. For all wave cases, there is almost no correlation between wave heights between the one-way coupled solution and two-way coupled solution (since the one-way coupled wave heights are not influenced at all by the currents). For the 1Co and 1Ct wave cases, the mean rms difference was 0.57 m at transect 2 and 0.44 m at transect 3. For the 2Co and 2Ct wave cases, the mean rms difference was 0.64 m at transect 2 and 0.42 m at transect 3. For the 3Co and 3Ct cases, the mean rms difference in wave height at transect 2 was 0.54 m, and at transect 3, 0.38 m. The smaller difference with the largest input wave energy is due to energy dissipation through breaking outside the entrance itself.

Figure 8.79 shows the time series comparison of wave heights along transect 2 for the 3Co and 3Ct model cases. From the wave height variation in the two-way coupled case, tidal stage can be inferred. Similarly Figure 8.80, shows the time series comparison of predicted wave heights along transect 2 for the 2Co and 2Ct cases. Again, tidal stage can be inferred from wave height variation. Figure 8.81 is included to show the time-series comparison in predicted wave heights for the 1Co and 1Ct model cases.

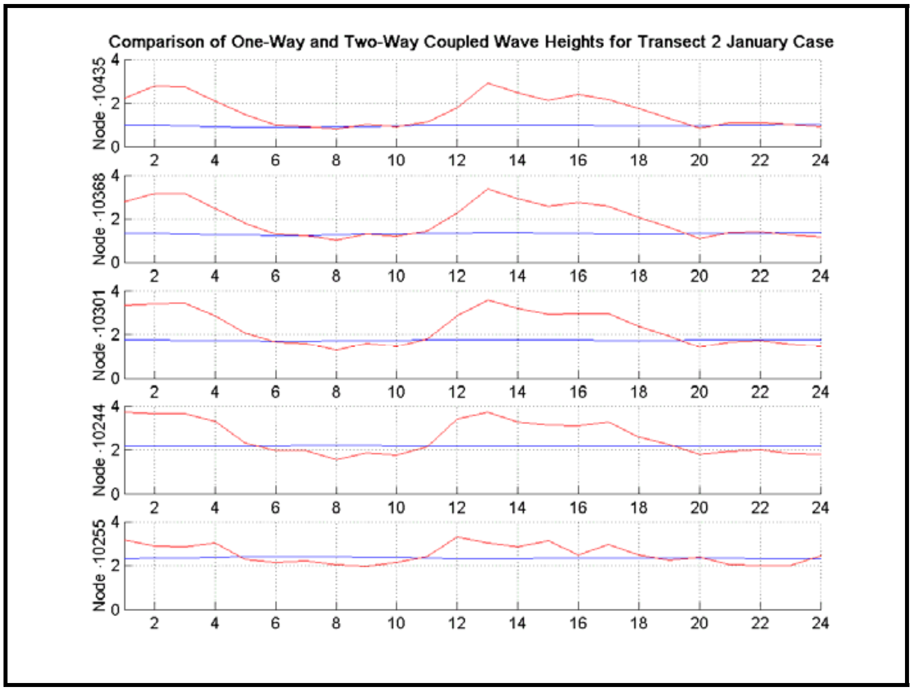

Figure 8.79. Transect 2: Hourly wave height comparison for model cases 3Co (Blue) and 3Ct (Red). Y-axis scale is wave height in m.

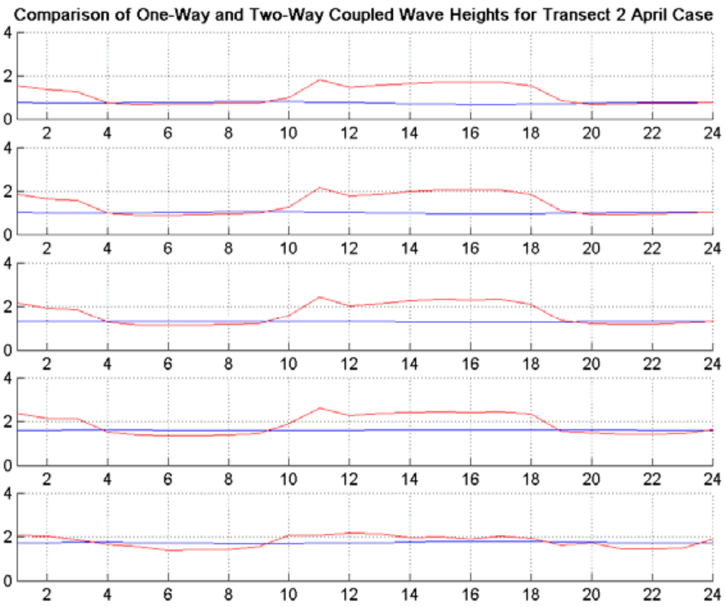

Figure 8.80. Transect 2: Hourly wave height comparison for model cases 2Co (Blue) and 2Ct (Red). Y-axis scale is wave height in m.

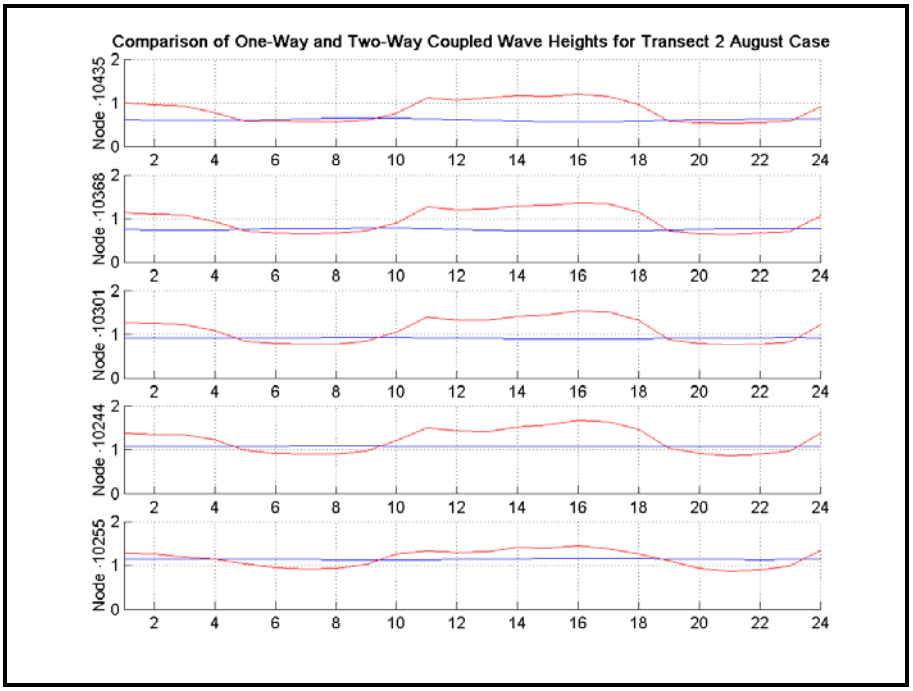

Figure 8.81. Transect 2: Hourly wave height comparison for model cases 1Co (Blue) and 1Ct (Red). Y-axis scale is wave height in m.

The impact of wave direction on model output was also examined on the basis of time series at transect nodes. Full analysis is beyond the scope of this paper, but preliminary conclusions were made. First, a significant phase lag was observed between solutions of the same coupling mode with different input wave directions. Second, wave heights show the most sensitivity to wave direction at transect 2. Third, two-way coupled solutions are slightly more dependent on wave direction than one-way solutions when it comes to phase distortion. Figure 8.82, Figure 8.83, and Figure 8.84 are included to illustrate the importance of input direction on model output.

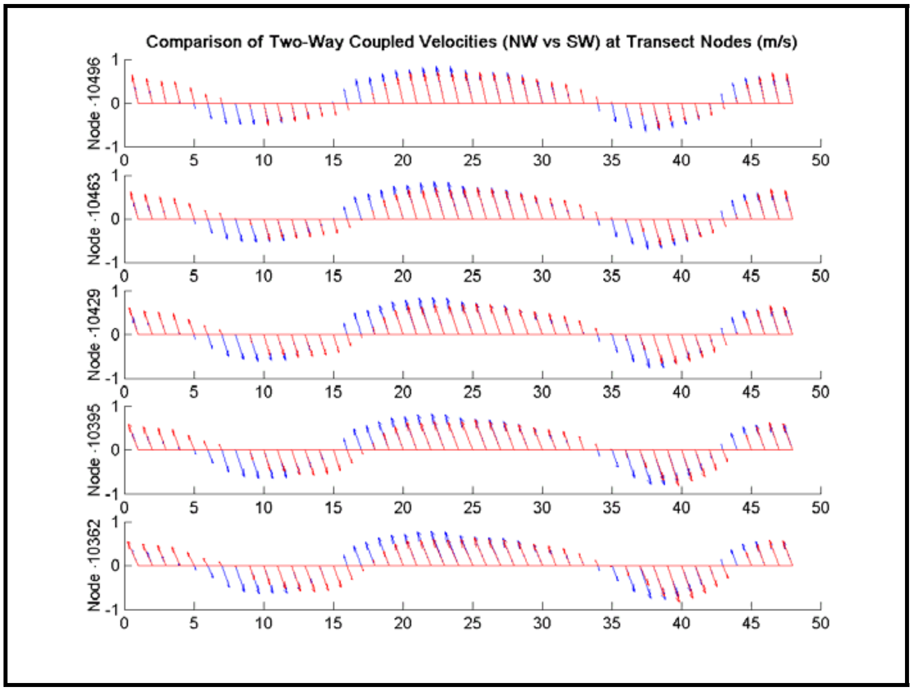

Figure 8.82. Transect 3: semi-hourly comparison of current velocities for two-way coupled model solutions for direction C (blue) and direction A (red) winter waves. Numbers along the x-axis denote semi-hourly time steps. The y-axis scale is in m/s.

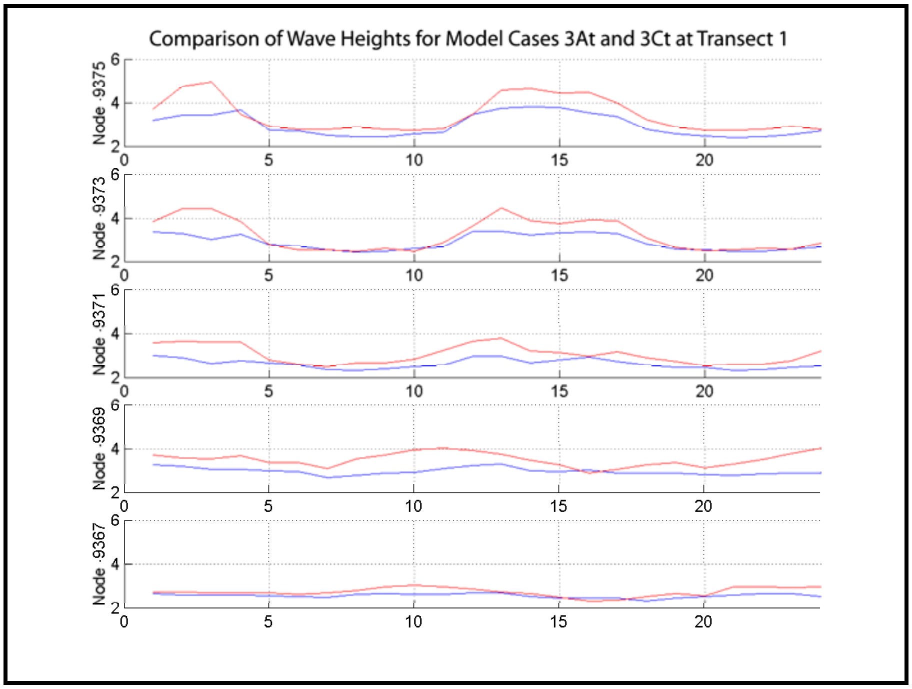

Figure 8.83. Transect 1: Hourly wave height comparison for two-way coupled model solutions direction C (blue) and direction A (red) waves. Y-axis scale is wave height in m.

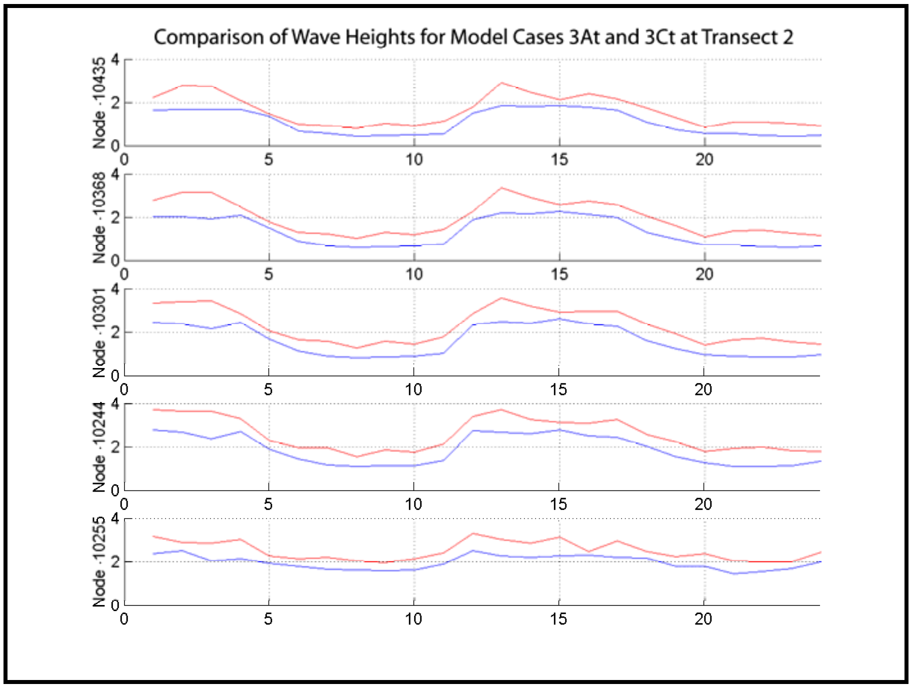

Figure 8.84. Transect 2: Hourly wave height comparison for two-way coupled model solutions direction C (blue) and direction A (red) waves. Y-axis scale is wave height in m.

9. DISCUSSION

Many different possibilities exist in modeling oceanic processes especially with the increasing sophistication of wave and current models. This paper has explored a few of the controlling variables that must be considered when choosing the most accurate model mode for a particular application. Often, the final word is not in predicted velocity, wave height, or radiation stress gradient, the three metrics used in this paper for evaluating model performance. Rather, the value of correctly predicting a current or radiation stress is in the usefulness of that prediction in modeling sediment suspension, movement and deposition. Modeling the interactive nature of the waves and currents should produce a better solution than ignoring the interaction of the currents and waves. Even though validation cases were limited in this paper, the two-way coupled model solution is taken to be the most correct solution. The question remains then, under what oceanic conditions is a one-way coupled model solution adequate, assuming that it is less computationally costly than a two-way coupled model solution? The answer to this question is supported by the comparisons made in this paper.

Each inlet modeling project has its own unique set of constraints and oceanic conditions. One must decide which model output parameters are most significant, whether wave height, current velocities, radiation stress gradient, or some other metric. Oceanographic climate factors such as dominant wave direction, significant wave height, and common storm conditions each play a role in determining which coupling mode of the models to use. Model domain and inlet geometry must factor into the decision. In the case of the Humboldt Bay region, there are a few modeling situations in which a one-way solution can be safely used, a few where test cases should be run, and a few where the two-way coupled solution is necessary (Table 9.1). More studies should be completed to confirm the applicability of these recommendations for projects dealing with the weaker wave climates of the East and Gulf coasts. Explanation of the recommendations is below.

Table 9.1. General guidelines for use of one-way or two-way coupling for a modeling project. Results include inferences from some model runs not specifically discussed above.

Indications for One-way Coupling	**Contra-indications for One-way Coupling**	**Coupling Mode Determined by Test Runs**
• Small wave climate (< 1.8 m significant height and < 9 s dominant period) • Wave directions within 10 degrees of channel alignment • Low magnitude tidal currents (< 1.0 m/s)	• Large wave climate (> 2.4 m significant height and >11 s dominant period) • Varied or oblique wave directions (directions greater than 20° away from channel alignment) • Moderate tidal currents (>1.5 m/s)	• Significant wave heights between 1.8 and 2.0 m • Dominant wave periods of 9 to 11 s. • Wave directions between 10 and 20 degrees of channel alignment

Examination of the above climatological cases showed that differences in current fields between model coupling cases increased as the wave energy increased. It should be noted that most of the time for the lowest wave conditions, one-way and two-way coupled current magnitude fields shared the same basic features. For the 1.8 m waves, the maximum difference in current velocity for all cases was 0.31 m/s. This difference occurred with direction C waves at peak ebb tide where the current rates in the navigation channel averaged 2.1 m/s for the two-way coupled case. Mean differences in current speeds were 0.08 m/s near slack tide, with the greatest disparities concentrated around bathymetric features such as the channel shoal. For both of the larger input wave cases the basic shape of the current field changed between coupling mode.

The wave-height fields were most affected by bathymetry, current velocity (for the two-way coupled model), and offshore wave direction. Wave height fields were most similar between one-way and two-way coupled models for the smallest waves at HHW. Model output for oblique waves of the A and D directions showed that the two-way coupled model predicts significantly more wave energy in an inlet for waves directed more than 17 degrees from alignment with the navigation channel. Both wave height and current fields showed significant differences in solutions between model coupling modes near bathymetric features such as the entrance to the navigation channel and the channel shoal for the larger input wave energies.

Applying the above information to the Humboldt inlet, it is clear that the two-way coupled model is required for greater accuracy under most wave conditions. As stated earlier in this paper, waves, predominantly southwesterly waves, in excess of 7 m significant wave height and 20 s dominant period occur annually. The greatest wave climatology cases discussed in this paper were less than 1/4 as energetic as some of the waves observed regularly near the Humboldt Bay entrance. The large tidal prism and narrow entrance at Humboldt combine to produce high velocity currents in and out of the mouth. The multi-basin nature of Humboldt Bay and complex bathymetric features at the inlet also contribute to the differences in output between model coupling modes.

Only twenty-four separate model cases were used to compare one-way and two-way coupled model performance. Many more test cases should also be run with this model system to better understand performance. For instance, true validation cases could not be run for the Humboldt Inlet due to lack of observed offshore wave direction data. Without a true validation case, the superiority of the two-way coupled model system over the one-way coupled model system cannot be taken for granted. More specific testing, varying only one model parameter, would provide more detailed understanding of model sensitivities. Also as computing power continues to increase, higher-resolution grids may decrease the advantage of the one-way coupled approach over the two-way coupled approach.

REFERENCES

Antunes Do Carmo, J. S. and Seabra-Santos, F. J. (2002) "Near-shore sediment dynamics computation under the combined effects of waves and currents." *Advances in Engineering Software*. **33,** 37-48.

Briggs, M., Melito, I., Demirbilek, Z., and Sargent, F. (2001). "Deep-draft entrance channels: Preliminary comparisons between field and laboratory measurements." Coastal and Hydraulics Engineering Technical Note CHETN-IX-7, U.S. Army Engineer Research and Development Center, Vicksburg, MS.

BYU-EMRL (Brigham Young University Environmental Modeling Research Laboratory). (1997). "Surface-water modeling system reference manual," Brigham Young University, Provo, UT.

Costa, S. L. (1982). "The Physical Oceanography of Humboldt Bay." in Proceedings, Humboldt Bay Symposium. (C. Toole and C. Diebel, ed.). HSU Center for Community Development.

Costa, S. L., and Glatzel, K. A. (2002). "Humboldt Bay, California, Entrance Channel, Report 1: Data Review." ERDC/CHL CR-02-1. U.S. Army Engineer Research and Development Center, Vicksburg, MS.

Dean, R. G., and Dalrymple, R. A. (1991). *Water Wave Mechanics for Engineers and Scientists*. World Scientific, River Edge, NJ.

Deigaard, R., Okayasu, A., and Frederiksen, J. H. (1998). "A note on the horizontal momentum exchange in combined waves and current." *Coastal Engineering*. **34,** 259-275.

Gates, J. H. (1986). *Night Crossings*. Pioneer Graphics, Eureka, CA.

Georgi, H. (1993). *The Physics of Waves*. Prentice Hall, New Jersey.

Hagen, S. C., Westerink, J. J., and Kolar, R. L. (2000). "One-dimensional finite element grids based on a localized truncation error analysis." *Int. J. Numer. Meth. Fluids*. **32**, 241-261.

Harris, C.K., (1999). "The importance of advection and flux divergence in the transport and redistribution of continental shelf sediment." Ph.D. Dissertation, University of Virginia.

Hasselmann, K. (1962). “On the non-linear energy transfer in a gravity-wave spectrum – Part 1.” *J. Fluid Mech.* **12**, 481-500.

Hasselmann, K. (1963a). “On the non-linear energy transfer in a gravity-wave spectrum – Part 2.” *J. Fluid Mech.* **15**, 273-281.

Hasselmann, K. (1963b). “On the non-linear energy transfer in a gravity-wave spectrum – Part 3.” *J. Fluid Mech.* **15**, 385-398.

Hasselmann, K. *et al.* (1973). “Measurements of wind-wave growth and swell decay during the Joint North Sea Wave Project (JONSWAP).” *Deutsche Hydrograph,Zeit., Erganzung-self Reihe* **A 8**, (12).

Houwman, K. T. and Van Rijn, L. C. (1999). “Technical Note: Current resistance in the coastal zone.” *Coastal Engineering*. **38,** 261-273.

Jensen, R. E. (1994). “Spectral Wave Modelling (sic) Technology.” Coastal Engineering Technical Note CETN I-58, U.S. Army Engineer Research and Development Center, Vicksburg, MS.

Jonsson, I.G., and Skovgaard, O. (1978). “Wave Refraction Across a Shearing Current.” *Proceedings of the 16th Coastal Engineering Conference*. American Society of Civil Engineers, **1**. p. 722-741.

Jonsson, I. G. (1990). “Wave-current interactions.” *The sea*. Vol. 9, Part A, B. LeMehaute and D. M. Hanes, ed., John Wiley & Sons, Inc., New York.

Kantha, L., and Clayson, C. A. (2000). *Numerical models of oceans and oceanic processes*. Academic. San Diego, CA.

King, D. B., Smith, J. M., Militello, A., Waller, T., and Stauble, D. K. (1999). “Ponce de Leon Inlet, Florida site investigation, Report 1: Selected portions of long-term measurements 1995-1997.” Technical Report CHL-99-1, U.S. Army Engineer Research and Development Center, Vicksburg, MS.

Knobloch, E., and Pierce, R. D. (1998). “On mean currents associated with traveling water waves.” *Fluid Dynamics Research.* **22,** 61-71.

Kolar, R.L., Westerink, J. J., Gray, W.G., and Luettich Jr., R. A. (1994). “Shallow water modeling in spherical coordinates: equation formulation, numerical implementation, and application.” *J. of Hydraulic Research.* **32**, 3-24

Kraus, N. C., and Seabergh, W.C. (2002). “Inlet Spits and Maintenance of Navigation Channels.” Coastal and Hydraulics Engineering Technical Note ERDC/CHL

CHETN IV-44, US Army Engineer Research and Development Center, Vicksburg, MS.

Lai, R. J., Long, S. R., and Huang, N. E. (1989). "Laboratory studies of wave-current interaction: Kinematics of the strong interaction." *J. Geophys. Res*., 97(C11), 16201-16214.

Large, W.G., and S. Pond, (1981). "Open ocean momentum flux measurements in moderate to strong winds." *J. Phys. Oceanogr*., 11, 324-336.

Le Provost, C., Genco, M. L., Lyard, F. , Vincent, P. ,and Canceil, P. (1994). "Spectroscopy of the world ocean tides form a finite element hydrodynamic model." *J. Geophys. Res.,* **99**, 24,777-24,798.

Li, Z. and Davies, A. G. (1996). "Towards Predicting Sediment Transport in Combined Wave-Current Current," *J. of Waterway, Port, Coastal and Ocean Engineering*. **122,** 157-164.

Longuett-Higgins, M.S. and Stewart, R. W. (1960). "Changes in the form of short gravity waves on long waves and tidal currents." *J. of Fluid Mech.* **8**, 565-583.

Longuett-Higgins, M.S. and Stewart, R. W. (1961). "The changes in amplitude of short gravity waves on steady non-uniform currents." *J. of Fluid Mech.* **10**, 529-549.

Longuett-Higgins, M.S. and Stewart, R. W. (1962). "Radiation stress and mass transport in gravity waves, with application to 'surf beats'." *J. of Fluid Mech.* **13**, 481-504.

Longuett-Higgins, M.S. and Stewart, R. W. (1964). Radiation stresses in water waves; a physical discussion, with applications. *Deep Sea Research*, Pergamom Press LTD, **11**, pp 529-562.

Luettich, R. A., Westerink, J. J. , and Scheffner, N. W. (1992). "ADCIRC: An advanced three-dimensional circulation model for shelves, coasts, and estuaries; Report 1, theory and methodology of ADCIRC-2DDI and ADCIRC-3DL." Technical Report DRP-92-6. U.S. Army Engineer Waterways Experiment Station. Vicksburg, MS.

Mader, C. L. (1988). *Numerical Modeling of Water Waves.*, University of California Press, Berkley.

Miche, R. (1951). "Le pouvoir reflechissant des ouvrages maritme exposes a l'action de la houle." *Annales Ponts et Chaussees* **121**, 285-319.

Miles, J. W. (1957). "On the generation of surface waves by shear currents." *J. Fluid Mech*. **3**, 185-204.

Militello, A. (1998). "Grid Development for Modeling Two-Dimensional Inlet Circulation." CETN-IV-14, U.S. Army Engineer Research and Development Center, Vicksburg, MS.

Militello, A. and A. K. Zundel. (1999). "Surface-Water Modeling system tidal constituents toolbox for ADCIRC." Coastal Engineering Technical Note CETN IV-21, U.S. Army Engineer Research and Development Center, Vicksburg, MS.

Militello, A., and Hughes, S. A. (2000). "Circulation patterns at tidal inlets with jetties." ERDC/CHL CETN-IV-29, U.S. Army Engineer Research and Development Center, Vicksburg, MS.

Mitsuyasu, H. (1968). "On the growth of the spectrum of wind-generated waves 1." *Rep. Res. Inst. Appl. Mech., Kyushu University*, **16**, 459-465.

Murray, A.B., and Reydellet, G. (2001). "A Rip Current Model Based on a Hypothesized Wave/Current Interaction." *J. of Coastal Research*. **3**, 517-530.

Nittrouer, C.A. and J.H. Kravitz, (1996). STRATAFORM: A program to study the creation and interpretation of sedimentary strata on continental margins, *Oceanography* 9, 146-152.

Pechon, P., Rivero, F., Johnson, H., Chesher, T., O'Connor, B., Tanguy, J.-M., Karambas, T., Mory, M., and Hamm, L. (1997). "Intercomparison of wave-driven current models," *Coastal Engineering*. **31,** 199-215.

Phillips, O. M. (1957). "On the generation of waves by turbulent wind." *J. Fluid Mech.* **2**, 417-445.

Pierson, W. J., Neuman, G., and James, R. W. (1955). "Observing and forecasting ocean waves by means of wave spectra and statistics." H O Pub. No. 603, U.S. Navy Hydrographic Office, Washington, D.C.

Resio, D. T. (1987). "Shallow-water waves. I: Theory." *J. Wtrway., Port,Coast., and Oc. Engrg*., ASCE, **113**(3), 264-281.

Resio, D. T. (1988a). "Shallow-water waves. II: Data comparisons." *J.Wtrway., Port, Coast., and Oc. Engrg*., ASCE, **114**(1), 50-65.

Resio, D. T. (1988b). "A steady-state wave model for coastal applications." *Proc. 21st Coast. Engrg. Conf*., ASCE, 929-940.

Resio, D. T., and Perrie, W. (1989). "Implications of an f^{-4} equilibrium rangefor wind-generated waves," *J. Phys. Oceanography* **19**, 193-204.

Schneggenburger, C., Gunther, H., and Rosenthal, W. (2000) "Spectral wave modelling (sic) with non-linear dissipation: validation and applications in a coastal tidal environment." *Coastal Engineering*. **41,** 201-235.

Smith, J. M. (1997). "One-dimensional wave-current interaction." Coastal Engineering Technical Note CETN-IV-9, U.S. Army Engineer Research and Development Center, Vicksburg, MS.

Smith, J. M. (1999). "Wave breaking on an opposing current." Coastal Engineering Technical Note CETN IV-17, U.S. Army Engineer Research and Development Center, Vicksburg, MS.

Smith, J. M. (2001). "Modeling nearshore transformation with STWAVE." Coastal and Hydraulics Engineering Technical Note CHETN I-64, U.S. Army Engineer Research and Development Center, Vicksburg, MS.

Smith, J. M., Sherlock A. R., and Resio D. T. (2001). *STWAVE: Steady-State Spectral Wave Model User's Manual for STWAVE, Version 3.0*. ERDC/CHL SR-01-1. Army Engineer Research and Development Center, Vicksburg, MS.

Smith, W.H.F., and D.T. Sandwell, (1997). "Global seafloor topography from satellite altimetry and ship depth soundings." *Science*, **277**, p1957-1962.

Stoker, J.J. (1957). *Pure and Applied Mathematics Volume IV: Water Waves.* Interscience Publishers, New York.

The SWAMP Group. (1985) "Sea Wave Modeling Project (SWAMP): Part 1 Prinicipal Results and Conclusions." Ocean Wave Modeling. Plenum Press.

Thompson, P. D. (1949). "The Propagation of Small Surface Disturbances Through Rotational Current." *Annals of the New York Academy of Science*. **51**. p. 463-474.

Thompson, E. R., Hadley, L. L., Brandon, W. A., McGehee, D. D., and Hubertz, J. M. (1996). "Wave response of Kahului Harbor, Maui, Hawaii," Technical Report CERC-96-11, U.S. Army Engineer Research and Development Center, Vicksburg, MS.

Veeramony, J. and Svendsen, I.A. (2000) "The current in surf-zone waves," *Coastal Engineering*. **39,** 93-122.

Vemulakonda, S. R. (1985). “Current: A Computer Model for Wave-Induced Currents and Setups,” Coastal Engineering Technical Note CETN-I-30, U.S. Army Engineer Research and Development Center, Vicksburg, MS.

Visser, P. J. (1991). “Laboratory Measurements of Uniform Longshore Currents,” *Coast. Eng.*, 15, No. 5, pp 563-593.

Wright, J, Colling, A., and Park, D. (1999). *Waves, Tides and Shallow Water Processes* 2nd ed. rev. Open University Press. 227 p.

Wolf, J. and Prandle, D. (1999). “Some observations of wave-current interaction,” *Coastal Engineering*. **37,** 471-485.

Work, P. A., and Kaihatu, J. M. (1997) “Wave Transformation at Pensacola Pass, Florida,” *J.Wtrway., Port, Coast., and Oc. Engrg*. **123,** 314-321.

Zhang, J. E., and Wu, T. Y. (1999) “Oblique Long Waves on Beach and Induced Longshore Current,” *J. of Engineering Mechanics*. **125,** 812-826.

Zhang, M. Y., and Li, S. Y. (1996). “The Synchronous Coupling of a Third-Generation Wave Model and a Two-Dimensional Storm Surge Model,” *Ocean Engineering*. **23,** 533-543.

Zhinhong, Li, and Davies, A. G. (1996). “Towards Predicting Sediment Transport in Combined Wave-Current Current.” *J.Wtrway., Port, Coast., and Oc. Engrg*. **122** (4):157-164, 1996.

Zundel, A. K., Cialone, M. A., and Moreland, T. J.. (2002). “The SMS Steering Module for coupling waves and currents, 1: ADCIRC and STWAVE,” Coastal and Hydraulics Engineering Technical Note CHETN IV-41, US Army Engineer Research and Development Center, Vicksburg, MS.